POLITECNICO DI TORINO

Master Degree in Biomedical Engineering

Molecular Level Investigation of Cell Penetrating Peptide Adsorption on Silica Surfaces by Classical and Enhanced Sampling Techniques

Thesis Supervisors
Prof. M. A. Deriu
Co-Supervisors
Prof. J. A. Tuszynski
Prof. U. Morbiducci

Candidate
Stefano Mercuri

ACADEMIC YEAR 2018/2019

TABLE OF CONTENTS

Abstract

Magnetic nanoparticles (MNPs) represent one of the most promising materials as they found application in bionanotechnology for enhanced imaging, diagnosis, and treatment of various diseases. Silica improves colloidal stability and the binding affinity for various organic molecules and as such is used to cover iron oxide NPs. One of the strategies for improving the coated MNPs might be the functionalization with organic molecules, such as cell penetrating peptides (CPPs) since they are able to enter into the cells and can enhance the physicochemical properties, adding a cell penetrating feature of the MNPs.

Classical and Enhanced Molecular Dynamics can be used to provide insight on the adsorption mechanism of the peptides onto the silica surface as well as the use of enhanced technique can provide an estimation of the free energy surfaces. In this work, a computational investigation on several CPPs interacting with three different silica surfaces is presented. Also, the use of enhanced sampling techniques is employed to highlight the influence of surface ionization's state on the adsorption mechanism. Although peptide binding is generally moderated by the physicochemical characteristics of the adsorbing peptide, the introduction of such a small degree of functionality onto silica particles was sufficient to produce drastic changes in the peptide's adsorption. In particular, the cationic peptides are strongly attracted to anionic silica surfaces by H-bond formation between charged residues and the negatively charged siloxide groups, as well as ion pairing between the surfaces and the N-termini residues. Moreover, the free energy profile of the adsorption mechanisms of the peptides onto the silica surfaces is provided, confirming the importance of a degree of ionization for selective adsorption.

Introduction

The present section is devoted to a general introduction of the master thesis work, elucidating aims and objectives.

The field of nanomedicine and nanoparticles (NPs) has exploded in the recent years. The use of NPs in the biotechnology has led to enhanced imaging, diagnosis and treatment of various diseases. To improve the overall stability, biocompatibility and biodegradability of the iron oxide NPs, several functionalization's strategies have been developed. Among all, the silica coating is the most common employed method, due to its hydrophilicity, biocompatibility and its easy production process. The silica coating can also help in binding with various biological ligands, such as Cell-penetrating peptides (CPPs). The CPPs functionalization of the silica coating is very promising, since it would enhance the uptake of the NPs due to the intrinsic capability of the CPPs to cross the cellular membrane.

In this work, an *in silico* approach has been employed to investigate the interactions between CPPs and three models of silica surfaces, employing classical molecular dynamics and Well-Tempered Metadynamics, an enhanced sampling method. These advanced computational methods are used to overcome the limits of the classical molecular dynamics simulations and can be helpful to deeply explore the conformational space.

The present work is arranged in chapters as follows:

CHAPTER ONE: A brief introduction to nanomedicine and nanoparticles, with focus on magnetic nanoparticles and functionalization's strategies, in particular silica coating advantages. As further functionalization of the silica coating, the cell-penetrating peptides are introduced, emphasizing the internalization mechanisms of the different classes.

CHAPTER TWO: It represents the theoretical background of the results herein discussed. Molecular modelling, molecular mechanics and molecular dynamics are presented and in the last section, the advantages of the enhanced sampling methods are discussed, with focus on Metadynamics and Well-Tempered Metadynamics.

CHAPTER THREE: The main results of this work are herein presented and discussed. The interactions between cell-penetrating peptides and the different silica surfaces are mainly driven by electrostatics. In particular, the investigation focused on the free energy profile of the systems with means of Well-Tempered Metadynamics techniques.

CHAPTER FOUR: It is devoted to the general conclusion of the present work.

1 Biological Background

This chapter will introduce the essential background on nanomedicine, focusing on magnetic nanoparticles and the silica coating strategy. The cell-penetrating peptides, as further functionalization, are herein introduced and discussed.

1.1 Nanoparticles in drug design

The application of nanotechnology to health and medicine – known as *Nanomedicine* – has grown greatly in the recent years. Indeed, nanotechnology has provided significant improvements in biomedical applications including diagnosis and therapy. In particular, nanoparticles are employed as nanocarriers for imaging and therapeutic agents (e.g. small molecules, proteins, peptides and nucleic acids) due to their unique physicochemical properties based on size, shape and surface properties. Nanomaterials are defined when at least one dimension of the system is less than $100\,nm$, thus possessing unique properties with respect to the bulk materials, such as nanoscale size, high surface to volume ratio and solubility. The nanomaterials range in biomedical applications includes lipids[1], metals[2], polymers[3], proteins[4], carbon[5], silicon and silica[6,7]. In particular, the NPs can be classified in *organic NPs* (such as liposomes, polymeric NPs, dendrimers, etc.) and *inorganic NPs* (such as metal NPs, silica NPs, magnetic NPs). The nanoparticles have been design in the treatment of diseases such as diabetes, neurological disorders, cancer, etc. and have made it to clinical trials and regulatory approval[8,9].

The use of nanocarriers enables sustained and controlled drug release, as well as the protection of the payload from biological degradation. Moreover, nanoparticles have the potential to decrease clearance and improve accumulation of drugs in a diseased tissue, thereby increasing therapeutic efficacy and reducing side effects. The body contains several barriers that must be overcome in order to reach a precise site, such as renal clearance, enzymatic degradation, vascular endothelium, lysosome, etc. The nanoparticles can be designed to overcome these barriers, releasing their cargo *in vivo*. Moreover, certain nanoparticles have electrical and optical properties that can be exploit for therapeutic purposes.

Overall, the most important features of a NP is the large surface area and the high surface-to-volume ratio. The large surface area accounts for the high loading capacity of functional molecules that can also be improved by a large porosity. The small size of NPs influences the renal clearance, in particular, a NP smaller than $8\,nm$ will be quickly cleared by the kidneys, while NPs with size in the $30 - 200\,nm$ range can accumulate in tumors by the enhanced permeability and retention (EPR) effect[10]. The EPR effect is a phenomenon based on the fact that sane tissues have thick vessel and with less pores, in contrast to tumoral

tissues, which have vessel lacking basal lamina and with high porosity. Also, the surface properties determine the hydrodynamic size and the surface charge of the NP, as well as its reactivity (e.g. binding affinity). It is to mention that positive charged NPs are more toxic because they cause several problems, like hemolysis and platelet aggregation. Positively charged NPs also have shorter circulation *half-life* than its negative and neutral counterpart[11].

The NPs can be *non-targeted* or *targeted*. The non-targeted NPs accumulate in tumor tissue through the EPR effect, which results from enhanced vascular permeability and the absence of a functioning lymphatic system. For efficient NP accumulation, long circulation time is important and requires efficient particle evasion from the clearing organs (e.g. liver). The targeted NPs, instead, present ligands on the surface, resulting in active binding of the NPs to the cell surface antigens.

The non-targeted NPs work well in solid tumors and inflamed tissue, where the leaky vasculature is high, but the EPR effect depends on the leaky tumor vasculature that could be limited in certain cancers (e.g. pancreatic cancer).

The targeted NPs are used for tumor targeting – where the accumulation and cellular uptake is enhanced through receptor-mediated endocytosis – and for vascular targeting, where the accumulation of NPs in the vascular wall is not a function of the EPR effect, albeit the tumor accumulation is largely determined by the particle physiochemical properties.

An important category of NPs is represented by the *Magnetic nanoparticles* (MNPs)[12]. Their main advantages are that they can be:

- visualized by magnetic resonance imaging (MRI);
- guided to target sites by means of an external magnetic field;
- heated to provide hyperthermia for cancer therapy;
- often degraded into non-toxic species in vivo;
- coated with different shells (surface tailoring, drug carriers, active targeting, etc.)

Due to their reduced size, the MNPs are superparamagnetic, which means that they have no hysteresis, much stronger magnetization, zero remanence and zero coercivity.

The MNPs are used in a wide range of applications, such as drug targeting and delivery, multimodal imaging, cells labelling, contrast enhancer MRI, hyperthermia treatment, gene delivery, etc. They are often preferred for biomedical applications because they have controllable small size, comparable to those of many biological entities.

In the last decade, several types of iron oxides have been developed for MNPs, such as *magnetite*[13] and *maghemite*[14] which are very promising candidates due to their proven biocompatibility.

1.1.1 Functionalization strategies

The problem with MNPs is that they have a large surface-to-volume ratio, which means high surface energies that manifests in the aggregation of the NPs in order to minimize the surface energies. In fact, the naked iron oxide NPs, have high chemical activity and are easily oxidized in air, which leads to loss of magnetism and dispersibility. Furthermore, the NPs has an intrinsic toxicity that can be manifested at the molecular, cellular and tissue level. As a NP moves through the body, it is exposed to different biological compartments, including blood, extracellular matrix, cytoplasm and cellular organelles. The interactions with these different microenvironments may impact the function of biomolecules, cellular components and tissue structure, a toxic response[11].

In order to avoid agglomeration, enhance biocompatibility and biodegradability, several surface coating and effective protection strategies have been developed[15].

The functionalization strategies consist in grafting of (or coating with) organic molecules, including small organic molecules or surfactants, polymers and biomolecules; or coating with an inorganic layer, like silica, metal oxide or metal sulfide.

1.1.2 Silica Coating

The surface functionalization with inorganic materials can be classified into five categories: core-shell, mosaic, shell-core, shell-core-shell and dumbbell as seen in Figure 1-1.

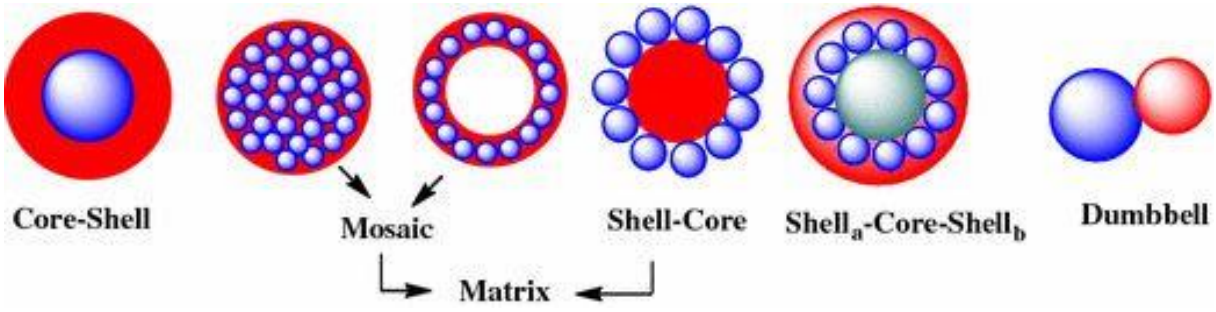

Figure 1-1 Different strategies of surface functionalization of the NPs.

The most common compound for preparing the functionalized iron oxide NPs is the Silica. The silica-coated NPs have many advantages such as:

- It provides stability to the MNPs in solution, avoiding the interparticle interactions and preventing agglomeration;
- Good biocompatibility, hydrophilicity and stability;
- The technology of preparation for size tunable composite NPs is already mature, and its variation of the shell thickness is relatively easy to control;
- Silica coating helps in binding the various biological or the other ligands at the NPs surface for several applications.

These shells serve the function of stabilization of the iron oxide NPs and can be also used for further functionalization, likewise cell-penetrating peptides.

1.2 Cell-Penetrating Peptides (CPPs)

Generally, a molecule is considered *peptide* if it is composed by a chain of less than 50 amino acid. Peptides are generally obtained by chemical synthesis or by recombinant DNA technique but some of them are naturally derived. They are essentials in several physiological functions: they can act as hormones, neurotransmitters, growth factors, ion-channel ligand or anti-infective. There are about 140 peptide therapeutics currently evaluated in clinical trials[16] thanks to their safety and tolerability but also to their production cost and complexity.

The advantages of peptides include good safety, efficacy, tolerability, high selectivity and standard synthesis protocols. However, they also have drawbacks like tendency for aggregation, short half-life and chemical/physical instability. To overcome their problems, several techniques emerged to design the peptides and overcome their weaknesses. The peptides are collected into three categories[17] – therapeutics peptides, immunogenic peptides and *CPPs*. The latter type has been identified in 1988, when it was discovered that the TAT protein, derived from human immunodeficiency virus 1 (HIV-1), was internalized by the cells promoting the viral activity[18].

In 1991, the same mechanism was discovered also about the homeodomain of Antennapedia, a homeoprotein of *Drosophila melanogaster*[19], and three years later its 16th peptide of the third helix was discovered as main component of the crossing-cell mechanism and has been named *penetratin*[20].

As shown in Figure 1-2, over the past decade a lot of research has been done toward CPP because of its potential application. A CPP is a short chain of about 5-30 amino acids that can cross the cell's membrane via energy-dependent or energy-independent mechanisms without the necessity of a chiral recognition by specific receptors. The CPPs can be used to deliver cargoes to cells, like siRNA, dsDNA, nanoparticles, proteins, liposomes, and small molecule drugs, through covalent or non-covalent complex formation.

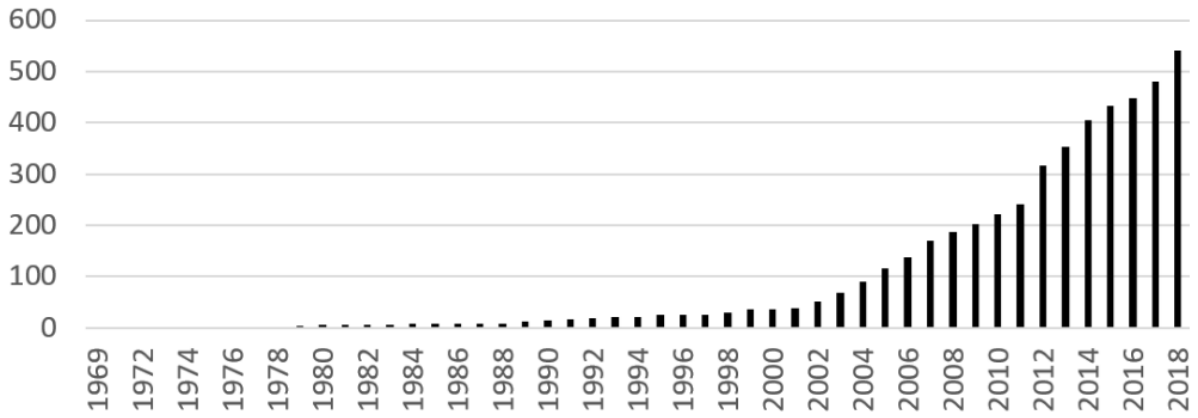

Figure 1-2 Result by year of searching "cell penetrating peptide" on PubMed.

There are different classifications of CPPs, based on their origin, sequence, function or their physical-chemical properties. The CPPs can be regrouped into three main class: *cationic, amphipathic* and *hydrophobic* class[21].

1.2.1 Cationic CPPs

A *cationic CPP* contains a stretch of positive charges – essential for the cellular uptake – and its 3D structure does not lead to an amphipathic helix. This class include Tat-derived peptides, penetratin, and polyarginine. This peptides usually contains more than five positively charged amino acids and studies have shown that arginine-based peptide have a more increased level of cellular uptake than lysine-based peptide, suggesting that the presence of arginine is a crucial factor in crossing cellular membrane[22]. A different type of cationic CPPs are *nuclear localization sequences (NLS)*, which are short cationic peptide based on lysine-, arginine- or proline-rich motifs that can cross the nuclear membrane through the nuclear pore. Most of them have few positive charges and are not very efficient.

1.2.2 Amphipathic CPPs

Amphipathic CPPs can be classified into primary, secondary α-helical, secondary β-sheet and proline-rich CPPs[23]. *Primary CPPs* are chimeric peptide obtained by covalently attaching a hydrophobic domain to an NLS – which is needed to enhance the cell-targeting. The amphipathic CPPs have showed high nuclear localization with regards to cationic CPPs[24] , suggesting a potential nuclear drug delivery application. *Secondary α-helical CPPs* show helicoidal structure in which the hydrophilic and hydrophobic residues are grouped on different sides of the helix and the amphipathicity can be visualized by the graphical method of the helical wheel[25]. Some studies demonstrated that the membrane penetration into the cytosol – *membrane translocation* – is based on the helical amphipathicity and does not depend upon the presence of positive charges[26]. *Secondary β-sheet CPPs* show one hydrophilic and one hydrophobic stretch of amino acids exposed to the solvent and this conformation – along with water solubility – is important for the uptake of this peptides[27]. The

latter type of amphipathic CPPs, the *proline-rich CPPs*, contain a pyrrolidine ring which gives rigidity to the peptides. Several proline-rich CPPs had been synthesized, with various R-group attached to the pyrrolidine ring.

1.2.3 Hydrophobic CPPs

The *hydrophobic CPPs* contain only nonpolar residues – which also means low net charge – and a hydrophobic motif or chemical group that is essential for the cellular internalization[23]. Despite the poor hydrophobic CPPs discovered – mainly because cationic and amphipathic CPPs where discovered first – they have a unique way to cross the membrane which is a spontaneous and passive energy-independent mechanism[28]. As well, the hydrophobic CPPs are classified in: *peptides based on natural amino acids, stapled peptides, prenylated peptides* and *pepducins*. In Table 1.1 are reported some example of cell-penetrating peptides.

Table 1.1 Examples of CPPs and their sequences, origins, and physical-chemical properties

CPP name	Sequence	Origin	Class
HIV-1 TAT protein, TAT_{48-60}	GRKKRRQRRRPPQ	HIV-1 TAT protein	Cationic
HIV-1 TAT protein TAT_{49-57}	RKKRRQRRR	HIV-1 TAT protein	Cationic
Penetratin, pAntp (43-58)	RQIKIWFQNRRMKWKK	Antennapedia *Drosophila melanogaster*	Cationic
Polyarginines	Rn	Chemically synthesized	Cationic
MPG	GALFLGFLGAAGSTMGAWSQPKKKRKV	HIV glucoprotein 41/ SV40 T antigen NLS	Amphipathic
pVEC	LLIILRRRIRKQAHAHSK	Vasccular endothelial cadherin	Amphipathic
ARF(1-22)	MVRRFLVTLRIRRACGPPRVR	P14ARF protein	Amphipathic
MAP	KLALKLALKALKAALKLA	Chemically synthesized	Amphipathic
Transportan	GWTLNSAGYLLGKINLKALAALAKKIL	Chimeric galanin-mastoparan	Amphipathic
p28	LSTAADMQGWTDFMASGLDKDYLKPDD	Azurin	Amphipathic
C105Y	CSIPPEVKFNKPFVYLI	α1-Antitrypsin	Hydrophobic
PFVYLI	PFVYLI	Derived from synthetic C105Y	Hydrophobic
PEP-7	SDLWEMMMVSLACQY	CHL8 peptide phage clone	Hydrophobic

1.2.4 Membrane Penetration mechanisms

The cellular uptake of CPPs is a central question for the development and designing of therapeutic agents for targeted cellular therapy. Still, for most CPPs the cellular uptake mechanism remains a mystery for studies to come. The difficulties underlying the experiment regard different parameters like, for example, the fluorescent dye – used to follow the CPPs during the translocation – which can interfere with the mechanism, but also by the nature of the CPPs, its secondary structure, the cargo and its electrostatic nature, and so on.

Several studies have reported different pathways and it's believed that all of these happen at the same time. For sure, the first contacts between the CPPs and the cellular membrane are mediated by electrostatic interaction with the proteoglycans GlucosAminoGlycan (GAG) – which interact with the cytoskeleton and trigger the actin remodeling[29,30]. The actin remodeling is at the base of the energy-dependent mechanism of *endocytosis*, which can follow the *macropinocytosis*[31]*,* the *clathrin-mediated endocytosis*[32] or the *caveolae-mediated uptake*[33]. Besides endocytosis, another energy-independent route is involved – the *direct penetration* or *translocation*, which occurs at low extracellular concentration of the CPP in contrast to endocytosis[34].

Endocytosis

Endocytosis is a physiological process by which the cells adsorb material by the surroundings. It is triggered by several stimulus all of which provoke the engulfment of the outer membrane into vesicles in an energy-dependent process. The endocytosis routes can be divided into 4 subgroups: *macropinocytosis, clathrin-mediated endocytosis, caveolae* and *phagocytosis*[35]. Nevertheless, there's to say that the markers and the endocytic inhibitors used to understand the uptake mechanism of a specific CPP can influence the pathway itself. So all these results must be taken carefully[36].

Macropinocytosis

Macropinocytosis consists in the engulfment of the plasma membrane to form a vesicle (approx. 0.5-50 μm in diameter) filled with the extracellular surrounding. It is involved in the internalization of polyarginines and penetratin[31,37] and it is considered to be the main route for most cationic CPPs[38,39].

Clathrin-mediated endocytosis

Clathrin-mediated endocytosis is mediated by the production of small (approx. 100 nm in diameter) vesicles that have a morphologically characteristic coat made up of the cytosolic protein clathrin. It is considered to be the main endocytic pathway concerning the TAT peptide, Penetratin and other CPPs[40].

Caveolae-mediated Uptake

Caveolae are the most common reported non-clathrin-coated plasma membrane buds, which exist on the surface of many, but not all cell types. Caveolae are small (approx. 50 nm in diameter) flask-shape pits in the membrane. They consist of the cholesterol-binding protein caveolin (Vip21) with a bilayer enriched in cholesterol and glycolipids. Caveolae uptake was demonstrated for Tat peptide[33], but it is not clear since macropinocytosis is also involved[38].

Direct penetration

The translocation across the plasma membrane is the main mechanism if the endocytic inhibitors don't affect the CPP penetration's capability. This mechanism is mediated by the destabilization of the plasma membrane by the electrostatic interaction with the CPPs. Several theories have been proposed to explain this mechanism[41].

Inverted micelle formation

This model was reported as the mechanism of the penetratin's uptake[42]. In inverted micelle formation the basic residues interact with the negatively charged phospholipids forming a neutral complex that encapsulates the peptide in its interior[43]. Then, the membrane disruption releases the peptide into the cytosol. A recent *in-silico* study explained the inverted micelle hypothesis as a minimization of the potential energy of the peptide[44].

Pore formation model

Speculations about the translocation of hydrophilic CPPs in an energy-independent manner headed to this model, which has been reported in molecular dynamics simulations and physiological experiments[45,46]. The basic idea is that the arginine-rich TAT peptide – which is basic and hydrophilic – spontaneously crosses the lipid membrane through the interaction between the phosphates group on both sides of the lipid bilayer, leading to destabilization and nucleation of transient pores across the membrane. This mechanism involves the thermal fluctuation of the membrane, which results in fluctuation of the local density, such as rarefaction, called a *prepore*. The prepores are instable and have a toroidal-like structure and their accumulation cause a thinning of the bilayer forming a transient pore[41].

Adaptive translocation

This model has been proposed for the uptake of the guanidinium-rich peptide[47] which are positively charged and their interaction with the negatively charged phospholipids lead to the transient formation of a ion pair complex with attenuated polarity, able to diffuse across the lipid apolar bilayer.

Endosomal escape

Although there are numerous ways of entering the cell, the main door is represented by endocytosis. So, questions arise about when and how CPPs-cargo conjugates escape the

endosome and leak to the cytosol. The *endosomal escape* would involve the endosomal acidification which dissociate the cationic CPPs from the GAGs[48]. The mechanisms involving direct penetration are represented in Figure 1-3.

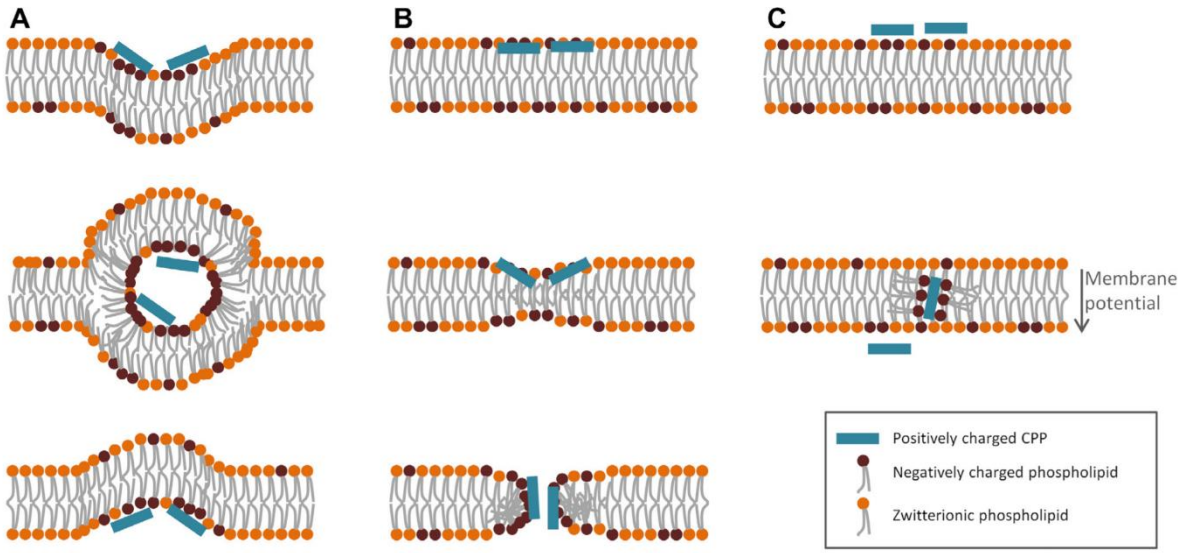

Figure 1-3 Examples of the proposed mechanisms for direct translocation. (A) Inverted micelle formation. (B) Pore-formation. (C) Adaptive translocation.

1.3 Selected Cell-Penetrating Peptides

In the present work, six cell-penetrating peptides were selected interacting with the silica surfaces models:

- CADY (GLWRALWRLLRSLWRLLWRA): the CADY peptide is an amphipathic peptide composed by 20 amino acidic residues of aromatic tryptophan and arginine. It was designed to improve cellular uptake of siRNA sequences[49,50]. It assumes an helical structure inside cell membranes, exposing charged residues on one side and tryptophan groups that improve the cellular uptake on the other.
- MAP (KLALKLALKALKAALKLA): the MAP peptide is an amphipathic chemically synthesized peptide, utilized as synthetic vaccines to produce anti-peptide antibodies[51]. Thanks to the high molar ratio of the peptide antigen to the core molecule, no carrier protein is needed to elicit an antibody response.
- pAntp $_{43}$(RQIKIWFQNRRMKWKK)$_{58}$: the pAntp peptide corresponds to the third helix of the homeodomain fragment of the Antennapedia. It is responsible for the penetration mechanism and characterized by seven positively charged residues[52].
- PEP (KETWWETWWTEWSQPKKKRKV): the PEP peptide is a short amphipathic peptide composed of hydrophobic tryptophan-rich domain and a hydrophilic lysine-rich domain separated by a spacer[53].
- Nona-arginine (ARG)9: The (ARG)9 peptide has been reported as the most effective arginine-rich peptide: at low concentration ($\leq 5\mu M$) (ARG)9 is internalized with an endocytic mechanism but at high concentration ($\geq 10\mu M$) can translocate. Above all, it has been proposed as a mechanism of action for cellular uptake the cross-linking of heparan sulfates and the interaction with lipid head groups[51].
- TAT (YGRKKRRQRRR): the TAT peptide is a short, highly basic and unstructured N-terminal sequence, necessary for the uptake mechanism. The TAT peptide derived from nuclear transcription activator TAT of human immunodeficiency virus-1. A novel study has designed and synthesized two conjugates of the TAT peptide attaching the *camptothecin* (CPT) to the N-terminus. These conjugates (TAT-CPT and TAT-2CPT) could kill cancer via membrane disruption – which is a mechanism found in antimicrobial peptides – and via releasing of CPT[54].

2 Materials and Method

This chapter is devoted to a general introduction of the molecular modeling, introducing to molecular dynamics and enhanced sampling techniques, such as Metadynamics and Well-Tempered Metadynamics.

2.1 Introduction to Molecular Modeling

A model is a representation of a system which permits to describe a natural phenomenon by solving the mathematical equations underneath. In such way, it is possible to represent different aspects of the reality, their interactions and their dynamics. All science fields make uses of mathematical models in order to analyze, comprehend and quantify such phenomena. In this context, the molecular modeling is a fast emerging area, used for the modeling and simulation of biological systems through computational techniques. It has a wide range of applications in various disciplines of engineering sciences, such as materials science, chemical engineering, biomedical engineering, etc.

Molecular modeling make use of the quantum mechanics, molecular mechanics, minimization, simulations, conformational analysis and any theoretical or computational technique that provides insight into the behavior of molecular systems. Nowadays, the molecular modeling has exponentially grown thanks to tremendous improvements in computer hardware and software, making it possible to simulate biological systems consisting of huge number of molecules. As so, the most detailed analysis of a biological system would start at the quantum level, with each *electron-electron interaction* in the system being considered separately. This would require the solving of the Schrödinger equation (known as an *ab initio calculation*) and quantum mechanical simulations usually exploit some simplified model of the interactions between electrons. However, this approach is not feasible for biological systems larger than 100/1000 atoms.

Among all computational methods, the Molecular Dynamics (MD) is a powerful tool of investigation of biomolecular systems. Indeed, at the molecular level the system is defined in terms of interactions between atoms and ions, which are modulated by hydrogen bonding, electrostatics, van der Waals interactions, and deformation of chemical bonds. By simply solving the Newton's laws, MD provide as a result the trajectory of the systems, in terms of positions and velocities of the particle.

2.2 Molecular Mechanics

In order to solve the Newton's laws, the potential energy function must be defined. The Molecular Mechanics (MM) method allows the modeling of very large molecules, such as

proteins and segments of DNA by setting up a simple algebraic expression for the total energy of a compound.

The MM method model the interactions within the systems as several contributions – like stretching of bonds, rotations about bonds, and treats the atoms as spheres and bonds as springs, neglecting the electronic motions (Born-Oppenheimer approximation) without which it would be impossible to write the energy as function of the nuclear coordinates.

The set of equations and parameters used to define the potential energy function V is known as *force field*.

2.2.1 The Potential Energy function

In MD simulations, the force field parameters model all the interactions between bonded atoms and non-bonded pairs by deriving the force from the potential energies V. In particular, the energy surface for a molecular system of N atoms as functions of the positions is given by:

$$V(r^N) = V_{bonded} + V_{non-bonded} \tag{2.1}$$

The *bond* and *non-bonded* contributions are treated separately and each term can be modelled in a different way, depending on the simulation settings. The bonded interactions model the bond lengths, the angle and the rotation of bonds or movements of atoms relative to each other. Instead, the non-bonded interactions models the contributions between all pairs of atoms that are in different molecules or that are separated by at least three bonds.

So, the terms in equation 2.1 can be written as:

$$V_{bonded} = V_{bonds} + V_{angles} + V_{dihedrals} \tag{2.2}$$

$$V_{non-bonded} = V_{van\ der\ Waals} + V_{electrostatic} \tag{2.3}$$

2.2.2 Treatment of bond and non-bond interactions

Depending on the choice of the force field, the terms in equation 2.1 can be modeled using different algebraic expression. One functional form for such a force field is:

$$\begin{aligned} V(r^N) = &\sum_{bonds} \frac{k_l}{2}\left(l_i - l_{i,0}\right)^2 + \sum_{angles} \frac{k_\theta}{2}\left(\theta_i - \theta_{i,0}\right)^2 + \sum_{torsions} k_\phi(1 + \cos(n\phi - \delta)) \\ &+ \sum_{i=1}^{N}\sum_{j=i+1}^{N}\left(4\epsilon_{ij}\left[\left(\frac{\sigma_{ij}}{r_{ij}}\right)^{12} - \left(\frac{\sigma_{ij}}{r_{ij}}\right)^{6}\right] + \frac{q_i q_j}{4\pi\epsilon_o r_{ij}}\right) \end{aligned} \tag{2.4}$$

The first term in equation 2.4 models the interaction between pairs of bonded atoms, modelled as an harmonic potential with stiffness k_l that gives the increase in energy as the

bond length l_i deviates from the reference value $l_{i,0}$. The second term is a summation over all valence angles in the molecule, using also an harmonic potential with stiffness k_θ, where a valence angles is defined as the angle formed between three atoms and $\theta_{i,0}$ is the bond angle at equilibrium. The third term is a torsional potential that models how the energy changes as a bond rotates and its energy is here modelled as a series of cosines: k_ϕ is the energetic barrier related to angle deformation, δ is the phase that determines the minimum position for the torsional angle

The non-bonded interactions are represented by the fourth and fifth term in equation 2.4. The non-bonded interactions do not depend upon a specific bonding relationship between atoms, and they are modelled by a function of some inverse power of the distance and includes two components: Van der Waals forces and Electrostatic interactions.

The Van der Waals interactions account for derivations from ideal gas behavior and are here modeled with the *Lennard-Jones* equation. It incorporates a repulsive term ($4\epsilon_{ij}\left(\frac{\sigma_{ij}}{r_{ij}}\right)^{12}$) and an attractive term ($4\epsilon_{ij}\left(\frac{\sigma_{ij}}{r_{ij}}\right)^{6}$) where σ_{ij} are the collision diameters (minimum distance to which the interaction potential is zero), r_{ij} is the distance between atom i and atom j and ϵ_{ij} is the depth of the potential well at which the attraction is at a maximum.

The Electrostatic interactions are described by the Coulomb's law, where ϵ_0 is the vacuum permittivity. This type of interaction is defined as long-range interaction, because the energy decreases as the distance between two atoms decreases.

Non-bonded interactions grow with the square number of system's particles, thus requiring a high computational cost. To overcome this phenomenon, one can define a *distance cut off* or several other tricks, such as Particle Mesh Ewald[55], Reaction Field, Multipole Cells[56]. Also the Periodic Boundary Condition (PBC) are introduced to avoid problems with boundary effects caused by finite size, and make the system more like an infinite one, at the cost of possible periodicity effects.

2.2.3 Periodic Boundary Conditions

The periodic boundary conditions[57] are very useful to minimize the edge effects and allows performing simulations of bulk systems with a smaller number of particles. The PBC are desired for simulating a solid crystal, representing its unit cell. For what concerns liquids or solutions, the PBC will introduce errors if not set right. In the periodic boundary conditions, particles are placed in a simulation box – which can have different shapes – and are surrounded by infinite replicas, thus mimic the bulk systems. In this way, there are no

boundaries of the system and an atom leaving the system on the left will reenter from the right, as in Figure 2-1.

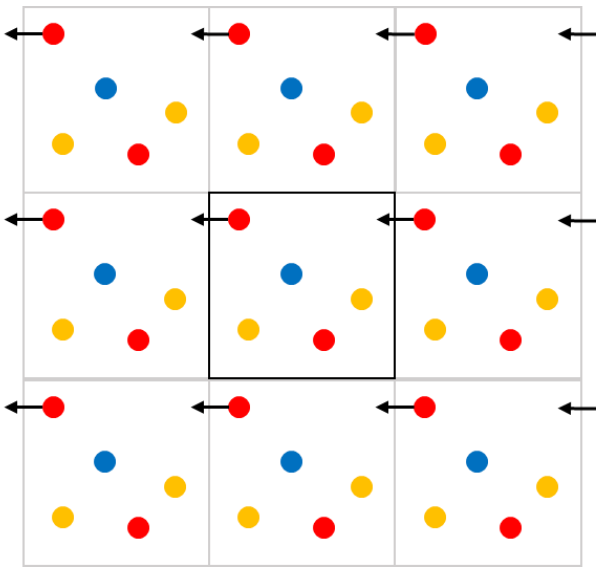

Figure 2-1 2D periodic boundary conditions (PBC) scheme.

It is to notice that in order to avoid a particle interacting with itself, the *Minimum Image Convention* should be taken into account when choosing a distance cutoff for the long-range interactions. Other approaches such as Particle Mesh Ewald, Reaction Field and Multipole cells can overcome these problems, avoiding the discontinuities introduced by cutoff.

2.2.4 Potential Energy Minimization

The use of computational techniques require performing a geometry optimization as first step. Indeed, the potential energy function is a multidimensional function of the molecular system coordinates where the minimum points correspond to stable states of the system. Hence, the methods of geometry optimization aims to find the *local minima* of the potential energy surface (PES). The energy minimization algorithms are classified in two groups: derivative and non-derivative methods.

The non-derivative methods require energy evaluation only and acts changing the coordinates of the atoms in order to find an energy minimum. The Simplex algorithm represents one of these methods.

The derivative methods can be further divided in two classes: *First order* and *Second order* derivative methods. The first order derivative methods – such as Steepest Descent and Conjugate Gradient **–** calculates the direction of the first derivative of the energy, which indicates where the minimum lies, and its magnitude indicates the steepness of the local slope. The second order derivative methods – such as Newton Raphson or L-BFGS – takes

into account the Hessian matrix of the energy function, providing information about the curvature of the PES.

2.3 Molecular Dynamics

As said before, the MD provide the trajectory of the systems of N particles, in terms of positions, velocities and forces by solving the Newton's laws:

$$m_i \frac{\partial^2 r_i}{\partial t^2} = F_i \tag{2.5}$$

Where m_i and r_i represent the mass and the position of the *i*th particle of the system ($i = 1 \dots N$) respectively and F_i are the forces that can be expressed in terms of the potential energy:

$$F_i = -\frac{\partial U(r_i, \dots ., r_N)}{\partial r_i} \tag{2.6}$$

2.3.1 Statistical Ensemble

The macroscopic physical properties can be divided into *static equilibrium properties* (e.g. average potential energy, radial distribution function) and *non-equilibrium* or *dynamic properties* (e.g. the dynamics of phase changes, diffusion processes).

Inferring the macroscopic physical properties of a system require the necessity to generate a representative statistical ensemble at a given temperature which delineates all the accessible physical states of a molecular system. Overall, a molecular system is defined in a multidimensional space – called *phase space*: the state of a system containing N atoms is described by $6N$ coordinates (three coordinates of position and three components of momentum). Hence, a *statistical ensemble* is a collection of all possible system configurations that have different microscopic state but identical macroscopic or thermodynamic state. In particular, a set of four ensemble is defined:

- The Micro-Canonical Ensemble (NVE) – characterized by fixed volume, energy and number of particles;
- The Canonical Ensemble (NVT) – characterized by fixed volume, temperature and number of particles;
- The Isobaric-Isothermal Ensemble (NPT) – characterized by fixed pressure, temperature and number of particles;
- The Grand Canonical or Gibbs ensemble (μVT) – characterized by fixed volume, temperature and chemical potential.

The MD simulations are able to sample the phase space and the generated ensemble such that it is able to calculate the ensemble average of the macroscopic property by integrating over all the possible configurations of the system:

$$< A >_{ensemble} = \iint A(p^N, q^N)\rho(p^N, q^N)dp^N dq^N \tag{2.7}$$

Where p^N are the coordinates of the N particles of the system, q^N are their momenta, $A(p^N, q^N)$ is the property of interest and $\rho(p^N, q^N)$ is the probability density of the ensemble, expressed in terms of a Boltzmann distribution as:

$$\rho(p^N, q^N) = \frac{1}{Q} e^{\frac{H(p^N, q^N)}{k_B T}} \tag{2.8}$$

Where H is the Hamiltonian, k_B the Boltzmann constant, T the temperature and Q is the partition function of the system, defined as follow in equation 2.9:

$$Q = \iint dp^N dq^N e^{-\frac{H(p^N, q^N)}{k_B T}} \tag{2.9}$$

The partition function designate the normalize sum of the Boltzmann factor of all microstates. It is also extremely important since all the macroscopic properties can be written as a function of the partition function; it correlates the microscopic and the macroscopic states but the analytical solution is merely impossible because it is extended at all the states of the system.

Nonetheless, under the *ergodic hypothesis* this issue can be addressed. In fact, it states that over long periods of time, the time-average of a certain physical property represents the ensemble-average of the same property, which means:

$$< A >_{ensemble} = < A >_{time} \tag{2.10}$$

$$< A >_{time} = \lim_{\tau \to \infty} \frac{1}{\tau} \int_{t=0}^{\tau} A\big(p^N(t), q^N(t)\big)dt \approx \frac{1}{M} \sum_{t=1}^{M} A(p^N, q^N) \tag{2.11}$$

Where t is the simulation time, M is the number of time steps in the simulation and $A(p^N(t), q^N(t))$ is the instantaneous value of the calculated property.

2.3.2 Implementation Scheme

As described in equation 2.5 and equation 2.6, the MD aims to solve Newton's equations of motion and several numerical integration algorithms have been developed to overcome the complex form of the potential energy function. All these algorithms are based on the Taylor expansions of positions, such as the Verlet algorithm, the Leap-frog algorithm or the Velocity Verlet[58].

An important choice is the integration time-step (expressed in fs) that accounts for the instability issues and the incorrect sampling of the phase space. A good time step should be smaller than $1/10^{th}$ of the fastest harmonic oscillator.

The implementation scheme of a MD simulation is represented in Figure 2-2.

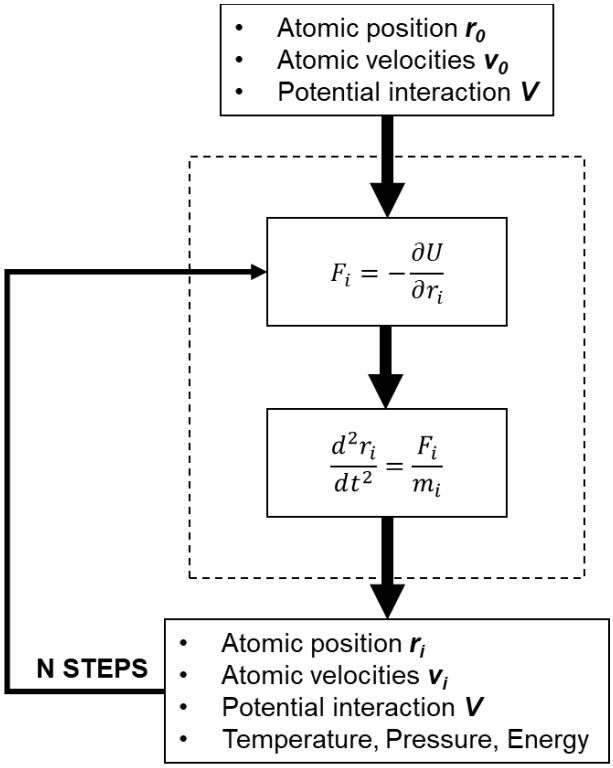

Figure 2-2 MD flowchart: starting from initial position and velocity, the initial potential is calculated. Then the algorithm calculates the forces. Thus, new positions and velocity are generated and the cycle continues for a certain number of steps.

The initial atoms velocities v_0 are generated randomly from a Maxwell-Boltzmann distribution at a given temperature, while the initial atoms positions r_0 are known from experimental data (e.g. Protein Data Bank). So, the simulation proceeds computing the initial potential, then the forces, the new positions and velocities until the equilibrium state is reached and the macroscopic properties are calculated as function of time.

2.4 Enhanced Sampling Techniques

The MD simulations have grown a lot in the recent years, allowing the study of several biological system: from small molecules to large protein complexes in a solvated environment. Nonetheless, the MD simulation are affected by two major drawbacks, which are related to the high computational costs – due to the number of interacting particles – and to the rough energy landscape which cause the system to be trapped in a local minimum with no possibility to explore other minima due to high energy barriers.

To address these issues, the *Enhanced Sampling techniques*[59] have emerged. The *Enhanced Sampling techniques* belong to 4 general classes:

1. Coarse-graining: reduce the number of degrees of freedom, preserving the relevant physics;
2. Biasing: adapts interactions to reduce phase space and/or smoothen the free energy landscape;
3. Jumping: exchanges snapshots between conditions to overcome barriers;
4. Multiscaling: reduce detail in the surroundings leading to effective interactions.

For what concerns the Biasing class, example of enhanced sampling algorithm are *Replica-Exchange*, *Simulated Annealing*, *Umbrella Sampling* and *Metadynamics.*

The idea of the *Replica-Exchange* (REMD) is to run multiple independent MD simulations with different values of a specific exchange variable (such as temperature) and at certain time intervals, a system state exchange based on an acceptance criterion is attempted. By doing so, the hope is to overcome the energy barriers on the potential energy surface, allowing a wide exploration of the conformational space.

The *Simulated Annealing* algorithm involves a dynamic range of temperature throughout the simulation. In particular, the temperature starts from high values and decrease to the reference value: higher temperatures help the system to overcome metastable states, reaching other minima configurations and sampling all the possible stable conformations of the studied molecules.

The *Umbrella Sampling* method generates a series of configurations along a reaction coordinate ζ, which are run in independent simulations each of one is biased with an umbrella biasing potential. In this way, one can force the system to explore only a predefined region of the space and combining the simulation through the *Weighted Histogram Analysis* information about the *Potential Mean Force* can be extracted.

2.4.1 Metadynamics

Metadynamics (METAD)[60] belong to a subclass of the Enhanced Sampling techniques in which sampling is facilitated by the introduction of an additional bias potential (or force) that acts on a selected number of degrees of freedom, referred as collective variables (CVs). Other methods that belong to the same class are umbrella sampling, adaptive force bias or steered MD.

The METAD simulation introduces an external history-dependent bias potential, written as function of few selected CVs and added to the Hamiltonian of the system. This potential take forms as a series of Gaussians deposited along the system trajectory in the CVs space, in order to force the system to explore different configurations.

Let S be a set of d functions of the microscopic coordinates R of the system:

$$S(R) = (S_1(R), \dots, S_d(R)) \tag{2.11}$$

At time t, the metadynamics bias potential can be written as:

$$V_G(S,t) = \int_0^t dt' \omega \exp(-\sum_{i=1}^{d} \frac{\left(S_i(R) - S_i\left(R(t')\right)\right)^2}{2\sigma_i^2}) \tag{2.12}$$

Where ω is an energy rate and σ_i is the width of the Gaussian for the ith CV. The energy rate can be expressed as a Gaussian height W and a deposition stride τ_G:

$$\omega = \frac{W}{\tau_G} \tag{2.13}$$

The effect of the V_G is to push the system away from local minima into visiting new regions of the phase space. Furthermore, in the long time limit, the bias potential converges to minus the free energy as a function of the CVs:

$$V_G(S, t \to \infty) = -F(S) + C \tag{2.14}$$

Where C is an irrelevant additive constant and $F(S)$ is the free energy, defined as:

$$F(S) = -\frac{1}{\beta} \ln(\int dR\ \delta\big(S - S(R)\big) e^{-\beta U(R)} \tag{2.15}$$

Where $\beta = (k_B T)^{-1}$, k_B is the Boltzmann constant, T is the temperature of the system and $U(R)$ the potential energy function.

The metadynamics method has many advantages, because not only accelerates the sampling of rare events by pushing away the system from local minima, it also requires no *a priori* knowledge of the landscape and allows the exploring of new reaction pathways. In Figure 2-3 is shown the metadynamics pseudo-code based on MD simulations.

set initial $\{\vec{r}\}$ and $\{\vec{v}\}$
set $V_{bias}(\vec{s}) \coloneqq 0$

every MD step:

compute CV values:

$\overrightarrow{s_t} \coloneqq \vec{s}\,(\{\vec{r}\})$

every n MD steps:

update bias potential:

$$V_{bias}(\vec{s}) \coloneqq V_{bias}(\vec{s}) + \tau\omega exp\left(-\frac{1}{2}\left|\frac{\vec{s}-\overrightarrow{s_t}}{\vec{\sigma}}\right|^2\right)$$

compute atomic forces:

$$\overrightarrow{F_i} \coloneqq -\frac{\partial V(\{\vec{r}\})}{\partial \vec{r}_i} - \frac{\partial V_{bias}(\vec{s})}{\partial \vec{s}}|_{\overrightarrow{s_t}}\left(\frac{\partial \vec{s}(\{\vec{r}\})}{\partial \overrightarrow{r_i}}\right)$$

propagate $\{\vec{r}\}$ and $\{\vec{v}\}$ by Δt

Figure 2-3 Metadynamics pseudo-code.

2.4.2 Well-Tempered Metadynamics

The METAD simulations are also affected by two important problems. The first is the choice of an appropriate set of CVs, which is very trivial and depends on the system. The second issue regards the fact that in a single run V_G does not converge modulo a constant to the free energy, but oscillates around it. This leads to the system being pushed toward high-energy regions of the CVs space. The last problems is due to the adding of Gaussian of constant height through the course of the simulation, so it is solved with the *Well-Tempered Metadynamics* (WTMetaD)[61].

In WTMetaD, the height of the Gaussian is decreased with simulation time according to:

$$W = W_0 e^{-\frac{V_G(S,t)}{k_B \Delta T}} \tag{2.16}$$

Where W_0 is the initial Gaussian height, ΔT an input parameter with a dimension of a temperature and k_B the Boltzmann constant. With this rescaling of the Gaussian height, the bias potential smoothly converges in the long time limit, but it does not fully compensate the underlying free energy:

$$V_G(S, t \to \infty) = -\frac{\Delta T}{T + \Delta T} F(S) + C \tag{2.17}$$

Where C is an immaterial constant and T the system's temperature. In the long time limit, the CVs thus sample an ensemble at a temperature $T + \Delta T$ which is higher that the system temperature T. The parameter ΔT can be chosen to regulate the extent of the free energy

exploration: $\Delta T = 0$ corresponds to standard MD, $\Delta T \to \infty$ to standard METAD. The setting of the ΔT is imposed by the setting of the *biasfactor*, defined as the ratio between the temperature of the CVs and the system's temperature:

$$\gamma = \frac{T + \Delta T}{T} \tag{2.18}$$

So, this last feature of the WTMetaD allows limiting the exploration of the CVs space only to regions of reasonable free energy. Indeed, by tuning the *biasfactor* according to the height of the typical free-energy barrier, one will avoid overcoming barriers that are much higher than that.

To recover the free energy profile of the biased simulation, a reweighting scheme is applied[62]. The weight of each configuration is given by equation (3.1):

$$\omega(R) \propto e^{\beta\left(V(s,t) - c(t) + V_{wall}(s)\right)} \tag{2.19}$$

Where $V(s,t)$ is the constructed bias potential (s is the value of the CV at a given time t), $\beta = 1/k_b T$ where k_b is the Boltzmann constant and T is temperature. $V_{wall}(s)$ is the bias due to the application of the upper wall and lower wall bias, and $c(t)$ is the reweighting factor, a time dependent offset bias calculated as:

$$c(t) = \frac{1}{\beta}\log\left(\frac{\int ds\, e^{-\beta F(s)}}{\int ds\, e^{-\beta F(s) + V(s,t)}}\right) \tag{2.20}$$

$$\beta F(s) = -\frac{\gamma V(s,t)}{k_b \Delta T} + \log\left(\int ds\, e^{\frac{\gamma V(s,t)}{k_b \Delta T}}\right) \tag{2.21}$$

Where ΔT is the hills temperature, $\gamma = \frac{T+\Delta T}{T}$ is the bias factor.

3 Cell-penetrating peptides adsorption on silica surfaces

In this chapter the adsorption mechanisms of cell-penetrating peptides onto silica surfaces is investigated by classical and enhanced molecular dynamics. Silica surfaces differ for ionization's state. Results suggest that the degree of surface ionization is fundamental in determining the strength of this interaction, quantified by free energy estimations.

3.1 Introduction

There are many reasons to account silica interaction with biomolecules. For instance, oxygen and silicon are the most abundant atomic species in the Earth's crust[63], forming numerous silica and silicate minerals. Silicon dioxide SiO_2, referred to as silica, is a solid compound, which appears in the form of crystalline minerals (principally quartz) and amorphous allotropic forms. Silica range of applications goes from making of glass, abrasives, filler for tires, catalysts supports to cosmetic, chromatography, biosensors and drug delivery. In the field of nanomedicine, the silica has been investigated as functionalization strategy of organic and inorganic nanoparticles. As a matter of facts, the intrinsic properties of the silica (high biocompatibility, optical transparency, chemical and colloidal stability, tunable porosity, easy surface modifications) prove its remarkable potential in biomedicine[64]. The silica coating of nanoparticles has been widely investigated since enhances the colloidal properties. Several studies have reported how the use of silica coating it's able to overcome the physicochemical limitations that the colloidal particles will be likely to encounter, such as low stability, high chemical reactivity and undesired aggregation processes[65–67]. The remarkable stability of the silica sols allows cations and positively charged molecules to be tightly attached to the polymeric silicate layer, at silica-water interfaces, under basic conditions[68], conferring both steric and electrostatic protection on the NPs cores and acting as dispersing agent of many electrostatic colloids. In addition, the silica coating leave subsequent space for further functionalization, allowing the NP to acquire theranostics features.

The physicochemical nature of the solid surface determines the kind of protein preferentially adsorbed, as well as the strength of the bond. Silica functionalities are mainly surface silanol groups (SiOH) and they interact with the polar groups of proteins. In this context, it is interesting to investigate the silica complex with cell-penetrating peptides (CPPs).

It is important to maintain the right conformation of the peptide in the adsorption process in order to enhance the cellular uptake of the NP. The CPPs are short chain of amino acid residues that enter the cell in a natural way helping facilitate the uptake of small and large biomolecules. In general, their composition is made up of a high relative abundance of

positively charged amino acids (lysine or arginine) or of alternating sequences of polar/charged and non-polar/hydrophobic residues. Several translocation mechanisms have been proposed to highlight the cellular uptake, but no real consensus has been achieved. In particular, three main mechanisms are defined: translocation through the formation of transient pores, direct penetration in the membrane and endocytosis-mediated pathway.

Nonetheless, the penetration mechanism depends upon the CPP and has yet to be completely defined. However, they have several applications in medicine as drug delivery agents and are used in the treatment of cancer as well as contrast agent for cell labelling. Thus, they can be used to design a magnetic nanoparticle, such as iron oxide NPs and their inorganic silica coating.

The specificity and strength of surface-peptide interactions has been attributed to the chemical nature of the surface, as well as the structure and conformation of the peptides and the surface-water interactions[69]. Above all, chemical bonding, hydrogen bonding, hydrophobic bonding and van der Waals forces are responsible for the adsorption mechanism[70].

The use of molecular dynamics simulations has been recognize to be helpful in the challenge of calculating protein structure on surface[71,72]. In particular, previous studies have been investigating the relation between peptides and silica surfaces by means of molecular dynamics and enhanced sampling techniques[73–78], elucidating the role of the electrostatic interactions on peptide-surface adsorption mechanism.

In this work, molecular dynamics and enhanced sampling techniques are employed to investigate the adsorption's mechanism of six CPPs onto three silica surfaces differing in the surface ionization's degree.

3.2 Materials and Methods

3.2.1 Preparation of the Amorphous Silica Surfaces

The silica surfaces have been downloaded by the Surface Model Database[79], in which several silica surfaces with full range of variable surface chemistry and pH (Q^2, Q^3, Q^4 with adjustable degree of ionization) and a silica force field – that well correlates the experimental data – can be found. The characterization of silica surfaces has involved X-ray Photoelectron Spectroscopy (XPS)[80], Fourier Transform Infrared Spectroscopy (FTIR), Time-of-Flight Secondary Ion Mass Spectrometry (ToF-SIMS), Extended X-ray Absorption Fine Structure (EXAFS), Sum Frequency Generation Spectroscopy (SFG), solid state NMR[81], contact angle[82], zeta potential measurements[80] and potentiometric titration[82,83].

These techniques can identify silicon environments on the nanoparticle surface (Q^4, Q^3, Q^2, Q^1 and Q^0) including the total density of silanol groups and sodium siloxide groups per surface area. As reported in Table 3.1, the majority of silica nanoparticles and porous glasses can be approximated as Q3 silica surface. Indeed, large nanoparticles of quartz at high pH in hydrated environments contain Q^2 surface environments – which consists of two silanol groups per superficial silicon atom ($=Si(OH)_2$) and mixed Q^2/Q^3 surface environments; silica surface after thermal treatment are distinguished by a higher proportion of Q^4 environments – which means siloxide bridges without silanol groups. As a matter of fact, most silica glasses and medium size nanoparticles are characterised by a 70-90% Q^3 environments on the surface ($\equiv Si(OH)$) – one silanol group per superficial silicon atom. Therefore, the type and area density of silanol groups thus depends on the particle size, thermal pre-treatment, synthesis protocol, humidity, etc.

Thereby, three variants of Q3 surfaces types were selected: a Q3 surface with 4.7 silanol groups per nm^2 (0% degree of ionization) – named *SiOH*; a 4.7 SiO(H,Na) per nm^2 and 0.42 SiO-Na+ per nm^2 (9% degree of ionization) – named *9SiO(H,Na)* – and a 4.7 SiO(H,Na) per nm^2 and 0.84 SiO-Na+ per nm^2 (18% degree of ionization) – named *18SiO(H,Na)*. The INTERFACE force field[79] has been employed for the surface topology. In Table 3.1 are shown the different model of silica surfaces in different conditions.

The models of the selected silica surfaces are visible in Figure SI 1.

Table 3.1 Guidelines of Silica Model for a known Silica substrate[79]

Type of silica substrate	1. Area density of silanol groups	2. Ionization to (SiO^- M^+)[a]	3. Surface topography
Quartz surfaces, silica nanoparticles >200 nm size, silica at pH > 9	Q^2 and Q^2/Q^3 (9.4 to 4.7 per nm^2)	pH 2: ~0 per nm^2 pH 5: ~0.5 per nm^2 pH 7: ~1.0 per nm^2 pH ≥9: ~1.5 per nm^2	Substrate-specific: smooth, rough, porous
Most silica glasses, porous silica, silica nanoparticles <200 nm size	Q^3 (4.7 per nm^2)	pH 3: ~0 per nm^2 (0%) pH 5: ~0.3 per nm^2 (6%) pH 7: ~0.6 per nm^2 (13%) pH ≥9: ~0.9 per nm^2 (20%)	
Silica surfaces and nanoparticles annealed at 200-1000 °C	Q^3/Q^4 and Q^4 (4.7 to 0 per nm^2)	pH 4: ~0 per nm^2 pH 7: 0-0.6 per nm^2 depending on Q^3 content	

3.2.2 Preparation of the Cell-Penetrating Peptides Models

The pAntp and TAT were 24 extracted from the Protein Data Bank (PDB ID: 1OMQ[84], and 1TAC respectively). The remaining peptides, (ARG)9, CADY, Pep and MAP, were built by the PEP-FOLD 3 server[85]. The CHARMM36[86] force field was employed to define the peptides topologies, since it has been demonstrated that INTERFACE and CHARMM force fields are compatible and can be used together[79]. The chosen peptide are shown in Figure 3.1

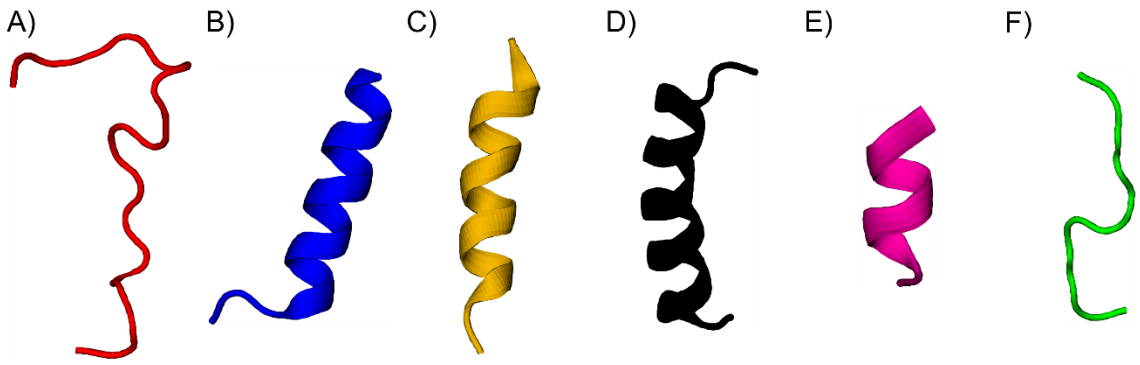

Figure 3.1 Selected cell-penetrating peptide. A) CADY; B) MAP; C) pAntp; D) PEP; E) (ARG)9; F) TAT

3.2.3 System Setup and Configuration

Based on the model described above, twelve molecular systems were set up, each consisting of a CPP interacting with one of the two silica surfaces. The centre of mass (COM) of each CPP was placed at about 2 nm from the surface COM, as shown in Figure 3.2. Each system was placed in a rectangular box of 6 nm x 6 nm x 8 nm and explicitly solvated – the number of interacting particles is reported in Table 3.2. The TIP3P[87] model was adopted to describe water topology. Ions were added to neutralize the system charge.

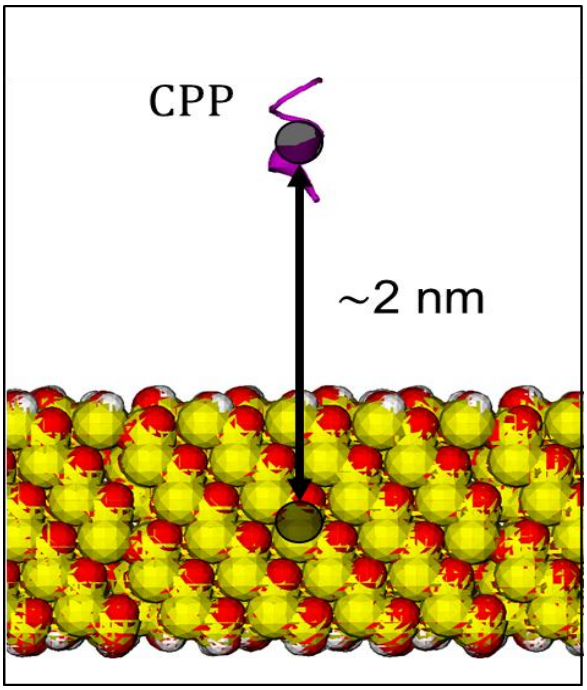

Figure 3.2 Visual inspection of the system peptide-silica surface. Water was removed for clarity. The Si atoms are represented in yellow, the O atoms in red and the H atoms in white.

Table 3.2 Charge and number of molecules for each CPP-surface system.

		Silica Surface Q3 0%		**Silica Surface Q3 9%**		**Silica Surface Q3 18%**	
	Peptide Charge	# Water Molecules	# Total Atoms	# Water Molecules	# Total Atoms	# Water Molecules	# Total Atoms
CADY	+5	8422	27845	8415	27824	8396	27769
MAP	+5	8459	27872	8452	27851	8433	27796
pAntp	+7	8450	27875	8443	27854	8424	27799
PEP	+3	8437	27900	8430	27879	8411	27824
(ARG)9	+9	8477	27843	8470	27822	8451	27767
TAT	+8	8482	27874	8475	27853	8456	27798

3.2.4 Molecular Dynamics

All the simulated systems were first minimized by means of the Steepest Descent energy minimization[88], then equilibrated in an NVT ensemble for 100 ps (T=300 K), by means of the V-rescale algorithm[89] (dt=2 fs, τ=0.1). Then, an equilibration in an NPT ensemble for 100 ps was carried out, adopting the Berendsen[90] isotropic barostat and the V-rescale thermostat. The isothermal-isobaric ensemble simulations were conducted applying position restraint on both the CPP backbone and the surface Si atoms (force constant of 1000 kJ mol^{-1} nm^{-2}). Finally, a 100 ns long MD simulation was performed on each system, using the Noose-Hoover[91] and the Parrinello-Rahman[92] as temperature and pressure coupling respectively. The LINCS [93] algorithm was used to constraint hydrogen bond. Electrostatic interactions were calculated with the Particle-Mesh Ewald[55] method with a short range cut off of 1.2 nm. The same cut off was employed to treat the Van der Waals interactions. All systems were periodic in x, y and z dimensions. Trajectory were collected every 10 ps. The peptide-surface distance was tracked with PLUMED 2.4.1[94] and a restraining potential was applied on the distance component (x, y, z) in order to limit the region of the phase space accessible during simulation (K=1000 kJ/mol), so that the peptide was forced to explore the top of the surface.

All MD simulations were performed using GROMACS 5.1[95] package while the Visual Molecular Dynamics (VMD)[96] software was employed for visual inspection of the simulated systems. Analysis of the Secondary Structure were performed applying both the Dictionary of Protein Secondary Structure (DSSP)[97] and the STRIDE web server[98].

3.2.5 Metadynamics

Following the NPT equilibration, metadynamics simulations were carried out on each system in order to define the binding free energy of each peptide with the silica surfaces. The Well-Tempered Metadynamics (WTMetaD)[61] was employed. The collective variable (CV) biased was the distance between the peptide COM and the surface COM in order to sample the free energy landscape. The Gaussian height was set to 1 kJ mol^{-1}, the bias factor was set to 3 for the CPPs-SiOH, to 7 for the CPPs-9SiO(H,Na) systems and to 12 for the CPPs-18SiO(H,Na) systems, the Gaussian deposition rate was set to 1 hill/ps for all the metadynamics simulations as in other studies[76]. The Gaussian width σ was set to 0.05 nm and its value was computed as half of standard deviation of the unbiased CV[99]. In Table 3.3 are summarized the former parameters for each system. An harmonic restraint was applied on the distance between the CPP and the silica substrate in all directions (k=5000 kJ mol^{-1} for the SiOH surface; k=10000 kJ mol^{-1} for the 9SiO(H,Na) and 18SiO(H,Na)) to promote the accelerated sampling of the region of interest.

The free energy was recovered by applying the reweighting scheme described in the Materials and Method chapter. These weights were used to estimate the free energy obtained as the natural logarithm of the sum of weight in each bin. The grid spacing was set as $1/5$ of the Gaussian width σ which is reasonable for most applications.

All the WTM simulations were computed using GROMACS 5.1[95] package and the PLUMED 2.4.3[94] open-source plug-in.

Table 3.3 Bias Factor and Gaussian width value for each metadynamics simulation.

	Silica Surface Q3 0%			**Silica Surface Q3 9%**			**Silica Surface Q3 18%**		
	Bias Factor (BF)	Gaussian width (σ)	Total simulation time	Bias Factor (BF)	Gaussian width (σ)	Total simulation time	Bias Factor (BF)	Gaussian width (σ)	Total simulation time
CPPs	3	0.05	*150 ns*	7	0.05	*250 ns*	12	0.05	*250 ns*

3.3 Results

3.3.1 Molecular Dynamics Results

The overall stability of the systems, calculated as the RMSD on the C-alpha fitted on the C-alpha of each CPP, can be found in Figure SI 5, Figure SI 6 & Figure SI 7.

The distance between the peptide's centre-of-mass (COM) and the surface's COM for each system is reported in Figure SI 2, Figure SI 3 & Figure SI 4. In Figure 3.3, the distance averaged on the last 50 ns for each system is shown. It is easy to see how each peptide was more attracted by the protonated surfaces, in fact the peptides interacting with the 9SiO(H,Na) and the 18SiO(H,Na) show lower value, confirming the longer contact with the surface.

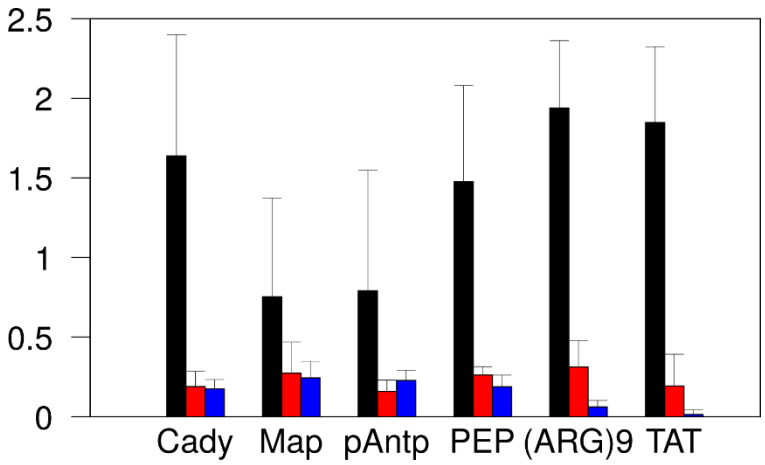

Figure 3.3 Mean distance and standard deviation calculated in the last 50 ns for each system: peptide-surface SiOH in navy; peptide-surface 9SiO(H,Na) in red and peptide-surface 18SiO(H,Na) in blue.

In Figure 3.4, it is represented the contact area as mean value and its standard deviation, between the peptides and the surfaces. The contact area is shown as total (black), hydrophilic (blue) and hydrophobic (red). It is to notice that all the surfaces are hydrophilic, so the hydrophobic contribution depend upon the peptides' residues. The surfaces with greater degree of ionization show a bigger affinity with the peptides – it is to mention the behaviour of the (ARG)9 peptide, which interacts only with the 9SiO(H,Na) and 18SiO(H,Na) surfaces.

The increment in the contact area seem to be almost due to hydrophilic interaction, which are determined by the polar residues of the peptide with whom the silanol groups of the surface can establish H-bond interactions[100] and ion pairing, which are the most important contributions in peptides' adsorption[74].

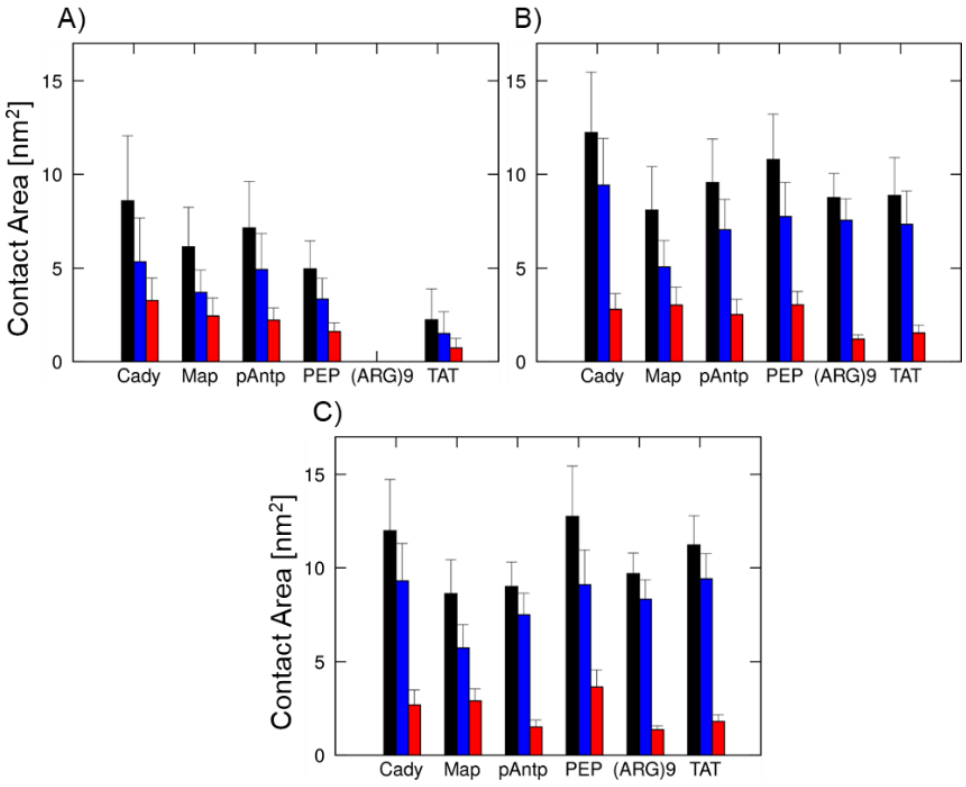

Figure 3.4 Contact area of the peptide with the SiOH surface (A), 9SiO(H,Na) (B) and 18SiO(H,Na) (C). The total area is shown in black, the hydrophilic area in blue and the hydrophobic area in red.

In Table 3.4 the most interacting residue forming H-bond, donator or acceptor, per peptide in each system are grouped.

Table 3.4 Resides most involved in H-bond formation per each system. The polar residues are highlighted in blue, the hydrophobic residues are highlighted in green and the charged residues are highlighted in red.

# Residue (1 2 3 4 5 6 7)	Surface SiOH	Surface 9SiO(H,Na)	Surface 18SiO(H,Na)
CADY	TRP ALA ARG	GLY ARG	GLY TRP ARG
MAP	LYS ALA	LYS ALA	ALA LYS
pAntp	GLN ASN TRP LYS ARG	ARG LYS	ARG
PEP	THR GLU GLN ARG	LYS ARG	ARG
(ARG)9	ARG	ARG	ARG
TAT	TYR ARG	TYR GLN ARG	TYR

These residues were extracted by Figure SI 8, Figure SI 9 & Figure SI 10 and classified in polar, charged and hydrophobic amino acids. In the case of the surfaces 9SiO(H,Na) and 18SiO(H,Na) the residues more involved in the H-bond formation are charged residues. All the silanol groups (SiOH) are subject to deprotonation-protonation equilibria in water, thereby the release of Na ions by the protonated surfaces get to the formation of negative silanol groups SiO^- that lead the interactions with the positively charged peptides and their polar/charged residues, linking the peptide on the surface.

In Figure 3.5, Figure 3.6 & Figure 3.7 the mean and the standard deviation over the contact time of the minimum distance per residue from the surface are represented. The minimum distance was computed as the minimum value between each atom of peptide residues and each atom of the silica surfaces. It is clear that the peptides interacting with the 9SiO(H,Na) and the 18SiO(H,Na) surfaces show overall lower values per residue and lower standard deviation, because of the much longer contact with the surface.

Not all these residues are involved in H-bond formation, suggesting that other contributions may come from ion pairing, as well as less energetic ion-dipole, dipole-dipole and Van der Waals interactions. These contributions are determined by the isoelectric point (pI) and the conformational flexibility of the peptides[74]. Nonetheless, the aqueous environment plays also a role in orienting the peptides onto the surface: as observed in previous works[75] the superficial water thwarts the peptide in establishing H-bond and ion pairing with the superficial atoms of the surface. The thickness of this interfacial water layer is governed by the silica surface characteristics and the protein molecules, whose adsorption leads to a local decrease of layer size[101].

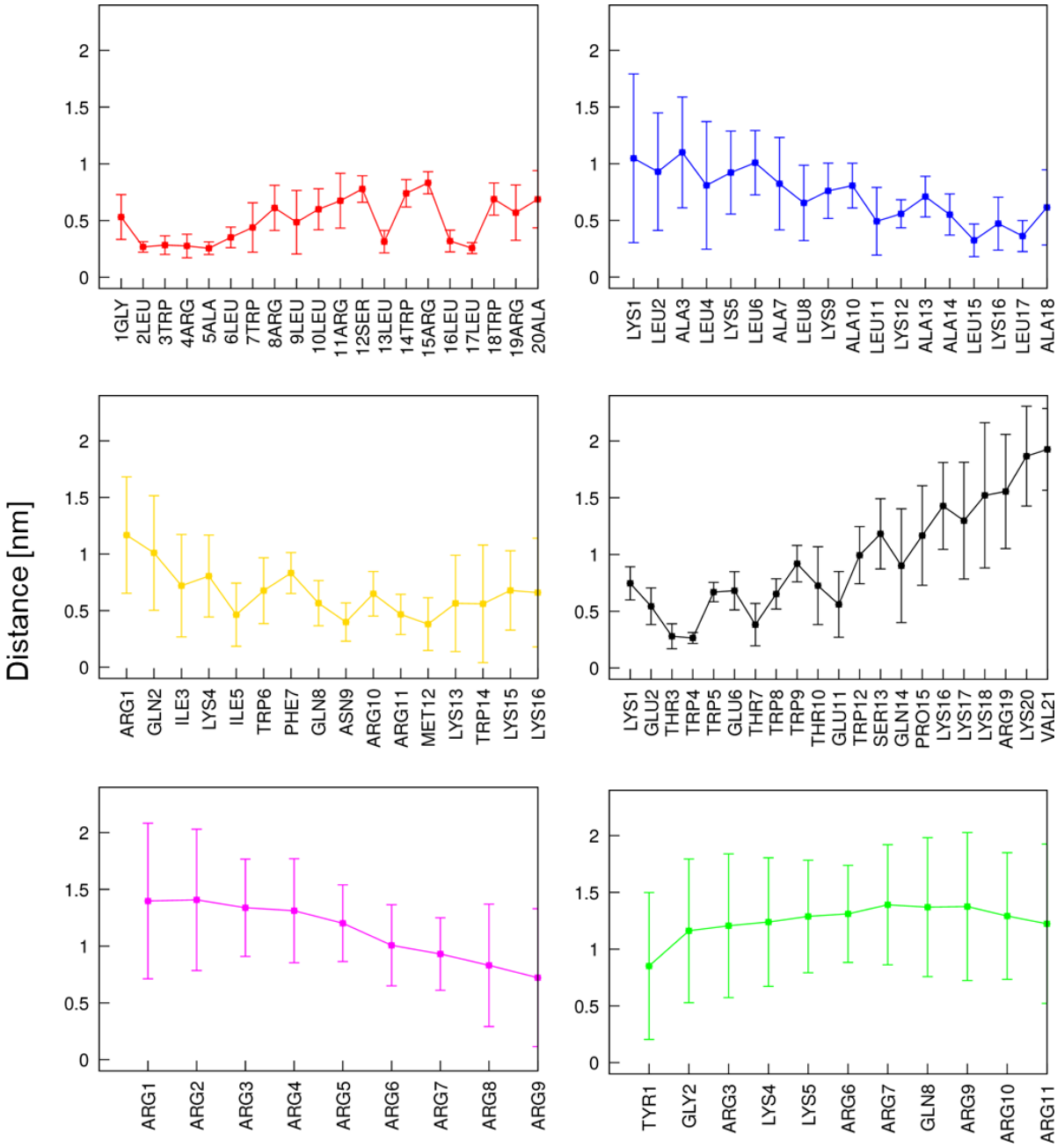

Figure 3.5 Equilibrium distance of the residue of the peptides to the SiOH. Each value was obtained averaging the minimum distance over the peptide-surface contact times. CADY (red); MAP (blue); pAntp (yellow); PEP (black); (ARG)9 (magenta); TAT (green)

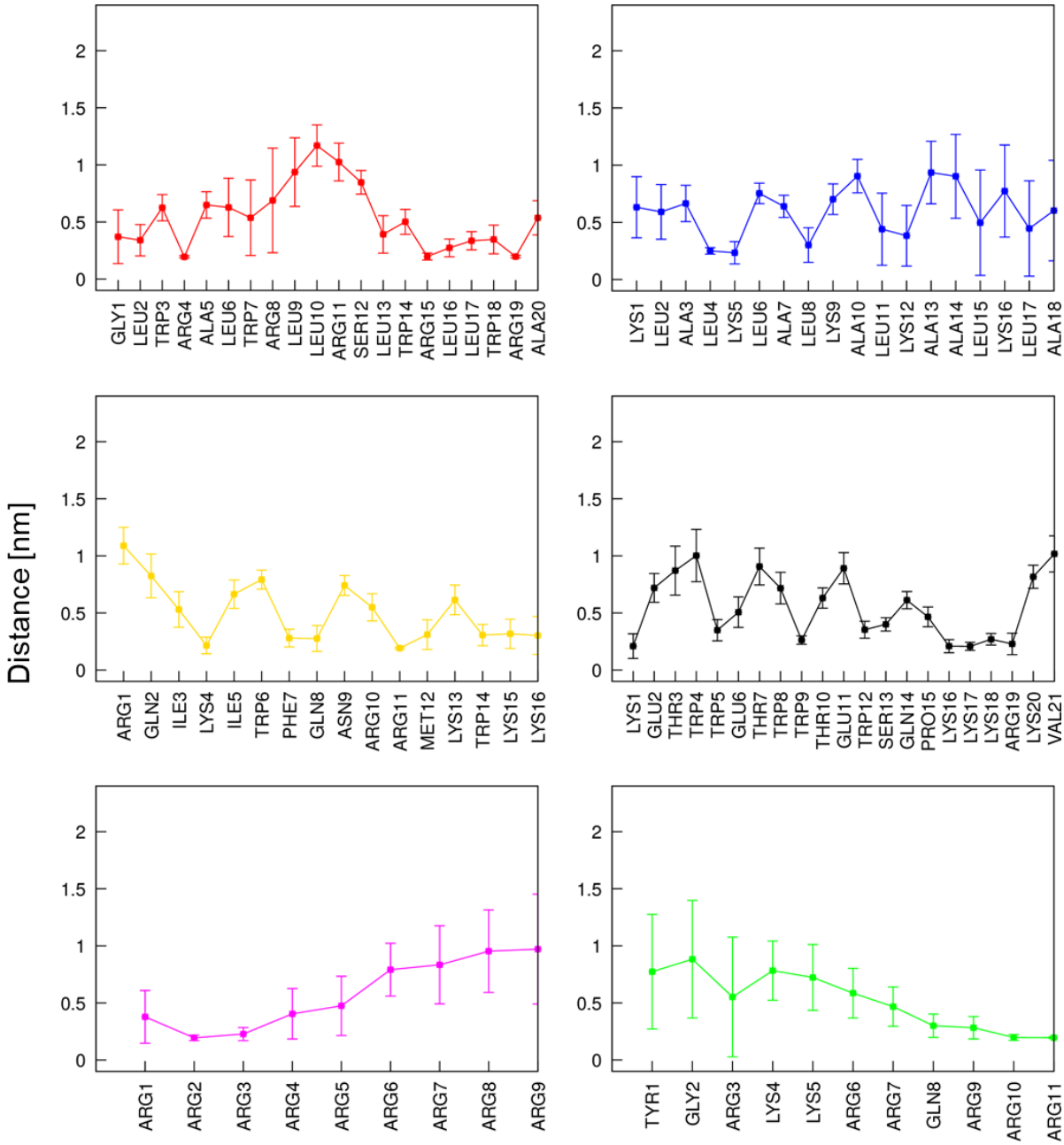

Figure 3.6 Equilibrium distance of the residue of the peptides to the 9SiO(H,Na). Each value was obtained averaging the minimum distance over the peptide-surface contact times. CADY (red); MAP (blue); pAntp (yellow); PEP (black); (ARG)9 (magenta); TAT (green).

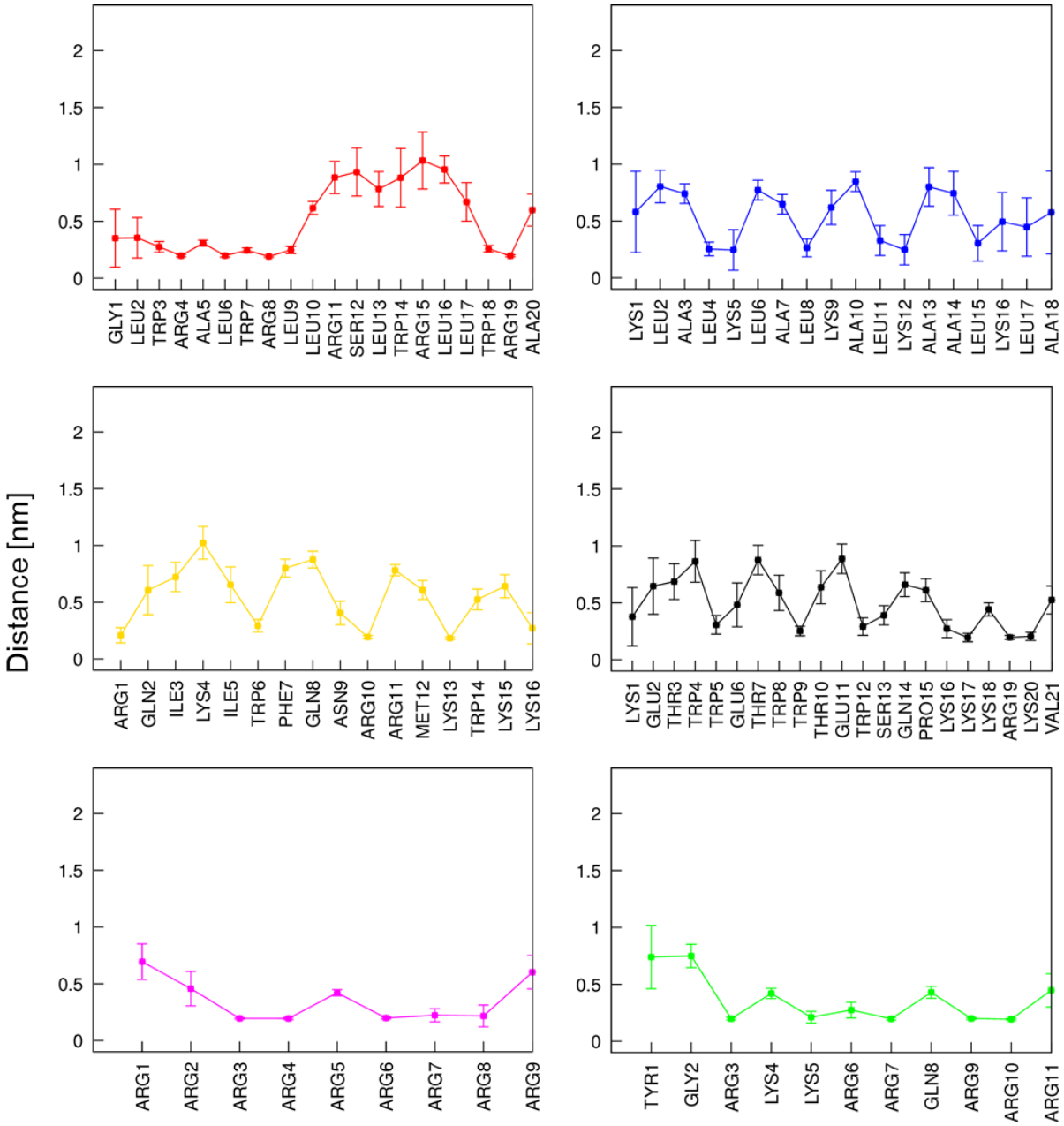

Figure 3.7 Equilibrium distance of the residue of the peptides to the 18SiO(H,Na). Each value was obtained averaging the minimum distance over the peptide-surface contact times. CADY (red); MAP (blue); pAntp (yellow); PEP (black); (ARG)9 (magenta); TAT (green).

In Figure 3.8 are shown three snapshot of the systems CADY peptide – silica surface (SiOH surface Figure 3.8 A-C; 9SiO(H,Na) surface Figure 3.8 D-F; 18SiO(H,Na) surface Figure 3.8 G-I). The behaviour of the CADY peptide changes with the surface: although the starting configuration of the peptide is the same in all simulations, only with the SiOH surface it can be observed an alpha-helical structure.

Regarding the SiOH surface, the C-terminal residues guide the adsorption mechanism: the ALA20 and the ARG19 reached the surface (Figure 3.8 A); then the N-terminal tail is pushed on the surface (Figure 3.8 B). In the end, the N-terminal tail is interacting with the surface, while the C-terminal tail has changed its orientation drifting from the surface (Figure 3.8 C).

Conversely, the contact with the 9SiO(H,Na) surface starts with the N-terminal tail of the peptide, and it is quite guided by the GLY1 residue (Figure 3.8 D). Indeed, the GLY1 reaches the surface and shove the C-terminal tail onto the surface (Figure 3.8 E), resulting in the end of the interaction in an upside-down twist, where the C-terminal tail is interacting and the GLY1 is located near the surface (Figure 3.8 F).

Likewise, the contact with the 18SiO(H,Na) surface begin with the N-terminal tail of the peptide. As before, the GLY1 is responsible for the anchoring of the CADY peptide (Figure 3.8 G) , dragging the C-terminal tail onto the surface (Figure 3.8 H). In the end, the GLY1 and the ARG19 residues link both the tails to the surface (Figure 3.8 I).

The interacting tail of the peptide may be completely random in the case of the SiOH systems. On the contrary, the siloxide groups of the 9SiO(H,Na) and 18SiO(H,Na) surfaces might influence the peptide in interacting with the ammonium group of the N-terminal tail. The presence of charged residues in the C-terminal tail is to be accounted for the final configuration twist (Figure 3.8 F,I).

The mechanism of adsorption of the CADY peptide is more or less equal to the other peptides, whose adsorption's mechanisms is described in Figure SI 11 (MAP), Figure SI 12 (pAntp), Figure SI 13 (PEP), Figure SI 14 ((ARG)9) & Figure SI 15 (TAT).

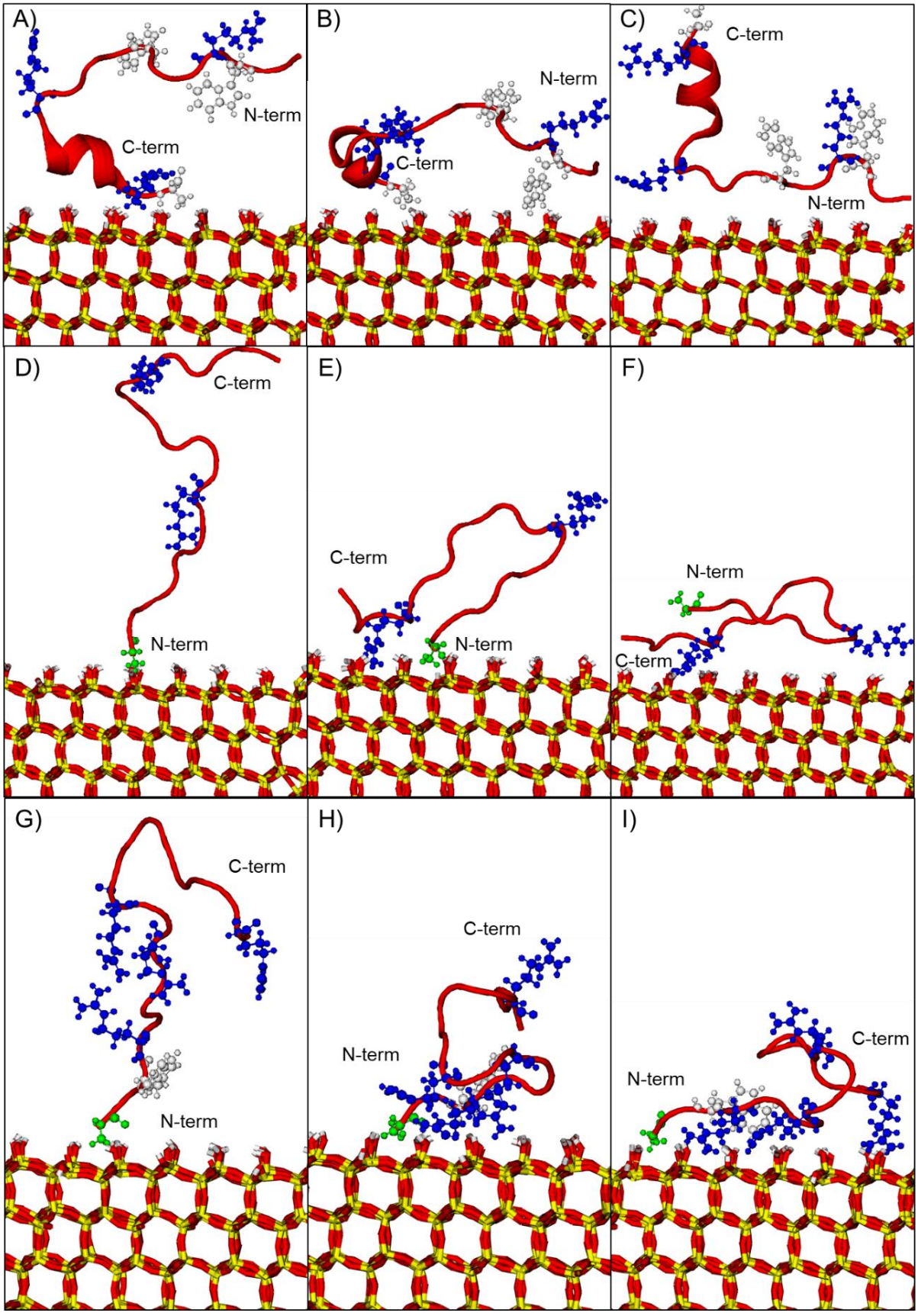

Figure 3.8 Snapshots of the contacts between the CADY peptide with the SiOH (A,B,C), the 9SiO(H,Na) (D,E,F) and the 18SiO(H,Na) (G,H,I) surfaces: A,D,G) Initial contact; B,E,H) during contact; C,F,I) final configuration. The residues from Table 3.4 are highlighted: non-polar residues in white (ALA, TRP); basic residues in blue (ARG); polar residues in green (GLY). The N-term and the C-term are highlighted.

In Figure 3.9, Figure 3.10 & Figure 3.11 the complete secondary structure evolution of each peptide-surface system is shown. It is to mention that MAP, pAntp and PEP conserve their folded structures in all the systems.

The behaviour of the CADY peptide is different in all the systems: in the CADY-SiOH system, in the first $20\,\mathrm{ns}$ the C-terminal tail residues acquire an alpha-helix conformations, which is mostly conserved when it reaches the surface (around $20-60\,\mathrm{ns}$) and it is recovered in the last $20\,\mathrm{ns}$. As regards the others two systems, there is no evidence of alpha-helical structure, resulting or in a more unfolded conformation (Figure 3.10 A) or in an interchange of bend and turn structures (Figure 3.11 A). This behaviour is reflected in the RMSD value (Figure SI 5, Figure SI 6 & Figure SI 7) that in the case of MAP, pAntp, PEP, (ARG)9 and TAT peptides limits their conformational space and their flexibility, while the fluctuations of the CADY peptide are more accentuated.

For what concerns the (ARG)9 and TAT peptides, which are the shortest peptides, have similar behaviour in all the systems. They present unfolded structures at the end of the simulations and throughout the simulations they conformed into partial turn and bend, no helical structure is reported (Figure 3.11 E-F), except the first ns of the (ARG)9-SiOH system, where the peptide did not interact with the surface.

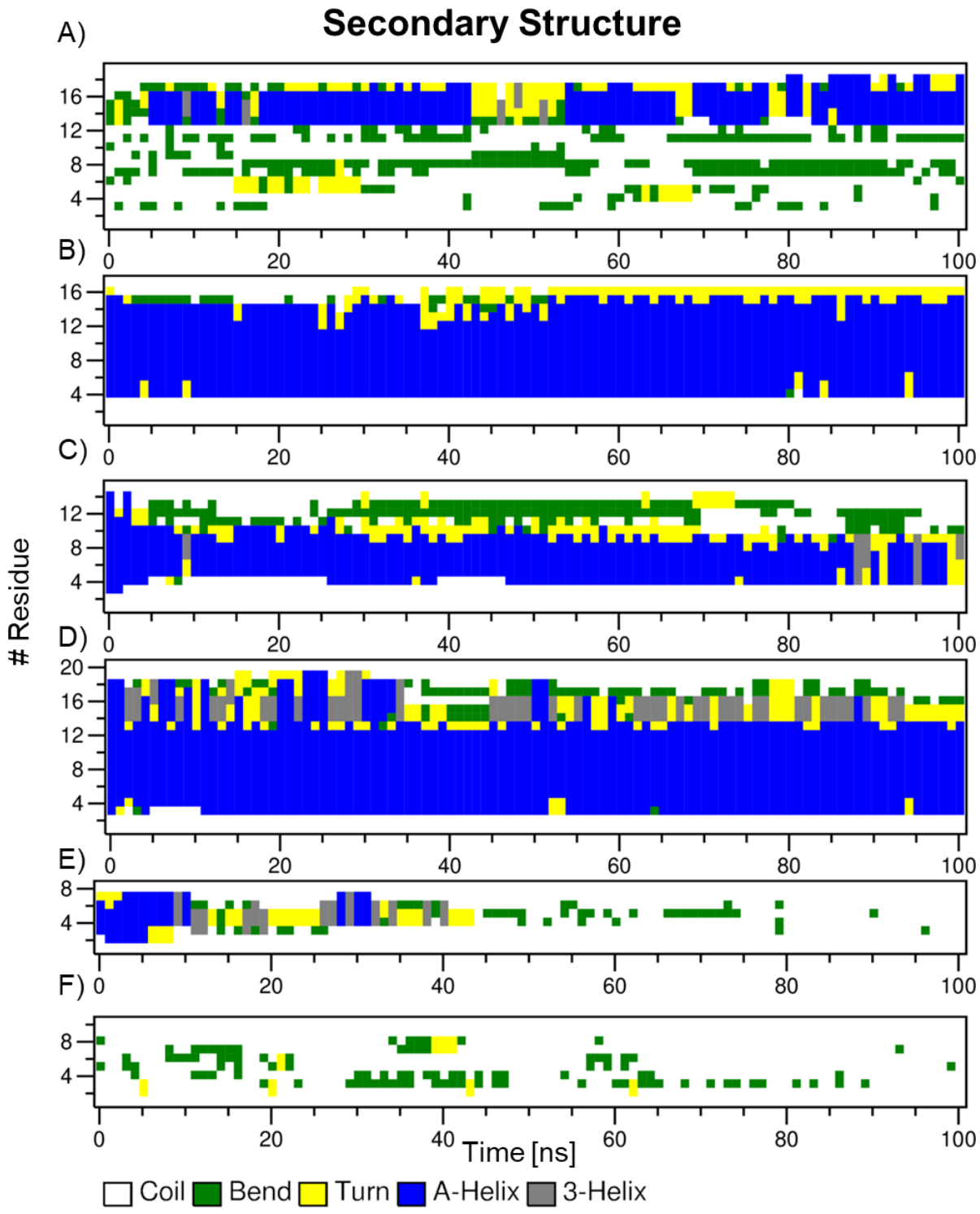

Figure 3.9 Complete structural evolution of the peptides interacting with the SiOH surface. A) CADY peptide; B) MAP peptide; C) pAntp peptide; D) PEP peptide; E) (ARG)9 peptide; F) TAT peptide.

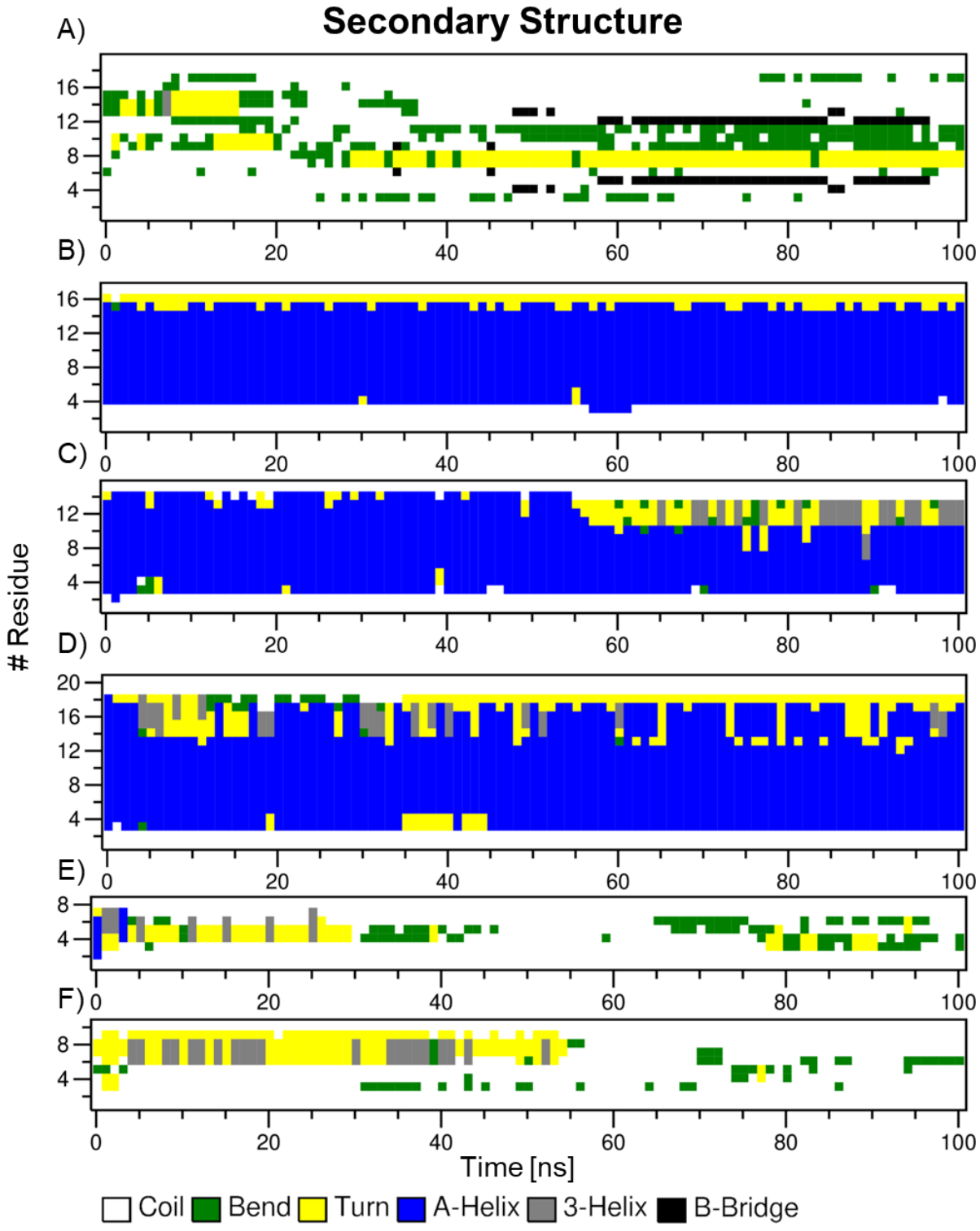

Figure 3.10 Complete structural evolution of the peptides interacting with the 9SiO(H,Na) surface. A) CADY peptide; B) MAP peptide; C) pAntp peptide; D) PEP peptide; E) (ARG)9 peptide; F) TAT peptide.

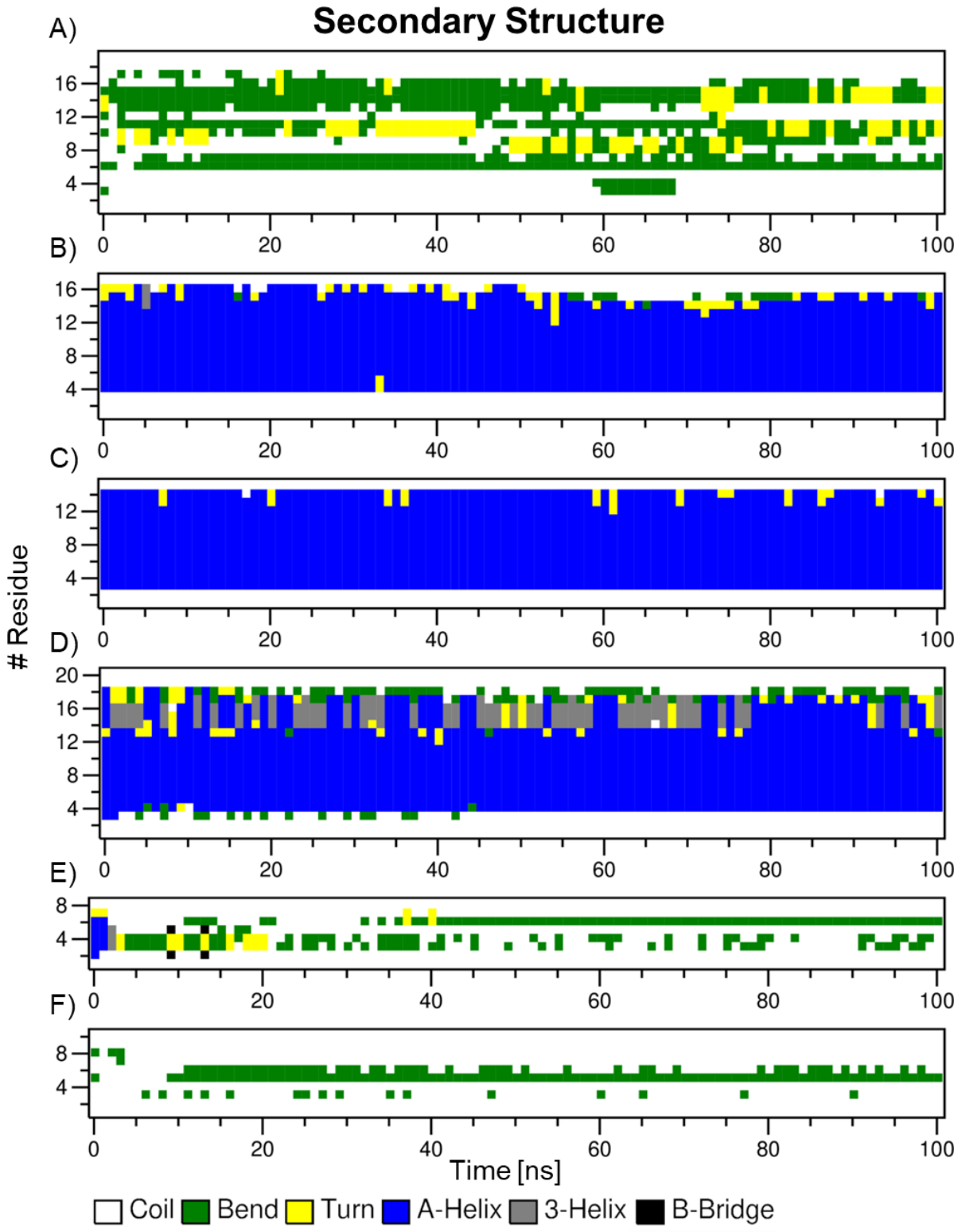

Figure 3.11 Complete structural evolution of the peptides interacting with the 18SiO(H,Na) surface. A) CADY peptide; B) MAP peptide; C) pAntp peptide; D) PEP peptide; E) (ARG)9 peptide; F) TAT peptide.

3.3.2 WTMetaD Results

In Figure 3.12 is reported the evolution of the CV thought the simulation time of the peptides in the SiOH systems. All the peptides explore multiple times the conformational space, reaching out for the surface and leaving numerous times. The convergence analysis and the CV evolution of all the systems are described in Figure SI 16-18.

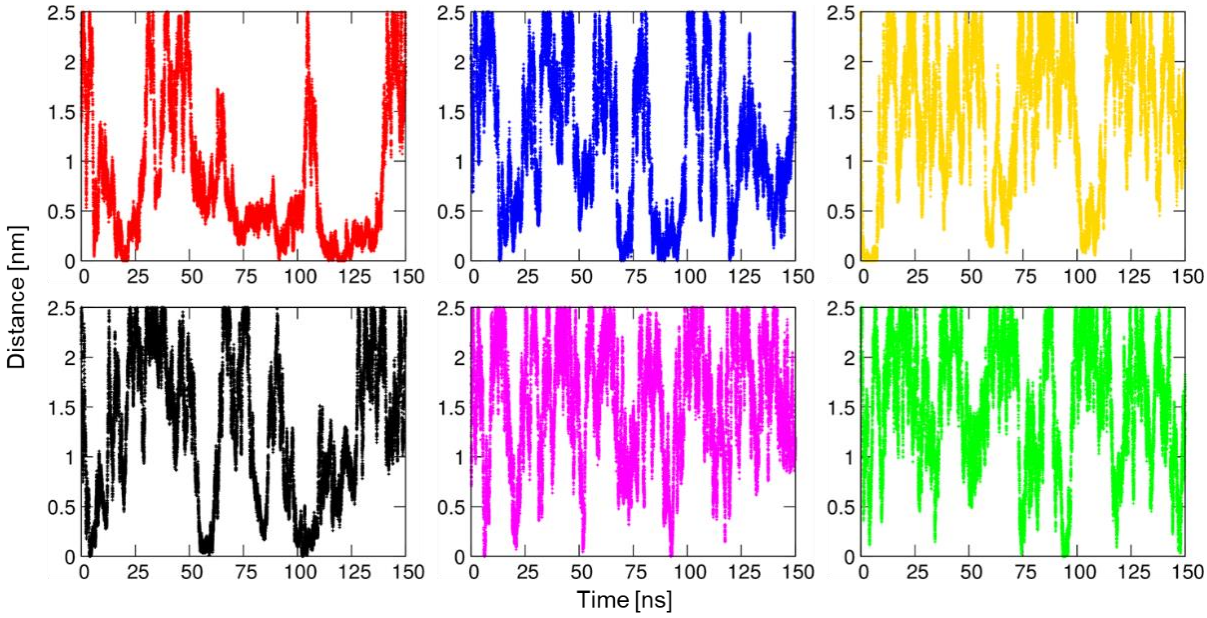

Figure 3.12 Evolution of the distance CV for each CPP-SiOH system. CADY peptide in red; Map peptide in blue; pAntp peptide in yellow; PEP peptide in black; (ARG)9 peptide in magenta; TAT peptide in green.

The free energy profile as a function of the distance CV are reported in Figure 3.13. These profiles were recovered through the reweighting algorithm explained in the Materials and Methods chapter.

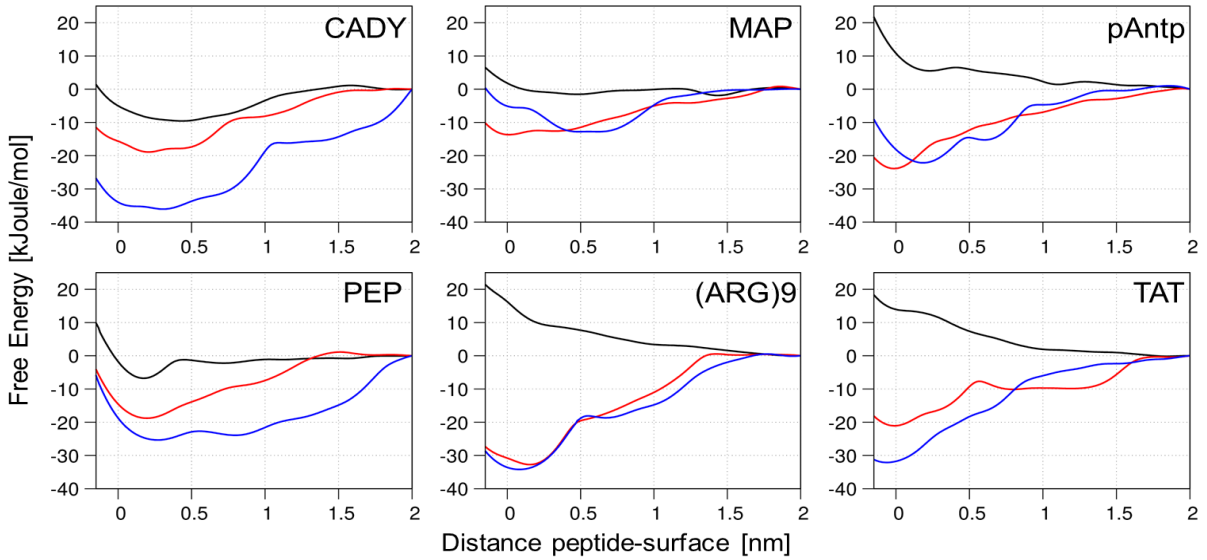

Figure 3.13 Free energy profile of the CPPs interacting with the silica surfaces: SiOH (black), 9SiO(H,Na) (red), 18SiO(H,Na) (blue).

Concerning the SiOH surface, only the CADY and PEP peptides show energy wells ($\Delta G \cong -10\ \mathrm{kJ/mol}$ and $\Delta G \cong -7\ \mathrm{kJ/mol}$ each), located at a distance value of $\sim 0.5\ \mathrm{nm}$ and $0.2\ \mathrm{nm}$ respectively. These values are 4 and 3 times higher than the thermal fluctuations ($k_B T$), thus indicating the existence of a metastable state near the surface. All the remaining peptides show no remarkable energy barrier. This is in line with the MD results, in a sense that the existence of the complex CPP-SiOH is not observed for those free energy profiles with no metastable minima.

In comparison with the 9SiO(H,Na) and 18SiO(H,Na) surfaces (red and blue lines in Figure 3.13), all the peptides show deeper energy well for a distance value in the range of $0 - 0.5\ \mathrm{nm}$, confirming the importance of the surface ionization state and therefore the best adsorption affinity. In the 9SiO(H,Na) system (red line in figure Figure 3.13), the TAT peptide shows a metastable state in the $0.7 - 1.3\ \mathrm{nm}$ region, and an energy barrier separating the minimum in the $0 - 0.5\ \mathrm{nm}$ region. This barrier is easily overcome by the thermal fluctuation.

The same considerations can be made on the other peptides interacting with the 18SiO(H,Na) surface, such as the pAntp that shows two energy well, one deeper than the other ($\Delta G \cong -15\ \mathrm{kJ/mol}$ and $\Delta G \cong -22\mathrm{kJ/mol}$).

In Figure 3.14 is reported the energy well of the stable state for all the systems in the $0 - 0.5\ \mathrm{nm}$ basin. These results confirm what previously seen in Figure 3.13, since both the protonated surfaces show negative values of ΔF (9SiO(H,Na) in red, 18SiO(H,Na) in blue) while only three peptides (CADY, MAP and PEP) show an affinity with the SiOH surface and are in line with the results from the classical MD simulations.

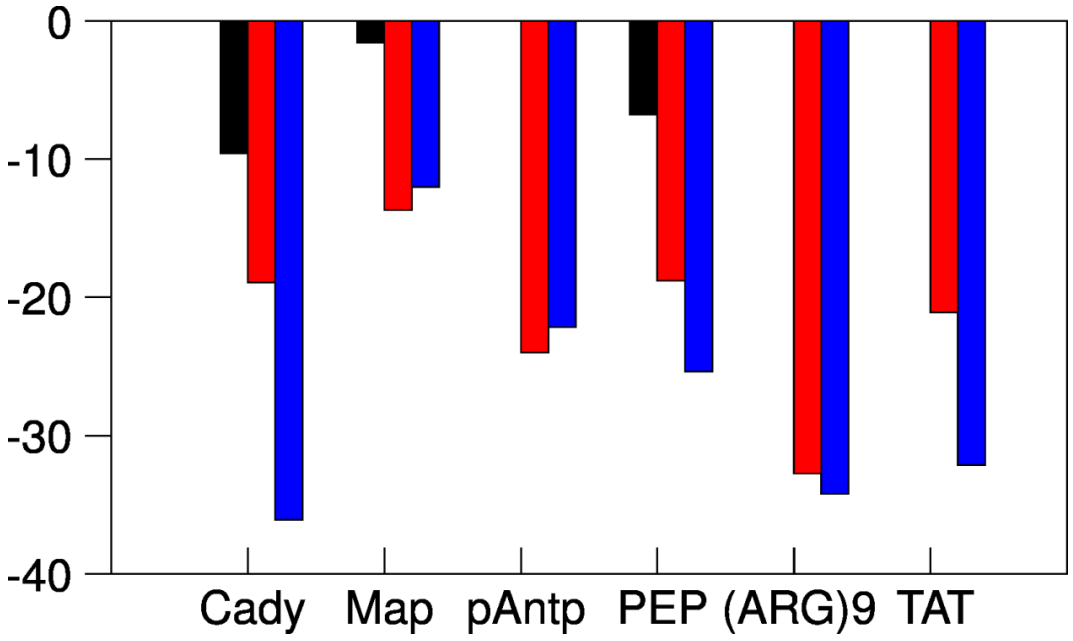

Figure 3.14 Minimum of the free energy for each peptide-surface system. SiOH (black), 9SiO(H,Na) (red), 18SiO(H,Na) (blue).

3.4 Discussion

The use of NPs in nanomedicine has grown in the last decade, since the NPs have demonstrated their efficacy as the next generation of targeted drug delivery[102,103]. Several types of iron oxide NPs have been developed and the choice – so far – is represented by the *magnetite*, easy to deal with synthesis processes and highly biocompatible[66,67]. Nonetheless, their high surface-to-volume ratio allows a very efficient functionalization, but it also leads to aggregation problems and loss of magnetism and dispersibility. In order to improve the iron oxide MNPs, several coatings have been investigated to improve their biocompatibility, magnetic properties, colloidal stability, shape and size. The use of MD simulation has proven its efficacy in describing the effect of different NP coating and their interaction with organic molecules and membranes. In particular, classical molecular dynamics simulation and enhanced sampling techniques have been employed to provide insight into the binding mechanism of peptides adsorption onto silica surfaces[74–78,100]. The use of silica coating can provide further functionalization with biomolecules of the MNPs, like CPPs. The conjugation of peptides to silica offers a possible route to design new drug delivery systems, improving the cellular uptake and the efficacy of the cargo delivery without significant damage[104,105].

In this context, an investigation of six cell-penetrating peptides onto three silica surfaces has been carried out, providing an estimation of the CPP-surface binding free energy by means of Well-Tempered Metadynamics. In particular, the effect of the surface ionization's state was considered, demonstrating the importance of the silica surface properties on the binding affinity.

These results confirm that the degree of ionization plays an important role in the electrostatics of the systems, facilitating the adsorption of the peptides. Above all, the 9SiO(H,Na) and the 18SiO(H,Na) have adsorbed all the studied peptides and, as pointed out in several studies[69,72,76,106], this behaviour has to be expected, since the protonated surface presents negatively charged SiO^- groups thus attracting the cationic peptides. Besides, as seen in Figure 3.8, the adsorption of the peptides onto the ionized surfaces are guided by the ammonium of the N-terminal residues, which is in agreement with other studies[74].

Moreover, the electrostatic non covalent interactions are hugely involved in the peptide-silica adsorption. The residues from Table 3.4, involved in the H-Bond formation with the silica surfaces are mostly polar and charged residues, which are normally found at the surface of proteins[69]. Also, the arginine plays an important role since it appears to drive the adsorption mechanism of the peptide on the silica surface[107].

4 Conclusion

Magnetic iron oxide nanoparticles (MNPs) represent a breakthrough in the field of nanomedicine and their applications range span from diagnosis to therapy. In particular, the MNPs are used in targeted drug delivery, magnetic resonance imaging (MRI), magnetic hyperthermia, bio sensing, cell labelling etc. The industry development of the last decade has achieved proper control over particle size, shape, crystallinity, polydispersity and magnetic properties and several synthesis methods have been investigated. To overcome the problems related to the high chemical activity, air oxidation, aggregation and toxicity, different functionalization strategies have been proposed. These strategies are based upon grafting or coating of inorganic and organic materials, such as polymers, biomolecules, surfactants and silica. The most common compound for preparing the MNPs is represented by the silica, since it provides stability, biocompatibility, hydrophilicity and it can also be used to further functionalization to facilitate the binding to several ligands. In this context, the cell-penetrating peptides can improve the cellular uptake of the MNPs in a natural, biological way. Besides, the CPPs can be used to deliver small and large cargo into the cell without provoking any damages.

The aim of this master thesis was to investigate the physical adsorption of the CPPs onto silica surfaces, in order to determine the underlying interactions. In particular, six cationic CPPs are presented and their relation with silica surfaces is investigated in all-atom simulations. Also, a quantitative estimation of the binding energy is provided by means of enhanced sampling approach. The influence of the surface ionization state on the adsorption behaviour was also investigated by employed three silica surfaces differing in ionization state (0%, 9%, and 18%). It is to notice that the surfaces do not present an excess in charge, since they are completely neutral, but the ionization state is responsible for the formation of a surface charge distribution.

Both the 9% and 18% surfaces result as best models in terms of CPPs adsorption, confirming that the area density of sodium siloxide groups is critical for selective adsorption. Also, the adsorption is modulated by the ammonium groups in the N-terminal tail of the peptides and by the ARG residues, through the formation of ion pairs with the negative siloxide groups.

In conclusion, as future perspective it could be interesting the study of the conjugated CPP-silica surface interacting with the cellular membrane, to understand if the conformations assumed by the peptides onto the surface can affect their penetrating capability in order to improve and modulate the NPs features.

References

(1) Celia, C.; Carafa, M.; Cilurzo, F.; Paolino, D.; Di Marzio, L.; Wolfram, J.; Anna Ventura, C.; Gentile, E. Liposomal Chemotherapeutics. *Futur. Oncol.* **2013**, *9* (12), 1849–1859. https://doi.org/10.2217/fon.13.146.

(2) Shen, J.; Kim, H. C.; Mu, C.; Gentile, E.; Mai, J.; Wolfram, J.; Ji, L. N.; Ferrari, M.; Mao, Z. wan; Shen, H. Multifunctional Gold Nanorods for SiRNA Gene Silencing and Photothermal Therapy. *Adv. Healthc. Mater.* **2014**, *3* (10), 1629–1637. https://doi.org/10.1002/adhm.201400103.

(3) Molinaro, R.; Wolfram, J.; Federico, C.; Cilurzo, F.; Di Marzio, L.; Ventura, C.; Carafa, M.; Celia, C.; Fresta, M. Polyethylenimine and Chitosan Carriers for the Delivery of RNA Interference Effectors. *Expert Opin. Drug Deliv.* **2013**, *10*. https://doi.org/10.1517/17425247.2013.840286.

(4) Choi, K. M.; Choi, S. H.; Jeon, H.; Kim, I. S.; Ahn, H. J. Chimeric Capsid Protein as a Nanocarrier for SiRNA Delivery: Stability and Cellular Uptake of Encapsulated SiRNA. *ACS Nano* **2011**, *5* (11), 8690–8699. https://doi.org/10.1021/nn202597c.

(5) Meng, L.; Chen, R.; Jiang, A.; Wang, L.; Wang, P.; Li, C. Z.; Bai, R.; Zhao, Y.; Autrup, H.; Chen, C. Short Multiwall Carbon Nanotubes Promote Neuronal Differentiation of PC12 Cells via Up-Regulation of the Neurotrophin Signaling Pathway. *Small* **2013**, *9* (9–10), 1786–1798. https://doi.org/10.1002/smll.201201388.

(6) Shen, J.; Yang, Z.; Lee, Y.; Ferrari, M.; Mao, Z.-W.; Shen, H.; Wu, X.; Wolfram, J. Porous Silicon Microparticles for Delivery of SiRNA Therapeutics. *J. Vis. Exp.* **2015**, No. 95, 1–9. https://doi.org/10.3791/52075.

(7) Shen, J.; Xu, R.; Mai, J.; Kim, H. C.; Guo, X.; Qin, G.; Yang, Y.; Wolfram, J.; Mu, C.; Xia, X.; et al. High Capacity Nanoporous Silicon Carrier for Systemic Delivery of Gene Silencing Therapeutics. *ACS Nano* **2013**, *7* (11), 9867–9880. https://doi.org/10.1021/nn4035316.

(8) Lai, E.; Lepeleire, I. De; Liu, F.; Hecken, A. Van; Depre, M.; Hilliard, D.; Greenberg, H.; Metters, K. Safety of a Prostaglandin D 2 Receptor Antagonist. **2008**, *83* (6), 761–769. https://doi.org/10.1038/sj.clp.

(9) Cattaneo, A. G.; Gornati, R.; Sabbioni, E.; Chiriva-Internati, M.; Cobos, E.; Jenkins, M. R.; Bernardini, G. Nanotechnology and Human Health: Risks and Benefits. *J. Appl. Toxicol.* **2010**, *30* (8), 730–744. https://doi.org/10.1002/jat.1609.

(10) Nichols, J. W.; Bae, Y. H. EPR: Evidence and Fallacy. *J. Control. Release* **2014**, *190*,

451–464. https://doi.org/10.1016/j.jconrel.2014.03.057.

(11) Zhao, G.; Xu, M.; Zhao, M.; Dai, X.; Kong, W.; Gerald, M.; Guan, Y.; Wang, C.; Wang, X.; Comprehensive, J.; et al. Safety of Nanoparticles in Medicine. **2013**, *82* (1), 34–44. https://doi.org/10.1038/ki.2012.40.Activation.

(12) Tadic, M.; Kralj, S.; Jagodic, M.; Hanzel, D.; Makovec, D. Magnetic Properties of Novel Superparamagnetic Iron Oxide Nanoclusters and Their Peculiarity under Annealing Treatment. *Appl. Surf. Sci.* **2014**, *322*, 255–264. https://doi.org/10.1016/j.apsusc.2014.09.181.

(13) Maher, B. A.; Ahmed, I. A. M.; Karloukovski, V.; MacLaren, D. A.; Foulds, P. G.; Allsop, D.; Mann, D. M. A.; Torres-Jardón, R.; Calderon-Garciduenas, L. Magnetite Pollution Nanoparticles in the Human Brain. *Proc. Natl. Acad. Sci.* **2016**, *113* (39), 10797–10801. https://doi.org/10.1073/pnas.1605941113.

(14) Shokrollahi, H. A Review of the Magnetic Properties, Synthesis Methods and Applications of Maghemite. *J. Magn. Magn. Mater.* **2017**, *426* (November 2016), 74–81. https://doi.org/10.1016/j.jmmm.2016.11.033.

(15) Mout, R.; Moyano, D. F.; Rana, S.; Rotello, V. M. Surface Functionalization of Nanoparticles for Nanomedicine. *Chem. Soc. Rev.* **2012**, *41* (7), 2539. https://doi.org/10.1039/c2cs15294k.

(16) Fosgerau, K.; Hoffmann, T. Peptide Therapeutics: Current Status and Future Directions. *Drug Discov. Today* **2015**, *20* (1), 122–128. https://doi.org/10.1016/j.drudis.2014.10.003.

(17) Sharfstein, S. T. ScienceDirect Non-Protein Biologic Therapeutics. *Curr. Opin. Biotechnol.* **2017**, *53*. https://doi.org/10.1016/j.copbio.2017.12.014.

(18) Frankel, A. D.; Pabo, C. O. Cellular Uptake of the Tat Protein from Human Immunodeficiency Virus. *Cell* **1988**, *55* (6), 1189–1193. https://doi.org/10.1016/0092-8674(88)90263-2.

(19) Joliot, A.; Pernelle, C.; Deagostini-Bazin, H.; Prochiantz, A. Antennapedia Homeobox Peptide Regulates Neural Morphogenesis. *Proc. Natl. Acad. Sci.* **1991**, *88* (5), 1864–1868. https://doi.org/10.1073/pnas.88.5.1864.

(20) Derossi, D.; Joliot, A. H.; Chassaing, G.; Prochiantz, A. The Third Helix of the Antennapedia Homeodomain Translocates through Biological Membranes. *J. Biol. Chem.* **1994**, *269* (14), 10444–10450. https://doi.org/10444-50.

(21) Guidotti, G.; Brambilla, L.; Rossi, D. Cell-Penetrating Peptides: From Basic Research

to Clinics. *Trends Pharmacol. Sci.* **2017**, *38* (4), 406–424. https://doi.org/10.1016/j.tips.2017.01.003.

(22) Takechi, Y.; Tanaka, H.; Kitayama, H.; Yoshii, H.; Tanaka, M.; Saito, H. Comparative Study on the Interaction of Cell-Penetrating Polycationic Polymers with Lipid Membranes. *Chem. Phys. Lipids* **2012**, *165* (1), 51–58. https://doi.org/10.1016/j.chemphyslip.2011.11.002.

(23) Milletti, F. Cell-Penetrating Peptides: Classes, Origin, and Current Landscape. *Drug Discov. Today* **2012**, *17* (15–16), 850–860. https://doi.org/10.1016/j.drudis.2012.03.002.

(24) Zaro, J. L.; Vekich, J. E.; Tran, T.; Shen, W. C. Nuclear Localization of Cell-Penetrating Peptides Is Dependent on Endocytosis Rather than Cytosolic Delivery in CHO Cells. *Mol. Pharm.* **2009**, *6* (2), 337–344. https://doi.org/10.1021/mp800239p.

(25) Schiffer, M.; Edmundson, A. B. Use of Helical Wheels to Represent the Structures of Proteins and to Identify Segments with Helical Potential. **1964**.

(26) Scheller, A.; Oehlke, J.; Wiesner, B.; Dathe, M.; Krause, E.; Beyermann, M.; Melzig, M.; Bienert, M. Structural Requirements for Cellular Uptake of a -Helical. **1999**, *194*, 185–194.

(27) Oehlke, J.; Krause, E.; Wiesner, B.; Beyermann, M.; Bienert, M. Extensive Cellular Uptake into Endothelial Cells of an Amphipathic SS-Sheet Forming Peptide. *FEBS Lett.* **1997**, *415* (2), 196–199. https://doi.org/10.1016/S0014-5793(97)01123-X.

(28) Marks, J. R.; Placone, J.; Hristova, K.; Wimley, W. C. Spontaneous Membrane-Translocating Peptides by Orthogonal High-Throughput Screening. **2011**, 8995–9004. https://doi.org/10.1021/ja2017416.

(29) Conner, S. D.; Schmid, S. L. Regulated Portals of Entry into the Cell. *Nature* **2003**, *422* (6927), 37–44. https://doi.org/10.1038/nature01451.

(30) Eitzen, G. Actin Remodeling to Facilitate Membrane Fusion. *Biochim. Biophys. Acta - Mol. Cell Res.* **2003**, *1641* (2–3), 175–181. https://doi.org/10.1016/S0167-4889(03)00087-9.

(31) Nakase, I.; Tadokoro, A.; Kawabata, N.; Takeuchi, T.; Katoh, H.; Hiramoto, K.; Negishi, M.; Nomizu, M.; Sugiura, Y.; Futaki, S. Interaction of Arginine-Rich Peptides with Membrane-Associated Proteoglycans Is Crucial for Induction of Actin Organization and Macropinocytosis. *Biochemistry* **2007**, *46* (2), 492–501. https://doi.org/10.1021/bi0612824.

(32) Richard, J. P.; Melikov, K.; Brooks, H.; Prevot, P.; Lebleu, B.; Chernomordik, L. V. Cellular Uptake of Unconjugated TAT Peptide Involves Clathrin-Dependent Endocytosis and Heparan Sulfate Receptors. *J. Biol. Chem.* **2005**, *280* (15), 15300–15306. https://doi.org/10.1074/jbc.M401604200.

(33) Ferrari, A.; Pellegrini, V.; Arcangeli, C.; Fittipaldi, A.; Giacca, M.; Beltram, F. Caveolae-Mediated Internalization of Extracellular HIV-1 Tat Fusion Proteins Visualized in Real Time. *Mol. Ther.* **2003**, *8* (2), 284–294. https://doi.org/10.1016/S1525-0016(03)00122-9.

(34) Jiao, C. Y.; Delaroche, D.; Burlina, F.; Alves, I. D.; Chassaing, G.; Sagan, S. Translocation and Endocytosis for Cell-Penetrating Peptide Internalization. *J. Biol. Chem.* **2009**, *284* (49), 33957–33965. https://doi.org/10.1074/jbc.M109.056309.

(35) Marsh, M. Endocytosis. Oxford University Press: Oxford [England] ; New York 2001.

(36) Vercauteren, D.; Vandenbroucke, R. E.; Jones, A. T.; Rejman, J.; Demeester, J.; De Smedt, S. C.; Sanders, N. N.; Braeckmans, K. The Use of Inhibitors to Study Endocytic Pathways of Gene Carriers: Optimization and Pitfalls. *Mol. Ther.* **2010**, *18* (3), 561–569. https://doi.org/10.1038/mt.2009.281.

(37) Nakase, I.; Niwa, M.; Takeuchi, T.; Sonomura, K.; Kawabata, N.; Koike, Y.; Takehashi, M.; Tanaka, S.; Ueda, K.; Simpson, J. C.; et al. Cellular Uptake of Arginine-Rich Peptides: Roles for Macropinocytosis and Actin Rearrangement. *Mol. Ther.* **2004**, *10* (6), 1011–1022. https://doi.org/10.1016/j.ymthe.2004.08.010.

(38) Kaplan, I. M.; Wadia, J. S.; Dowdy, S. F. Cationic TAT Peptide Transduction Domain Enters Cells by Macropinocytosis. *J. Control. Release* **2005**, *102* (1), 247–253. https://doi.org/10.1016/j.jconrel.2004.10.018.

(39) Wadia, J. S.; Stan, R. V.; Dowdy, S. F. Transducible TAT-HA Fusogenic Peptide Enhances Escape of TAT-Fusion Proteins after Lipid Raft Macropinocytosis. *Nat. Med.* **2004**, *10* (3), 310–315. https://doi.org/10.1038/nm996.

(40) Säälik, P.; Elmquist, A.; Hansen, M.; Padari, K.; Saar, K.; Viht, K.; Langel, Ü.; Pooga, M. Protein Cargo Delivery Properties of Cell-Penetrating Peptides. A Comparative Study. *Bioconjug. Chem.* **2004**, *15* (6), 1246–1253. https://doi.org/10.1021/bc049938y.

(41) Islam, Z.; Sharmin, S.; Yamazaki, M. Elementary Processes for the Entry of Cell-Penetrating Peptides into Lipid Bilayer Vesicles and Bacterial Cells. **2018**, 3879–3892.

(42) Derossi, D.; Calvet, S.; Trembleau, A.; Brunissen, A.; Chassaing, G.; Prochiantz, A. Cell Internalization of the Third Helix of the Antennapedia Homeodomain Is Receptor-Independent. *J. Biol. Chem.* **1996**, *271* (30), 18188–18193.

https://doi.org/10.1074/jbc.271.30.18188.

(43) Alves, I. D.; Goasdoué, N.; Correia, I.; Aubry, S.; Galanth, C.; Sagan, S.; Lavielle, S.; Chassaing, G. Membrane Interaction and Perturbation Mechanisms Induced by Two Cationic Cell Penetrating Peptides with Distinct Charge Distribution. *Biochim. Biophys. Acta - Gen. Subj.* **2008**, *1780* (7–8), 948–959. https://doi.org/10.1016/j.bbagen.2008.04.004.

(44) Kawamoto, S.; Takasu, M.; Miyakawa, T.; Morikawa, R.; Oda, T.; Futaki, S.; Nagao, H. Inverted Micelle Formation of Cell-Penetrating Peptide Studied by Coarse-Grained Simulation: Importance of Attractive Force between Cell-Penetrating Peptides and Lipid Head Group. *J. Chem. Phys.* **2011**, *134* (9). https://doi.org/10.1063/1.3555531.

(45) Herce, H. D.; Garcia, A. E. Molecular Dynamics Simulations Suggest a Mechanism for Translocation of the HIV-1 TAT Peptide across Lipid Membranes. *Proc. Natl. Acad. Sci.* **2007**, *104* (52), 20805–20810. https://doi.org/10.1073/pnas.0706574105.

(46) Herce, H. D.; Garcia, A. E.; Litt, J.; Kane, R. S.; Martin, P.; Enrique, N.; Rebolledo, A.; Milesi, V. Arginine-Rich Peptides Destabilize the Plasma Membrane, Consistent with a Pore Formation Translocation Mechanism of Cell-Penetrating Peptides. *Biophys. J.* **2009**, *97* (7), 1917–1925. https://doi.org/10.1016/j.bpj.2009.05.066.

(47) Wender, P. A.; Galliher, W. C.; Goun, E. A.; Jones, L. R.; Pillow, T. H. The Design of Guanidinium-Rich Transporters and Their Internalization Mechanisms. *Adv. Drug Deliv. Rev.* **2008**, *60* (4–5), 452–472. https://doi.org/10.1016/j.addr.2007.10.016.

(48) Fischer, P. M. Cellular Uptake Mechanisms and Potential Therapeutic Utility of Peptidic Cell Delivery Vectors: Progress 2001-2006. *Med. Res. Rev.* **2007**, *27* (6), 755–795. https://doi.org/10.1002/med.20093.

(49) Rujitanaroj, P.; Jao, B.; Yang, J.; Wang, F.; Anderson, J. M.; Wang, J.; Chew, S. Y. Controlling Fibrous Capsule Formation through Long-Term down-Regulation of Collagen Type I (COL1A1) Expression by Nanofiber-Mediated SiRNA Gene Silencing. *Acta Biomater.* **2013**, *9* (1), 4513–4524. https://doi.org/10.1016/j.actbio.2012.09.029.

(50) McMaster, G. K.; Crombez, L.; Brasseur, R.; Heitz, F.; Aldrian-Herrada, G.; Nguyen, Q. N.; Konate, K.; Divita, G. A New Potent Secondary Amphipathic Cell–penetrating Peptide for SiRNA Delivery Into Mammalian Cells. *Mol. Ther.* **2008**, *17* (1), 95–103. https://doi.org/10.1038/mt.2008.215.

(51) Pae, J.; Säälik, P.; Liivamägi, L.; Lubenets, D.; Arukuusk, P.; Langel, Ü.; Pooga, M. Translocation of Cell-Penetrating Peptides across the Plasma Membrane Is Controlled by Cholesterol and Microenvironment Created by Membranous Proteins. *J. Control.*

Release **2014**, *192*, 103–113. https://doi.org/10.1016/j.jconrel.2014.07.002.

(52) Drin, G.; Démé, H.; Temsamani, J.; Brasseur, R. Translocation of the PAntp Peptide and Its Amphipathic Analogue AP-2AL. *Biochemistry* **2001**, *40* (6), 1824–1834. https://doi.org/10.1021/bi002019k.

(53) Morris, M. C.; Depollier, J.; Mery, J.; Heitz, F.; Divita, G. A Peptide Carrier for the Delivery of Biologically Active Proteins into Mammalian Cells. *Nat. Biotechnol.* **2001**, *19*, 1173.

(54) Song, J.; Zhang, Y.; Zhang, W.; Chen, J.; Yang, X.; Ma, P.; Zhang, B.; Liu, B.; Ni, J.; Wang, R. Cell Penetrating Peptide TAT Can Kill Cancer Cells via Membrane Disruption after Attachment of Camptothecin. *Peptides* **2015**, *63*, 143–149. https://doi.org/10.1016/j.peptides.2014.12.001.

(55) Essmann, U.; Perera, L.; Berkowitz, M. L.; Darden, T.; Lee, H.; Pedersen, L. G. A Smooth Particle Mesh Ewald Method. *J. Chem. Phys.* **1995**, *103* (19), 8577–8593. https://doi.org/10.1063/1.470117.

(56) Zheng, J.; Balasundaram, R.; Gehrke, S. H.; Heffelfinger, G. S.; Goddard, W. A.; Jiang, S. Cell Multipole Method for Molecular Simulations in Bulk and Confined Systems. *J. Chem. Phys.* **2003**, *118* (12), 5347–5355. https://doi.org/10.1063/1.1553979.

(57) Leach AR. *Molecular Modelling: Principles and Applications*; 2001.

(58) Ramachandran, K. I.; Deepa, G.; Namboori, K. *Computational Chemistry and Molecular Modeling: Principles and Applications*; Springer Verlag, 2008.

(59) Bernardi, R. C.; Melo, M. C. R.; Schulten, K. Enhanced Sampling Techniques in Molecular Dynamics Simulations of Biological Systems. *Biochim. Biophys. Acta - Gen. Subj.* **2015**, *1850* (5), 872–877. https://doi.org/10.1016/j.bbagen.2014.10.019.

(60) Barducci, A.; Bonomi, M.; Parrinello, M. Metadynamics. *Wiley Interdiscip. Rev. Comput. Mol. Sci.* **2011**, *1* (5), 826–843. https://doi.org/10.1002/wcms.31.

(61) Barducci, A.; Bussi, G.; Parrinello, M. Well-Tempered Metadynamics: A Smoothly Converging and Tunable Free-Energy Method. *Phys. Rev. Lett.* **2008**, *100* (2), 1–4. https://doi.org/10.1103/PhysRevLett.100.020603.

(62) Tiwary, P.; Parrinello, M. A Time-Independent Free Energy Estimator for Metadynamics. *J. Phys. Chem. B* **2015**, *119* (3), 736–742. https://doi.org/10.1021/jp504920s.

(63) Rudnick, R. L.; Gao, S. Composition of the Continental Crust. In *Treatise on*

Geochemistry; Elsevier, 2003; Vol. 637–638, pp 1–64. https://doi.org/10.1016/B0-08-043751-6/03016-4.

(64) Halas, N. J. Nanoscience under Glass: The Versatile Chemistry of Silica Nanostructures. *ACS Nano* **2008**, *2* (2), 179–183. https://doi.org/10.1021/nn800052e.

(65) Algar, W. R.; Blanco-Canosa, J. B.; Manthe, R. L.; Susumu, K.; Stewart, M. H.; Dawson, P. E.; Medintz, I. L. Nanomaterial Interfaces in Biology. *Methods Mol. Biol.* **2013**, *1025*, 47–73. https://doi.org/10.1007/978-1-62703-462-3.

(66) Guerrero-Martínez, A.; Pérez-Juste, J.; Liz-Marzán, L. M. Recent Progress on Silica Coating of Nanoparticles and Related Nanomaterials. *Adv. Mater.* **2010**, *22* (11), 1182–1195. https://doi.org/10.1002/adma.200901263.

(67) Liu, Y.; Zhang, X.; Zhou, M.; Chen, X.; Zhang, X. Surface Engineering of Organic Nanoparticles for Highly Improved Bioimaging. *Colloids Surfaces B Biointerfaces* **2017**, *159*, 596–604. https://doi.org/10.1016/j.colsurfb.2017.07.077.

(68) Atkins, D.; Kekicheff, P.; Spalla, O. Adhesion between Colloidal Silica as Seen with Direct Force Measurement. *J. Colloid Interface Sci.* **1997**, *188* (1), 234–237. https://doi.org/10.1006/jcis.1996.4751.

(69) Papirer, E. *Adsorption on Silica Surfaces*; CRC Press: Cambridge, 2000. https://doi.org/10.1201/9781482269703.

(70) Parida, S. K.; Dash, S.; Patel, S.; Mishra, B. K. Adsorption of Organic Molecules on Silica Surface. *Adv. Colloid Interface Sci.* **2006**, *121* (1–3), 77–110. https://doi.org/10.1016/j.cis.2006.05.028.

(71) Feng, J.; Pandey, R. B.; Berry, R. J.; Farmer, B. L.; Naik, R. R.; Heinz, H. Adsorption Mechanism of Single Amino Acid and Surfactant Molecules to Au {111} Surfaces in Aqueous Solution: Design Rules for Metal-Binding Molecules. *Soft Matter* **2011**, *7* (5), 2113–2120. https://doi.org/10.1039/c0sm01118e.

(72) Heinz, H. The Role of Chemistry and PH of Solid Surfaces for Specific Adsorption of Biomolecules in Solution - Accurate Computational Models and Experiment. *J. Phys. Condens. Matter* **2014**, *26* (24). https://doi.org/10.1088/0953-8984/26/24/244105.

(73) Raut, V. P.; Agashe, M. A.; Stuart, S. J.; Latour, R. A. Molecular Dynamics Simulations of Peptide−Surface Interactions. *Langmuir* **2005**, *21* (4), 1629–1639. https://doi.org/10.1021/la047807f.

(74) Patwardhan, S. V.; Emami, F. S.; Berry, R. J.; Jones, S. E.; Naik, R. R.; Deschaume, O.; Heinz, H.; Perry, C. C. Chemistry of Aqueous Silica Nanoparticle Surfaces and the

Mechanism of Selective Peptide Adsorption. *J. Am. Chem. Soc.* **2012**, *134* (14), 6244–6256. https://doi.org/10.1021/ja211307u.

(75) Kubiak-Ossowska, K.; Burley, G.; Patwardhan, S. V.; Mulheran, P. A. Spontaneous Membrane-Translocating Peptide Adsorption at Silica Surfaces: A Molecular Dynamics Study. *J. Phys. Chem. B* **2013**, *117* (47), 14666–14675. https://doi.org/10.1021/jp409130s.

(76) Sprenger, K. G.; Pfaendtner, J. Strong Electrostatic Interactions Lead to Entropically Favorable Binding of Peptides to Charged Surfaces. *Langmuir* **2016**, *32* (22), 5690–5701. https://doi.org/10.1021/acs.langmuir.6b01296.

(77) Prakash, A.; Sprenger, K. G.; Pfaendtner, J. Essential Slow Degrees of Freedom in Protein-Surface Simulations: A Metadynamics Investigation. *Biochem. Biophys. Res. Commun.* **2018**, *498* (2), 274–281. https://doi.org/10.1016/j.bbrc.2017.07.066.

(78) Grasso, G.; Deriu, M. A.; Prat, M.; Rimondini, L.; Vernè, E.; Follenzi, A.; Danani, A. Cell Penetrating Peptide Adsorption on Magnetite and Silica Surfaces: A Computational Investigation. *J. Phys. Chem. B* **2015**, *119* (26), 8239–8246. https://doi.org/10.1021/jp512782e.

(79) Emami, F. S.; Puddu, V.; Berry, R. J.; Varshney, V.; Patwardhan, S. V.; Perry, C. C.; Heinz, H. Erratum: Force Field and a Surface Model Database for Silica to Simulate Interfacial Properties in Atomic Resolution (Chemistry of Materials (2014) 26:8 (2647-2658) DOI: 10.1021/Cm500365c). *Chem. Mater.* **2016**, *28* (1), 406–407. https://doi.org/10.1021/acs.chemmater.5b04760.

(80) Liang, M. K.; Deschaume, O.; Patwardhan, S. V.; Perry, C. C. Direct Evidence of ZnO Morphology Modification via the Selective Adsorption of ZnO-Binding Peptides. *J. Mater. Chem.* **2011**, *21* (1), 80–89. https://doi.org/10.1039/c0jm02124e.

(81) Heeribout, L.; Vincent, R.; Batamack, P.; Dor, C.; Fraissard, J. Brønsted Acidity of Amorphous Silica – Aluminas Studied by 1 H NMR. *Science (80-.).* **1998**, *53*, 23–31. https://doi.org/10.4028/www.scientific.net/AMM.71-78.1366.

(82) Helmy, A. K.; de Bussetti, S. G.; Ferreiro, E. A. The Water-Silicas Interfacial Interaction Energies. *Appl. Surf. Sci.* **2007**, *253* (16), 6878–6882. https://doi.org/10.1016/j.apsusc.2007.01.127.

(83) Méndez, A.; Bosch, E.; Rosés, M.; Neue, U. D. Comparison of the Acidity of Residual Silanol Groups in Several Liquid Chromatography Columns. *J. Chromatogr. A* **2003**, *986* (1), 33–44. https://doi.org/10.1016/S0021-9673(02)01899-X.

(84) Lindberg, M.; Biverståhl, H.; Gräslund, A.; Mäler, L. Structure and Positioning

Comparison of Two Variants of Penetratin in Two Different Membrane Mimicking Systems by NMR. *Eur. J. Biochem.* **2003**, *270* (14), 3055–3063. https://doi.org/10.1046/j.1432-1033.2003.03685.x.

(85) Shen, Y.; Maupetit, J.; Derreumaux, P.; Tufféry, P. Improved PEP-FOLD Approach for Peptide and Miniprotein Structure Prediction. *J. Chem. Theory Comput.* **2014**, *10* (10), 4745–4758. https://doi.org/10.1021/ct500592m.

(86) Huang, J.; Rauscher, S.; Nawrocki, G.; Ran, T.; Feig, M.; De Groot, B. L.; Grubmüller, H.; MacKerell, A. D. CHARMM36m: An Improved Force Field for Folded and Intrinsically Disordered Proteins. *Nat. Methods* **2016**, *14* (1), 71–73. https://doi.org/10.1038/nmeth.4067.

(87) Jorgensen, W. L.; Chandrasekhar, J.; Madura, J. D.; Impey, R. W.; Klein, M. L. Comparison of Simple Potential Functions for Simulating Liquid Water. *J. Chem. Phys.* **1983**, *79* (2), 926–935. https://doi.org/10.1063/1.445869.

(88) Fletcher, R.; Powell, M. J. D. A Rapidly Convergent Descent Method for Minimization. *Comput. J.* **1963**, *6* (2), 163–168. https://doi.org/10.1093/comjnl/6.2.163.

(89) Bussi, G.; Donadio, D.; Parrinello, M. Canonical Sampling through Velocity Rescaling. *J. Chem. Phys.* **2007**, *126* (1). https://doi.org/10.1063/1.2408420.

(90) Berendsen, H. J. C.; Postma, J. P. M.; Van Gunsteren, W. F.; Dinola, A.; Haak, J. R. Molecular Dynamics with Coupling to an External Bath. *J. Chem. Phys.* **1984**, *81* (8), 3684–3690. https://doi.org/10.1063/1.448118.

(91) Evans, D. J.; Holian, B. L. The Nose-Hoover Thermostat. *J. Chem. Phys.* **1985**, *83* (8), 4069–4074. https://doi.org/10.1063/1.449071.

(92) Parrinello, M.; Rahman, A. Polymorphic Transitions in Single Crystals: A New Molecular Dynamics Method. *J. Appl. Phys.* **1981**, *52* (12), 7182–7190. https://doi.org/10.1063/1.328693.

(93) Hess, B.; Bekker, H.; Berendsen, H. J. C.; Fraaije, J. G. E. M. LINCS: A Linear Constraint Solver for Molecular Simulations. *J. Comput. Chem.* **1997**, *18* (12), 1463–1472. https://doi.org/10.1002/(SICI)1096-987X(199709)18:12<1463::AID-JCC4>3.0.CO;2-H.

(94) Tribello, G. A.; Bonomi, M.; Branduardi, D.; Camilloni, C.; Bussi, G. PLUMED 2: New Feathers for an Old Bird. *Comput. Phys. Commun.* **2014**, *185* (2), 604–613. https://doi.org/10.1016/j.cpc.2013.09.018.

(95) Abraham, M. J.; Murtola, T.; Schulz, R.; Páll, S.; Smith, J. C.; Hess, B.; Lindah, E.

Gromacs: High Performance Molecular Simulations through Multi-Level Parallelism from Laptops to Supercomputers. *SoftwareX* **2015**, *1–2*, 19–25. https://doi.org/10.1016/j.softx.2015.06.001.

(96) Humphrey, W.; Dalke, A.; Schulten, K. VMD: Visual Molecular Dynamics. *J. Mol. Graph.* **1996**, *14* (1), 33–38. https://doi.org/10.1016/0263-7855(96)00018-5.

(97) Kabsch, W.; Sander, C. Dictionary of Protein Secondary Structure: Pattern Recognition of Hydrogen-Bonded and Geometrical Features. *Biopolymers* **1983**, *22* (12), 2577–2637. https://doi.org/10.1002/bip.360221211.

(98) Heinig, M.; Frishman, D. STRIDE: A Web Server for Secondary Structure Assignment from Known Atomic Coordinates of Proteins. *Nucleic Acids Res.* **2004**, *32* (WEB SERVER ISS.). https://doi.org/10.1093/nar/gkh429.

(99) Bussi, G.; Branduardi, D. Free-Energy Calculations with Metadynamics: Theory and Practice. **2015**, *28*, 1–49. https://doi.org/10.1002/9781118889886.ch1.

(100) Rimola, A.; Costa, D.; Sodupe, M.; Lambert, J.-F.; Ugliengo, P. Silica Surface Features and Their Role in the Adsorption of Biomolecules: Computational Modeling and Experiments. *Chem. Rev.* **2013**, *113* (6), 4216–4313. https://doi.org/10.1021/cr3003054.

(101) Tischenko, V. A.; Gun'ko, V. M.; Voronin, E. F.; Zarko, V. I.; Siltchenko, S. S.; Barvinchenko, V. N.; Chuiko, A. A.; Kazakova, O. A.; Dudnik, V. V.; Turov, V. V. Aqueous Suspensions of Fumed Silica and Adsorption of Proteins. *J. Colloid Interface Sci.* **2002**, *192* (1), 166–178. https://doi.org/10.1006/jcis.1997.4985.

(102) Wegmann, M.; Scharr, M. *Synthesis of Magnetic Iron Oxide Nanoparticles*; Elsevier Inc., 2018. https://doi.org/10.1016/B978-0-12-805364-5.00008-1.

(103) Hofmann, A.; Wenzel, D.; Becher, U. M.; Freitag, D. F.; Klein, A. M.; Eberbeck, D.; Schulte, M.; Zimmermann, K.; Bergemann, C.; Gleich, B.; et al. Combined Targeting of Lentiviral Vectors and Positioning of Transduced Cells by Magnetic Nanoparticles. *Proc. Natl. Acad. Sci.* **2009**, *106* (1), 44–49. https://doi.org/10.1073/pnas.0803746106.

(104) Huang, Y.-W.; Lee, H.-J.; Tolliver, L. M.; Aronstam, R. S. Delivery of Nucleic Acids and Nanomaterials By Cell-Penetrating Peptide: Opportunities and Challenges. *BioMed Reasearch Int.* **2014**, *2015*, 11–13. https://doi.org/10.1155/2015/834079.

(105) Hu, J. J.; Xiao, D.; Zhang, X. Z. Advances in Peptide Functionalization on Mesoporous Silica Nanoparticles for Controlled Drug Release. *Small* **2016**, *12* (25), 3344–3359. https://doi.org/10.1002/smll.201600325.

(106) Puddu, V.; Perry, C. C. Interactions at the Silica-Peptide Interface: The Influence of Particle Size and Surface Functionality. *Langmuir* **2014**, *30* (1), 227–233. https://doi.org/10.1021/la403242f.

(107) Kubiak-Ossowska, K.; Mulheran, P. A. What Governs Protein Adsorption and Immobilization at a Charged Solid Surface? *Langmuir* **2010**, *26* (11), 7690–7694. https://doi.org/10.1021/la101276v.

Supporting Information

In Figure SI 1 the three models of the chosen silica surfaces are shown.

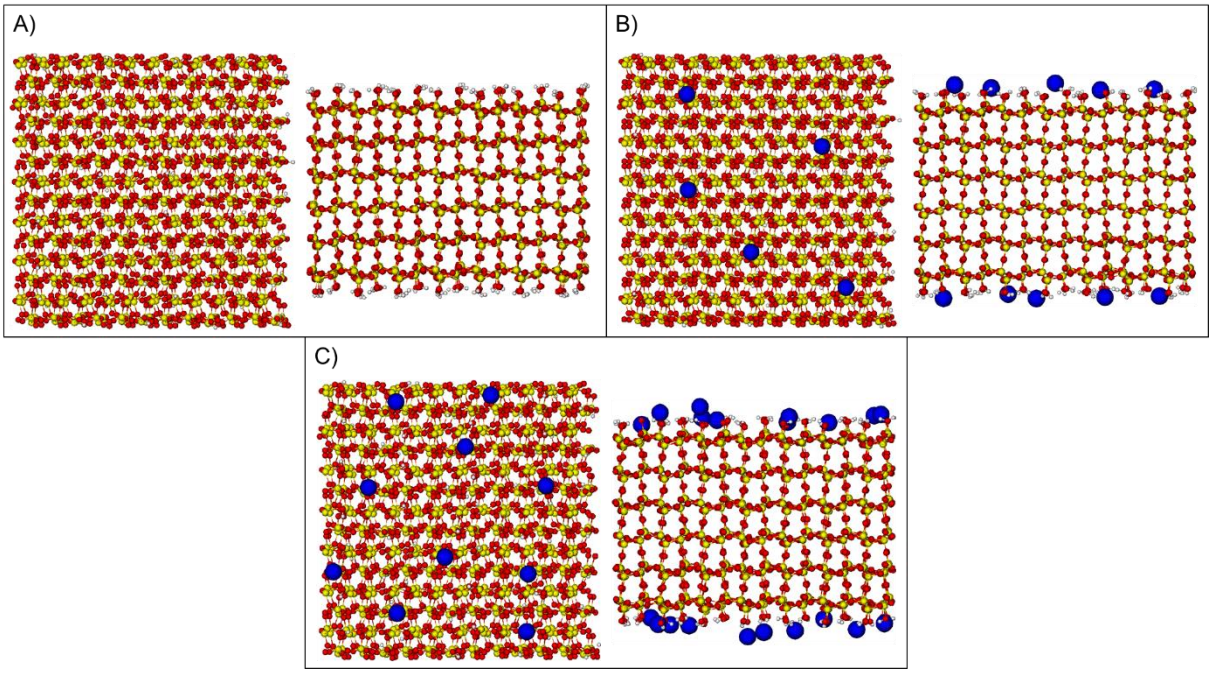

Figure SI 1 Silica surfaces models. A) SiOH: top view (left side); side view (right side); B) 9SiO(H,Na): top view (left side); side view (right side); C) 18SiO(H,Na): top view (left side); side view (right side). The Na ions are represented in blue, the Si atoms in yellow, the O atoms in red and the H atoms in white.

In Figure SI 2, Figure SI 3 & Figure SI 4 the time evolution of the distance between peptides-surfaces is represented.

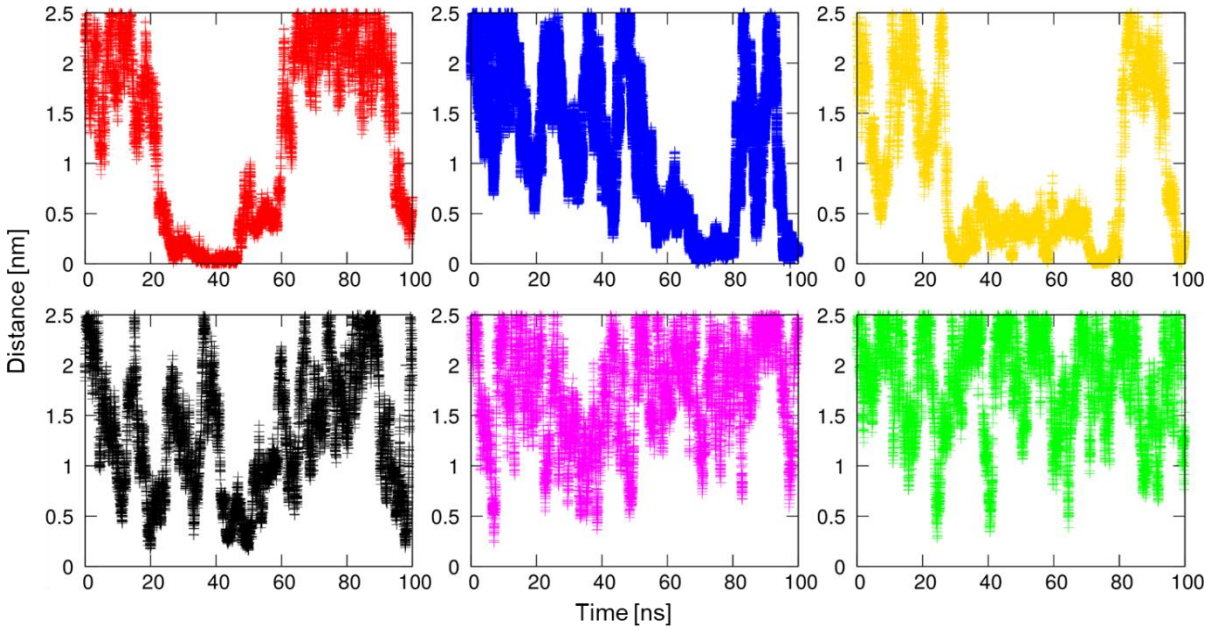

Figure SI 2 Distance between the COM of the peptides and the COM of SIOH surface. CADY peptide in red; Map peptide in blue; pAntp peptide in yellow; PEP peptide in black; (ARG)9 peptide in magenta; TAT peptide in green.

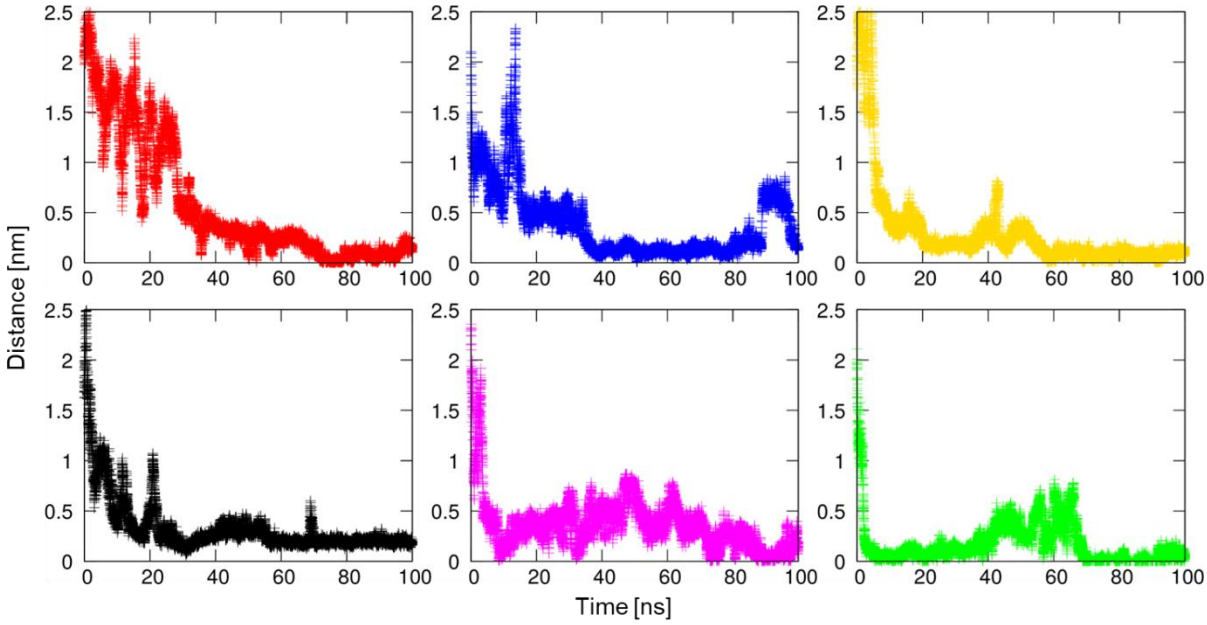

Figure SI 3 Distance between the COM of the peptides and the COM of 9SIO(H,Na) surface. CADY peptide in red; Map peptide in blue; pAntp peptide in yellow; PEP peptide in black; (ARG)9 peptide in magenta; TAT peptide in green.

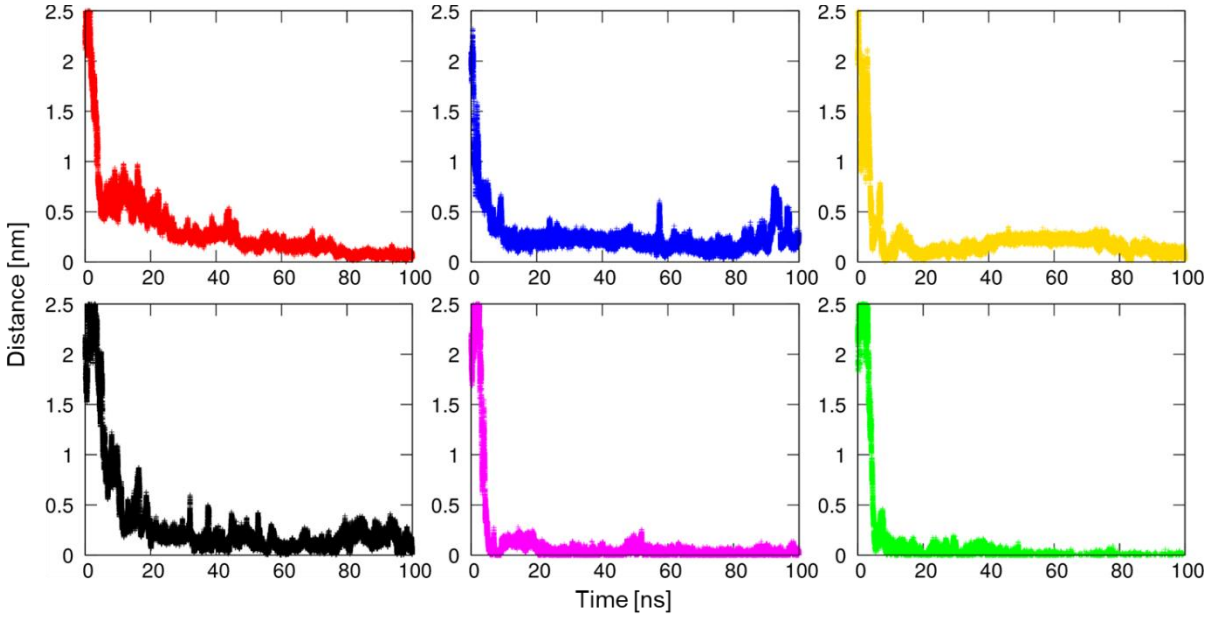

Figure SI 4 Distance between the COM of the peptides and the COM of 18SIO(H,Na) surface. CADY peptide in red; Map peptide in blue; pAntp peptide in yellow; PEP peptide in black; (ARG)9 peptide in magenta; TAT peptide in green.

In Figure SI 5, Figure SI 6 & Figure SI 7 the RMSD value of the C-alpha fitted on C-alpha for each system CPP-surface is shown. Each trend shows that the systems have reached a stable configuration.

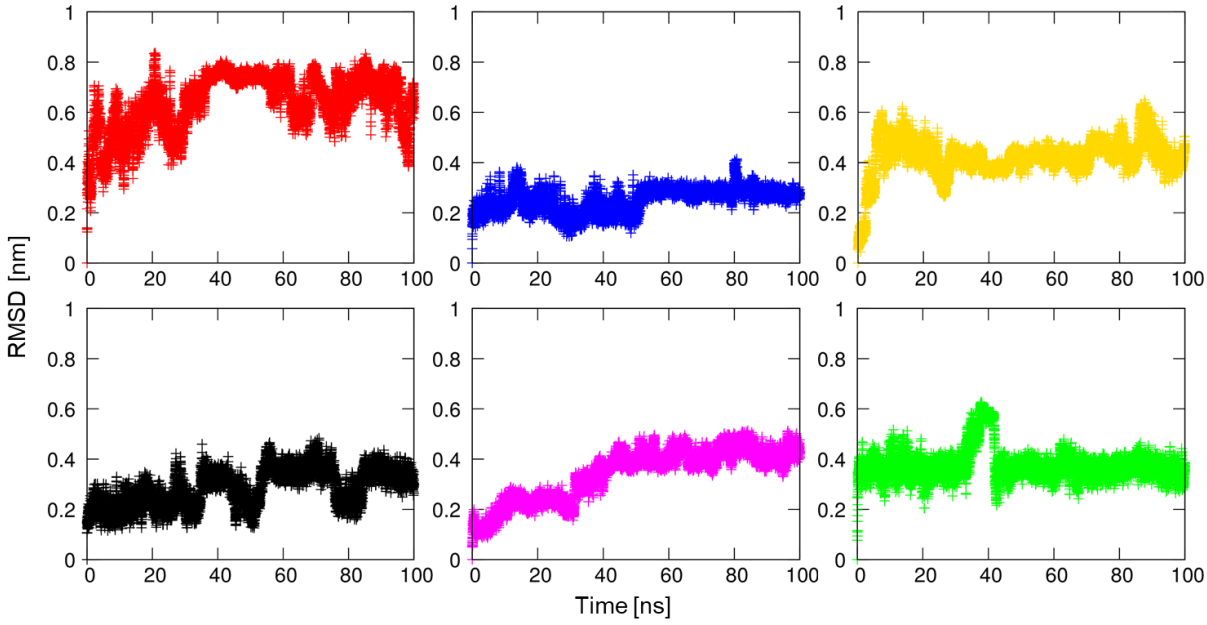

Figure SI 5 RMSD of the peptide interacting with the SiOH surface calculated on C-alpha fitted on C-alpha. CADY peptide (red); MAP peptide (blue); pAntp peptide (yellow); PEP peptide (black); (ARG)9 peptide (magenta); TAT peptide (green).

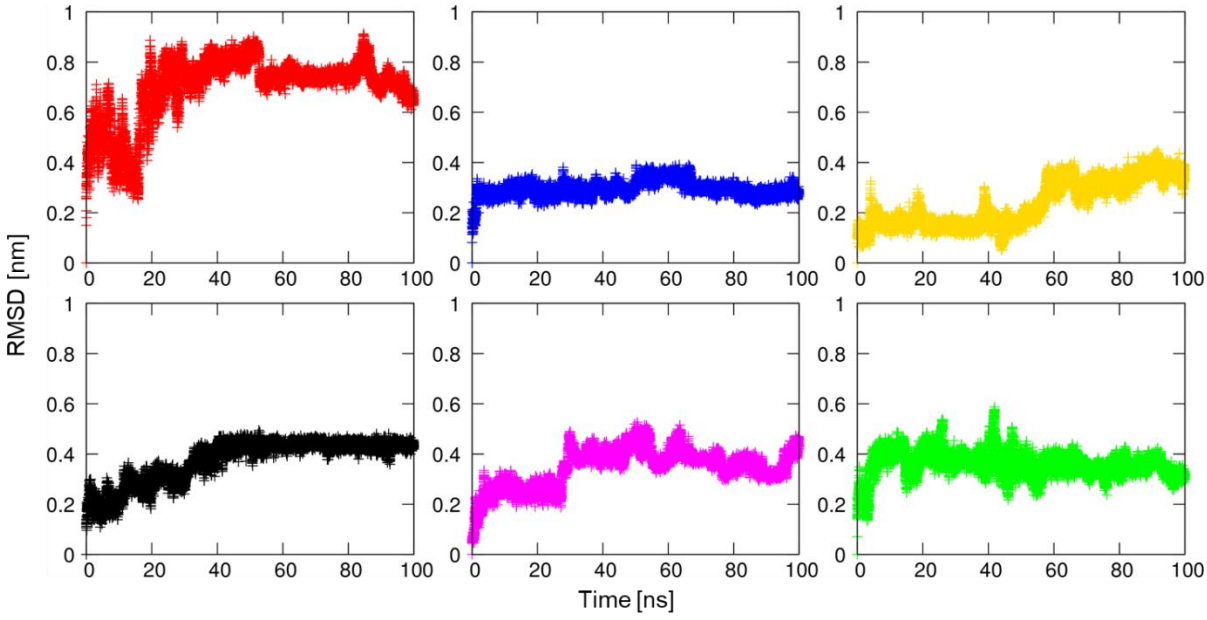

Figure SI 6 RMSD of the peptide interacting with the 9SiO(H,Na) surface calculated on C-alpha fitted on C-alpha. CADY peptide (red); MAP peptide (blue); pAntp peptide (yellow); PEP peptide (black); (ARG)9 peptide (magenta); TAT peptide (green).

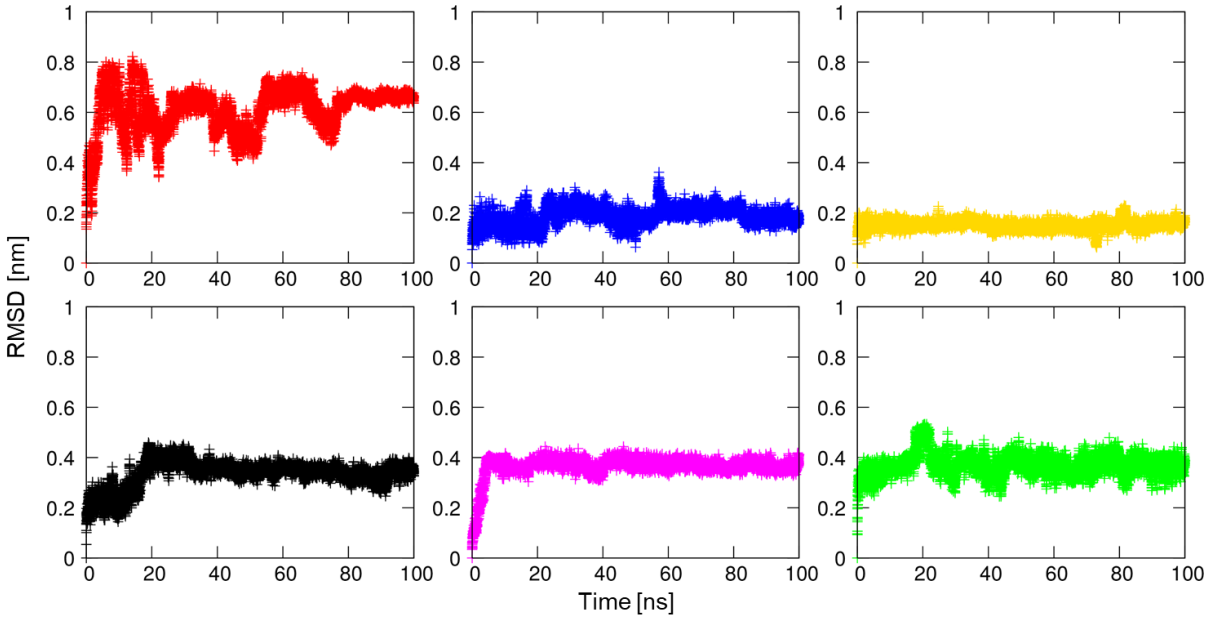

Figure SI 7 RMSD of the peptide interacting with the 18SiO(H,Na) surface calculated on C-alpha fitted on C-alpha. CADY peptide (red); MAP peptide (blue); pAntp peptide (yellow); PEP peptide (black); (ARG)9 peptide (magenta); TAT peptide (green).

In Figure SI 8, Figure SI 9 & Figure SI 10 are shown the total H-bond count per residue interacting with the surfaces, normalized by the maximum value of each CPP-surface system. The bars are divided per pattern, showing the donor (filled bar) and the acceptor rates (crossed bar). The total amount of the bar reflects the total H-bond capability of each residue.

H-bonds are determined based on cut-offs for the angle Hydrogen - Donor - Acceptor (zero is extended) and the distance Donor – Acceptor (0.35 nm). OH and NH groups are regarded as donors, O and N as acceptors.

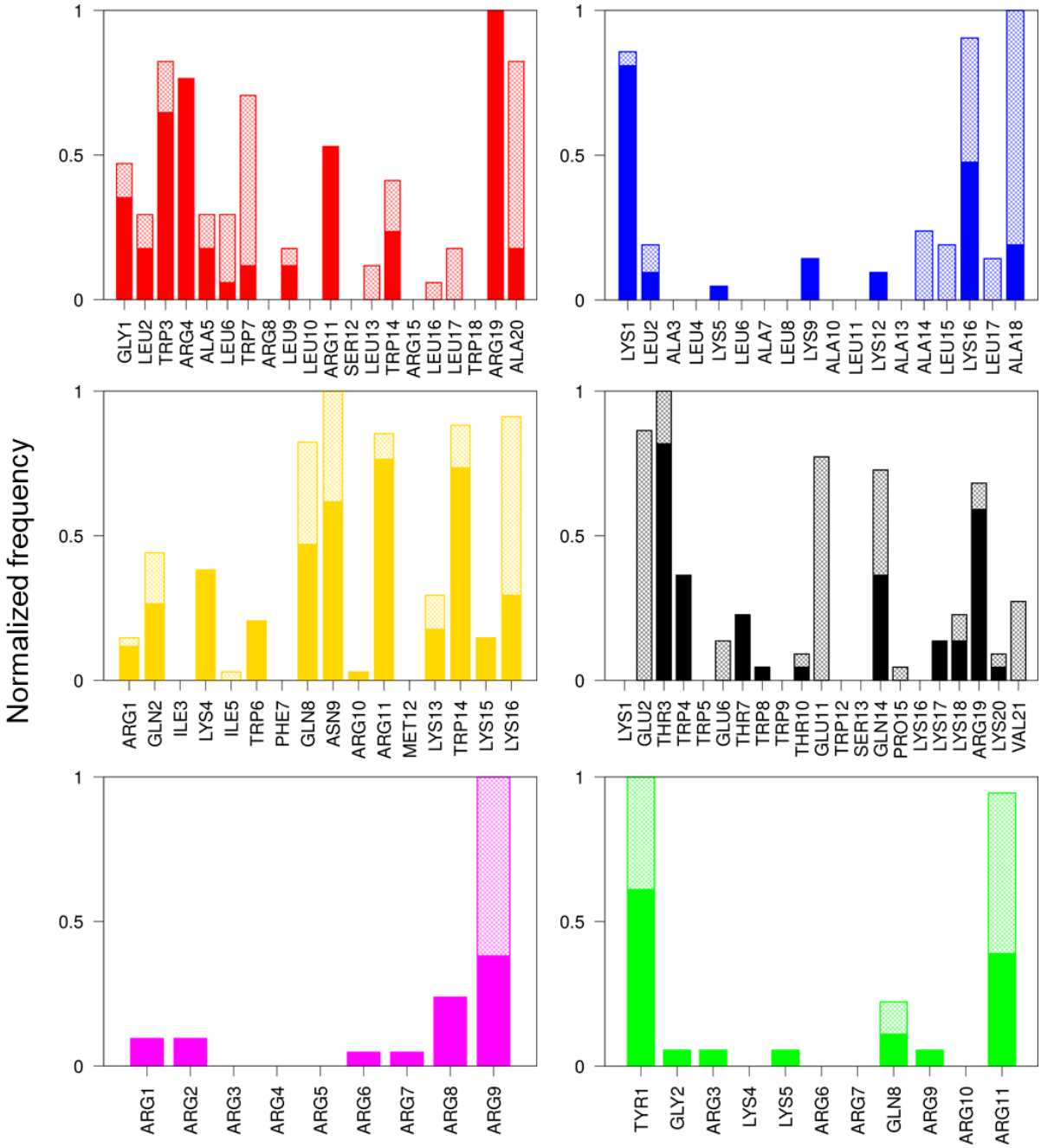

Figure SI 8 Residues forming H-bond with the SiOH surface: filled bar DONATOR, crossed bar ACEPTOR. CADY peptide (red); MAP peptide (blue); pAntp peptide (yellow); PEP peptide (black); (ARG)9 peptide (magenta); TAT peptide (green).

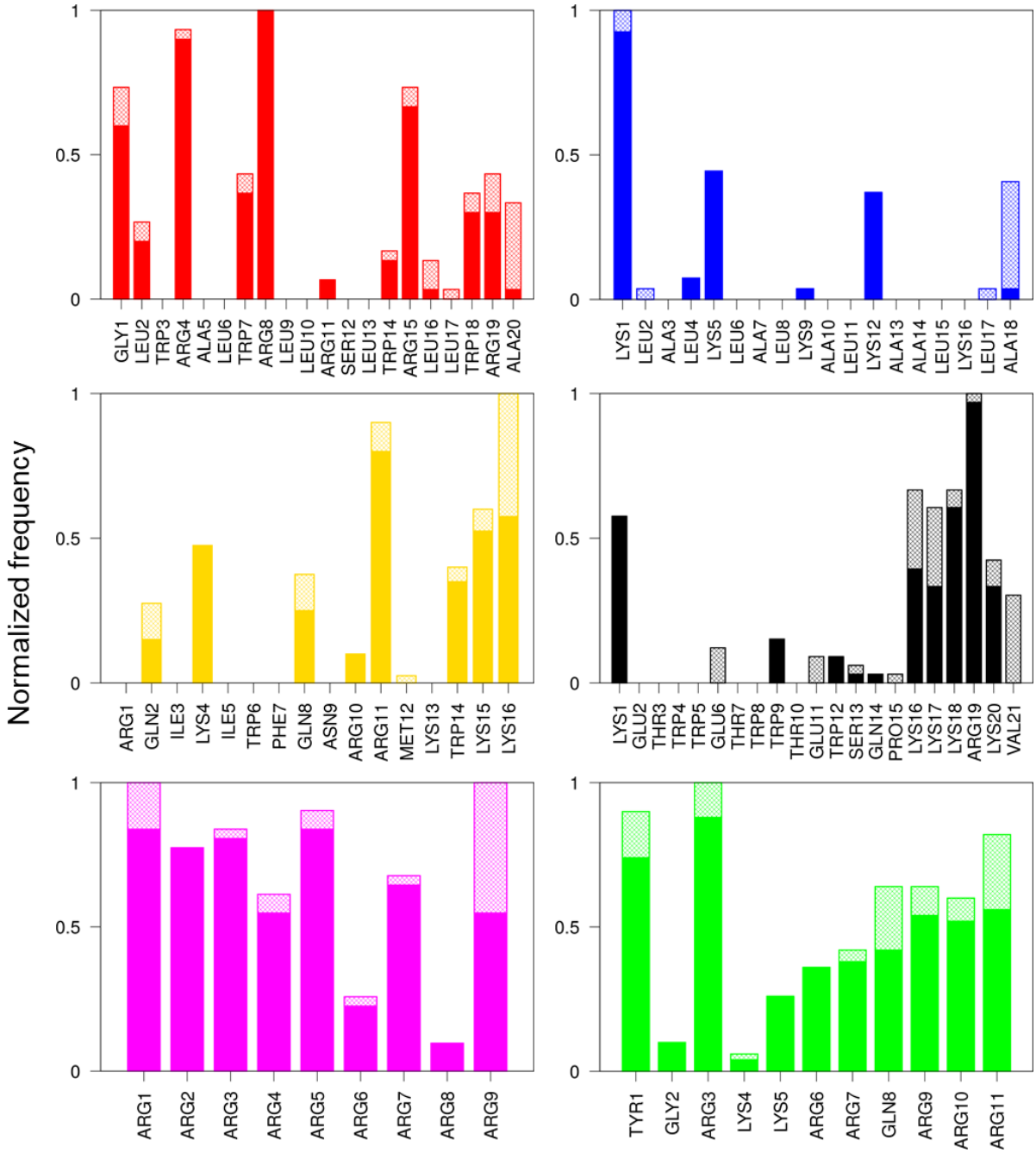

Figure SI 9 Residues forming H-bond with the 9SiO(H,Na) surface: filled bar DONATOR, crossed bar ACEPTOR. CADY peptide (red); MAP peptide (blue); pAntp peptide (yellow); PEP peptide (black); (ARG)9 peptide (magenta); TAT peptide (green).

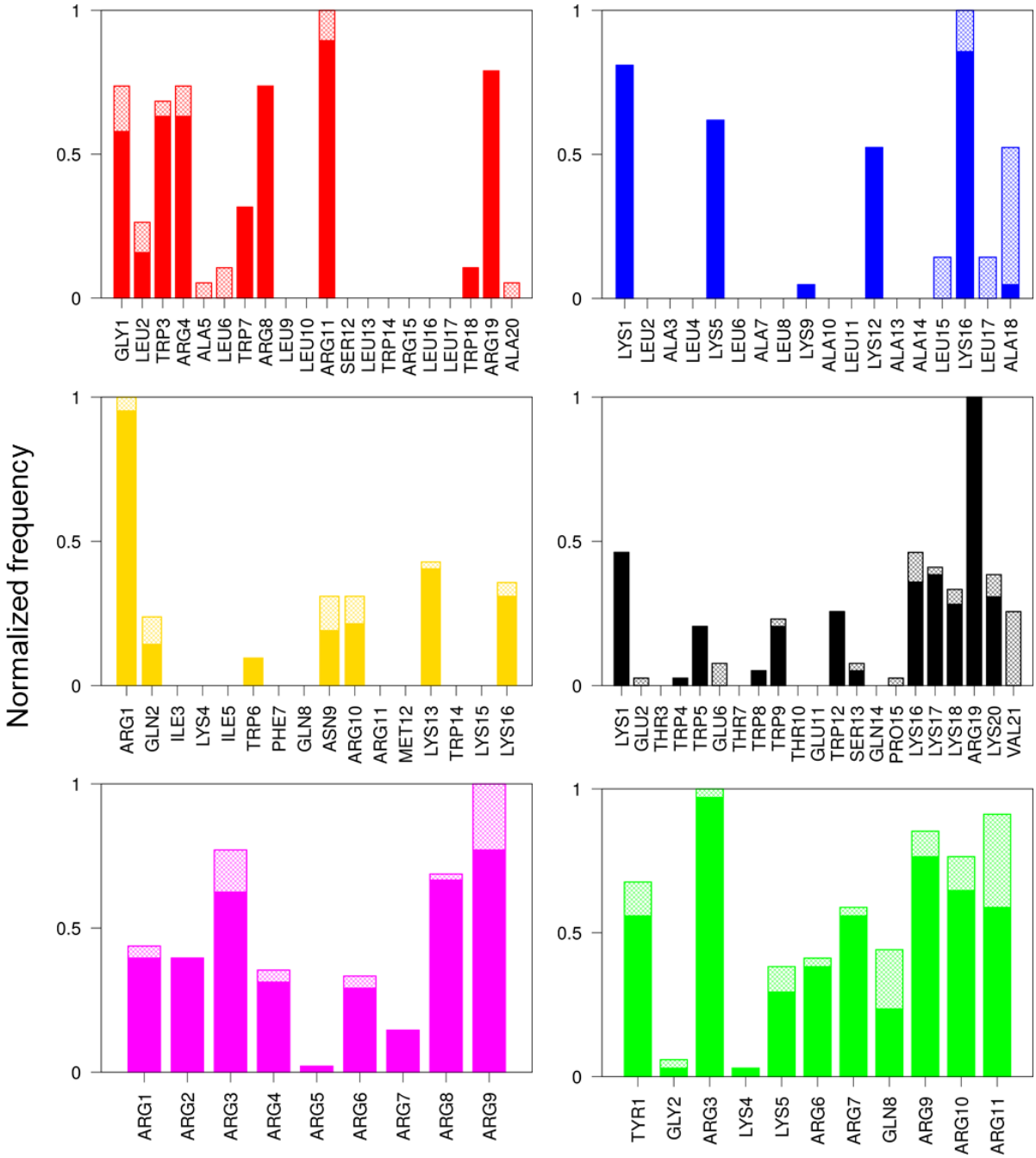

Figure SI 10 Residues forming H-bond with the 18SiO(H,Na) surface: filled bar DONATOR, crossed bar ACEPTOR. CADY peptide (red); MAP peptide (blue); pAntp peptide (yellow); PEP peptide (black); (ARG)9 peptide (magenta); TAT peptide (green).

In Figure SI 11 three snapshots of the systems MAP peptide – silica surface (SiOH surface Figure SI 11 A-C; 9SiO(H,Na) surface Figure SI 11 D-F; 18SiO(H,Na) surface Figure SI 11 G-I) are shown. In this case, the MAP peptide conserves its helical secondary structure in all the simulations.

The contact with the SiOH surface starts with the C-terminal tail in a vertical orientation (Figure SI 11 A); then the N-terminal tail approaches the surface (Figure SI 11 B) and in the end, it results interacting with the surface in a horizontal conformation (Figure SI 11 C).

On the other hand, the MAP peptide contacts the 9SiO(H,Na) surface with the N-terminal tail, in particular the LYS1 reaches the surfaces (Figure SI 11 D), the C-terminal tail reaches out for the surface (Figure SI 11 E) and in the last snapshot it is laid down onto the surface (Figure SI 11 F).

In the same manner, the MAP peptide contacts the 18SiO(H,Na) surface with the LYS1 (Figure SI 11 G) but the LYS in the C-terminal tail and in the core structure engage with the surface (Figure SI 11 H) resulting in stronger interaction (Figure SI 11 I).

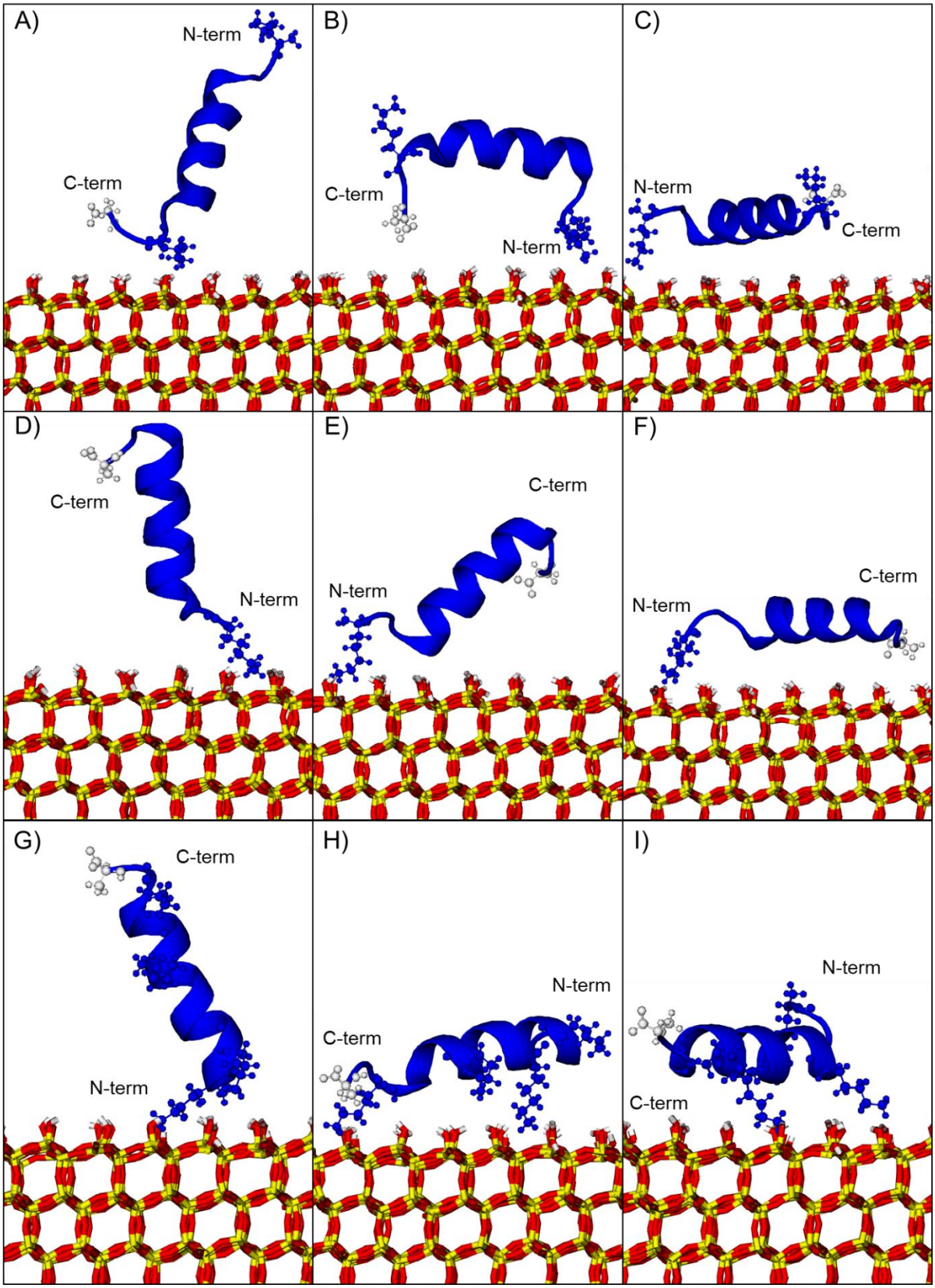

Figure SI 11 Snapshots of the contacts between the MAP peptide with the SiOH (A,B,C), the 9SiO(H,Na) (D,E,F) and the 18SiO(H,Na) (G,H,I) surfaces: A,D,G) Initial contact; B,E,H) during contact; C,F,I) final configuration. The residues from Table 3.4 are highlighted: non-polar residues in white (ALA); basic residues in blue (LYS). The N-term and the C-term are highlighted.

In Figure SI 12 are shown three snapshots of the systems pAntp peptide – silica surface (SiOH surface Figure SI 12 A-C; 9SiO(H,Na) surface Figure SI 12 D-F; 18SiO(H,Na) surface Figure SI 12 G-I).

In the pAntp-SiOH surface simulation, the peptide is more unfolded then in the other simulations. The interaction starts with the C-terminal residues (Figure SI 12 A) which drive the central helix of the pAntp on the surface (Figure SI 12 B) that – as the contact ends – results the most interacting part (Figure SI 12 C).

The pAntp peptide stays fold in the case of the 9SiO(H,Na) and its main interactions are due to the ARG and LYS C-terminal residues (Figure SI 12 D). These residues are positively charged in this condition and the interaction with the surface is purely driven by the electrostatics of the negative silanol groups (Figure SI 12 E-F).

The contact with the 18SiO(H,Na) surface starts with the N-terminal residues (Figure SI 12 G). In particular, the ARG1 anchors to the surface throughout all the simulation (Figure SI 12 H-I).

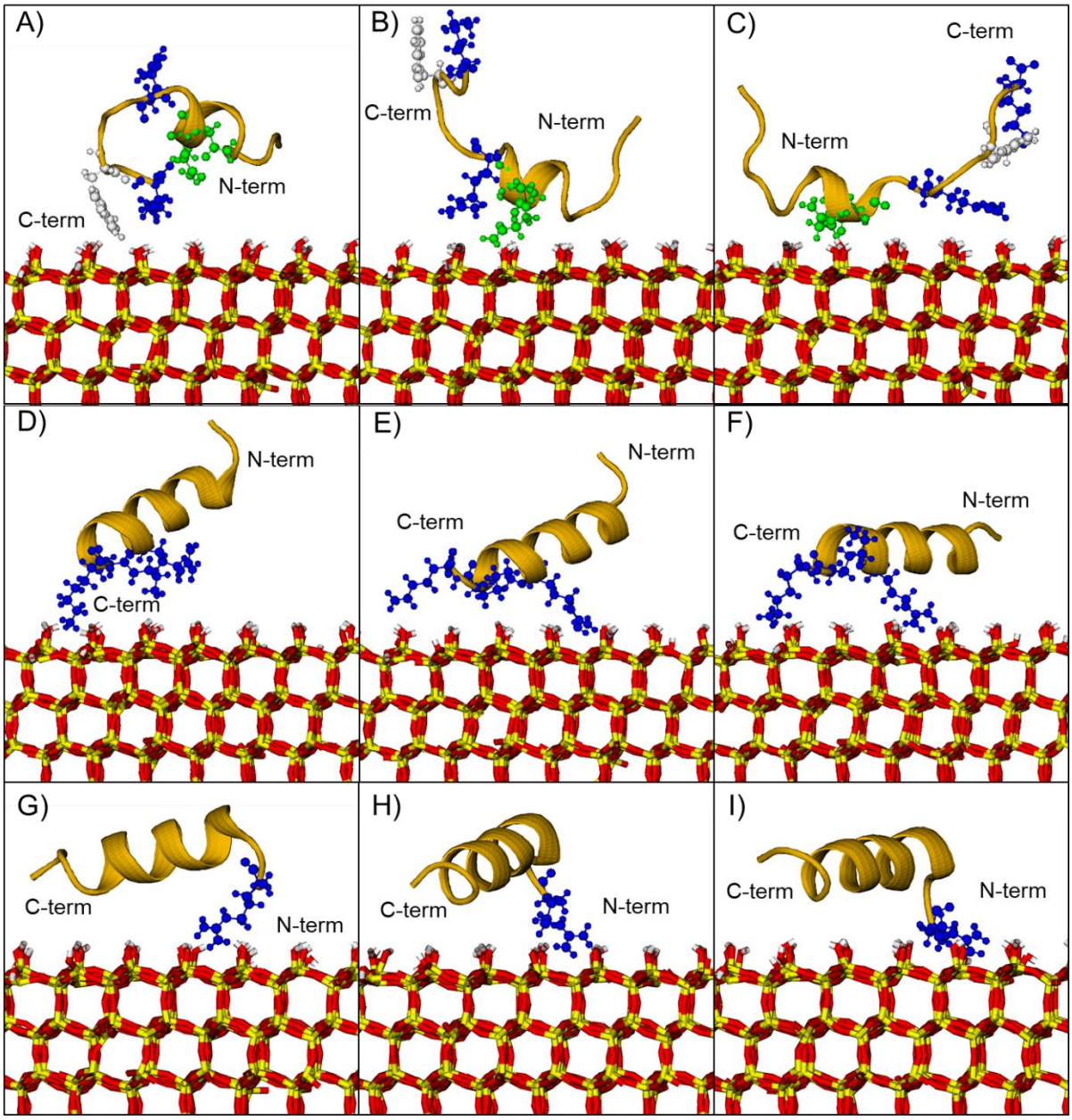

Figure SI 12 Snapshots of the contacts between the pAntp peptide with the SiOH (A,B,C), the 9SiO(H,Na) (D,E,F) and the 18SiO(H,Na) (G,H,I) surfaces: A,D,G) Initial contact; B,E,H) during contact; C,F,I) final configuration. The residues from Table 3.4 are highlighted: non-polar residues in white (TRP); basic residues in blue (LYS, ARG); polar residues in green (ASN,GLN). The N-term and the C-term are highlighted.

In Figure SI 13 are shown three snapshots of the systems PEP peptide – silica surface (SiOH surface Figure SI 13 A-C; 9SiO(H,Na) surface Figure SI 13 D-F; 18SiO(H,Na) surface Figure SI 13 G-I).

The contact with the surface SiOH begins with the N-terminal tail (Figure SI 13 A) that drives the peptide's core onto the surface (Figure SI 13 B) until the C-terminal tail reaches the surface where the N-terminal tail detaches (Figure SI 13 C) and the PEP founds itself stepping away from the surface.

Conversely, the contact with the 9SiO(H,Na) starts with the C-terminal tail and its charged residues – LYS and ARG (Figure SI 13 D) – then the N-terminal tail approaches the surface (Figure SI 13 E) and in the final configuration both tails are linked to the surface (Figure SI 13 F) resulting in a stable connection.

As for the 18SiO(H,Na) surface, the most interacting residue is the ARG19 of the C-terminal tail (Figure SI 13 G) that makes the first contact and push the peptide onto the surface (Figure SI 13 H-I).

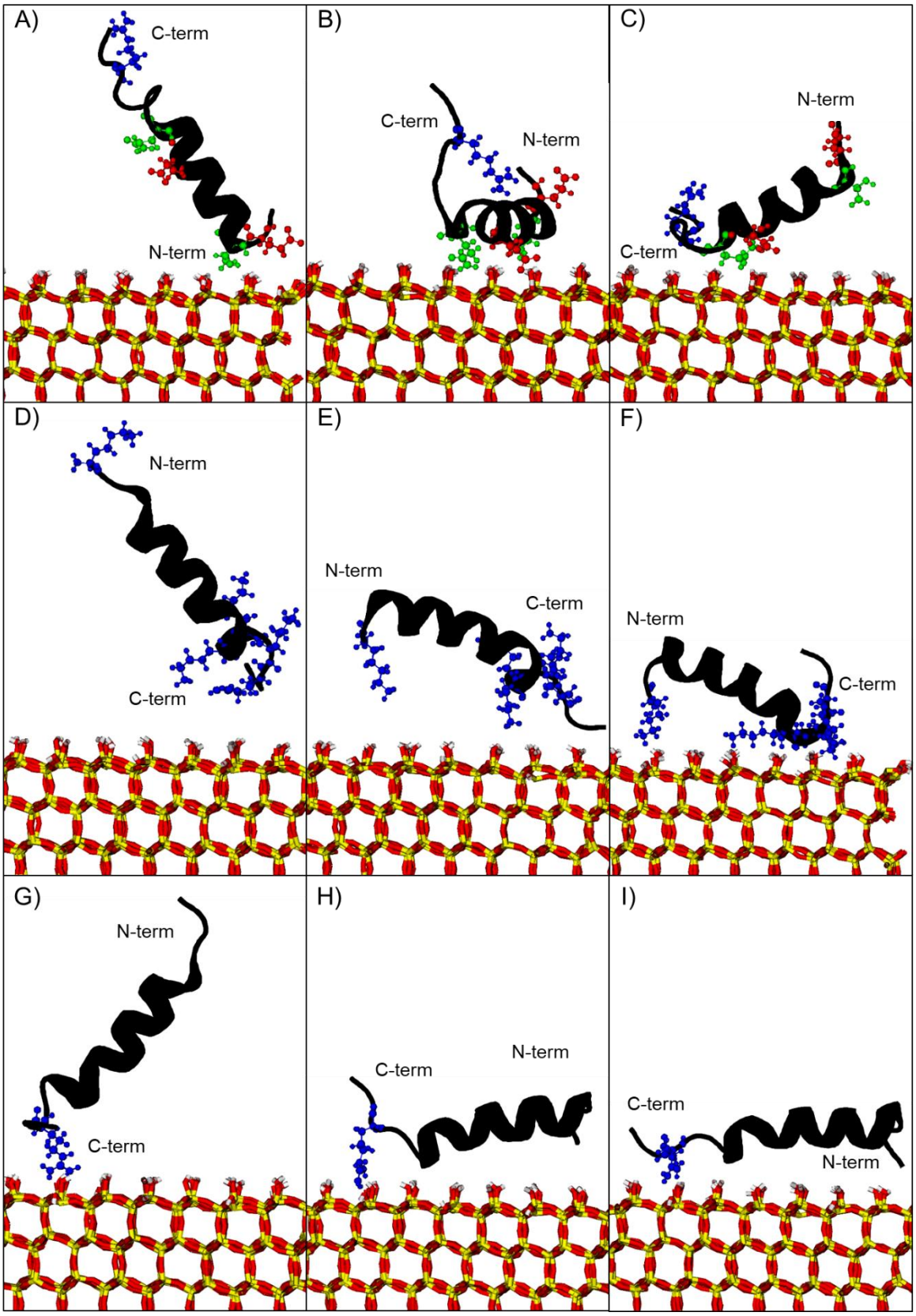

Figure SI 13 Snapshots of the contacts between the PEP peptide with the SiOH (A,B,C), the 9SiO(H,Na) (D,E,F) and the 18SiO(H,Na) (G,H,I) surfaces: A,D,G) Initial contact; B,E,H) during contact; C,F,I) final configuration. The residues from Table 3.4 are highlighted: basic residues in blue (LYS, ARG); polar residues in green (THR, GLN); acidic residue in red (GLU). The N-term and the C-term are highlighted.

In Figure SI 14 are shown three snapshots of the systems (ARG)9 peptide – silica surface (SiOH surface Figure SI 14 A-C; 9SiO(H,Na) surface Figure SI 14 D-F; 18SiO(H,Na) surface Figure SI 14 G-I).

As seen in Figure SI 2, there is no considerable contact between the (ARG)9 peptide and the SiOH surface and it can be seen in Figure SI 14 A-C, where only the C-terminal tail is found nearby the surface without making any stable contact.

Instead, the (ARG)9 makes a stable and long lasting contact with the 9SiO(H,Na) which is entirely driven by the N-terminal ARG (Figure SI 14 D-F).

Also the 18SiO(H,Na) interacts with the (ARG)9 peptide. Here, the conformation is very different, in fact the most interacting residues are in the C-terminal tail (Figure SI 14 G-H) and the conformation is most stable in an horizontal orientation (Figure SI 14 I).

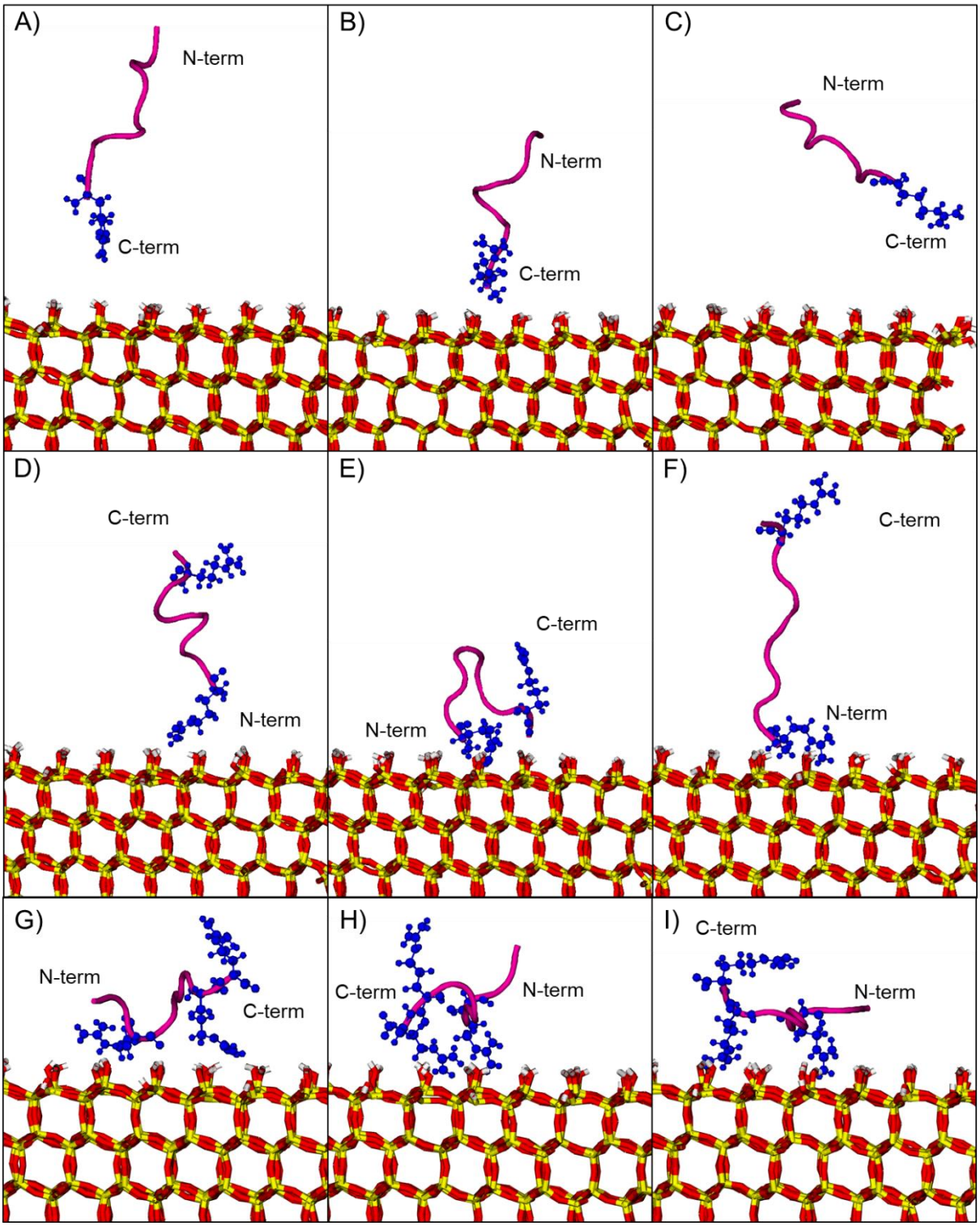

Figure SI 14 Snapshots of the contacts between the (ARG)9 peptide with the SiOH (A,B,C), the 9SiO(H,Na) (D,E,F) and the 18SiO(H,Na) (G,H,I) surfaces: A,D,G) Initial contact; B,E,H) during contact; C,F,I) final configuration. The residues from Table 3.4 are highlighted: basic residues in blue (ARG). The N-term and the C-term are highlighted.

In are shown three snapshots of the systems TAT peptide – silica surface (SiOH surface Figure SI 15 A-C; 9SiO(H,Na) surface Figure SI 15 D-F; 18SiO(H,Na) surface Figure SI 15 G-I).

As shown in Figure SI 15 A & Figure SI 15 B the TAT peptide tries to contact the SiOH surface with both the N-terminal and C-terminal tail, but – in the end – stays unfold in the water environment (Figure SI 15 C).

Regarding the TAT-9SiO(H,Na) system, the contact is neat and involves more residues: it starts with the N-terminal tail reaching the surface (Figure SI 15 D); then the peptide reorganize itself on the surface (Figure SI 15 E). In the end, the C-terminal tail interacts with the surface and the N-terminal tail in the water environment (Figure SI 15 F).

As for the 18SiO(H,Na) surface, even more residues are involved and the C-terminal is responsible for the first contact (Figure SI 15 G). Then, the ARG residues stabilize the conformation of the TAT peptide on the surface (Figure SI 15 H-I).

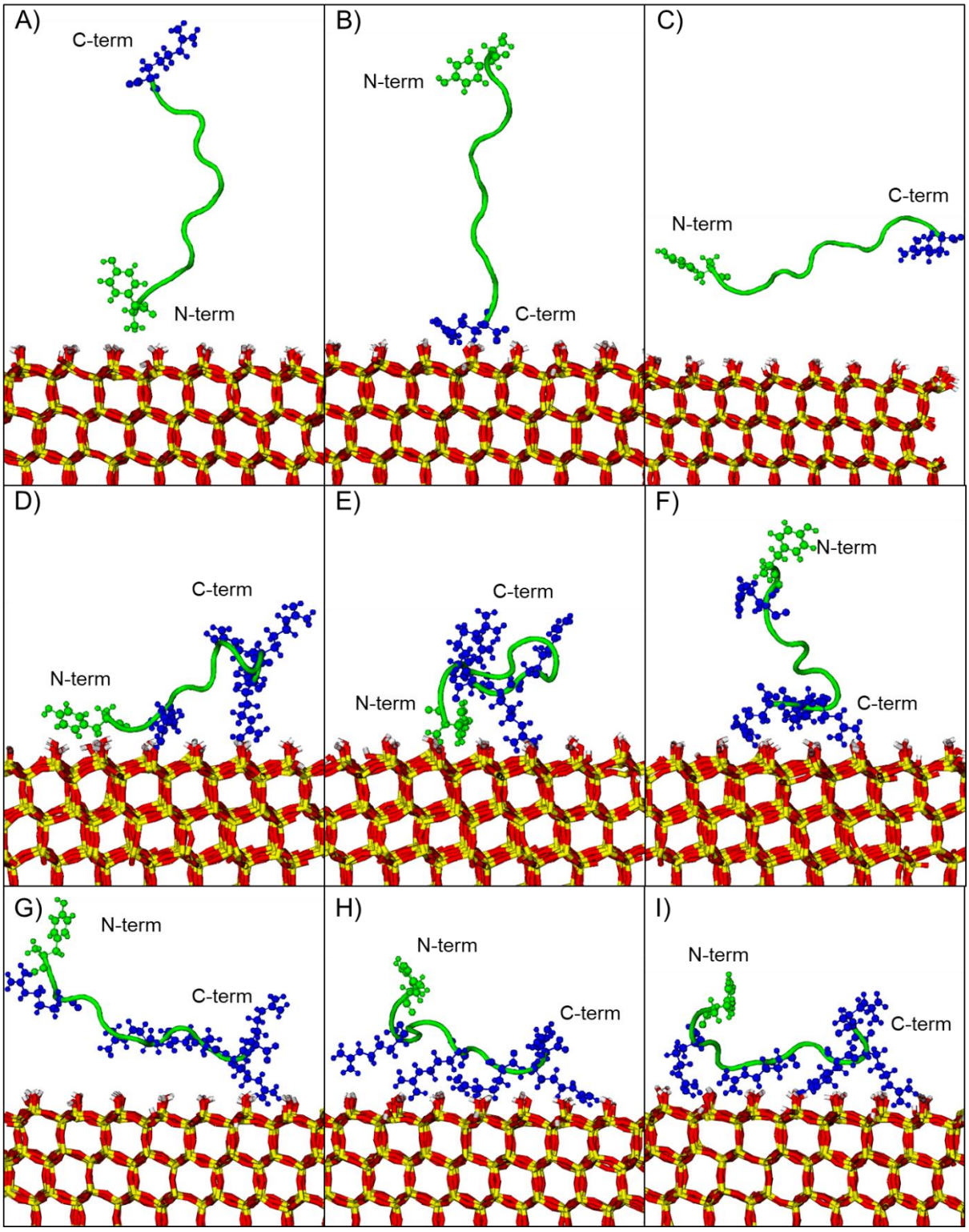

Figure SI 15 Snapshots of the contacts between the TAT peptide with the SiOH (A,B,C), the 9SiO(H,Na) (D,E,F) and the 18SiO(H,Na) (G,H,I) surfaces: A,D,G) Initial contact; B,E,H) during contact; C,F,I) final configuration. The residues from Table 3.4 are highlighted: basic residues in blue (ARG), polar residues in green (TYR, GLN). The N-term and the C-term are highlighted.

Convergence Analysis –SiOH Surface

In Figure SI 16 are reported the metadynamics analysis of the CADY peptide interacting with the SiOH surface. The convergence (Figure SI 16 B) is calculated as the difference between the local maximum along the distance CV between 1.5 and 2 nm and the local minimum along the distance CV between 0 and 0.5 nm. The Gaussian height (Figure SI 16 D) through the simulation time is also shown and its exponential trend is in line with the well-tempered recipe. Also the distance CV (Figure SI 16 C) through simulation time is reported for clarity, as it is possible to see how the peptide reach the surface several time, exploring multiple metastable state, as expected in such metadynamics simulation.

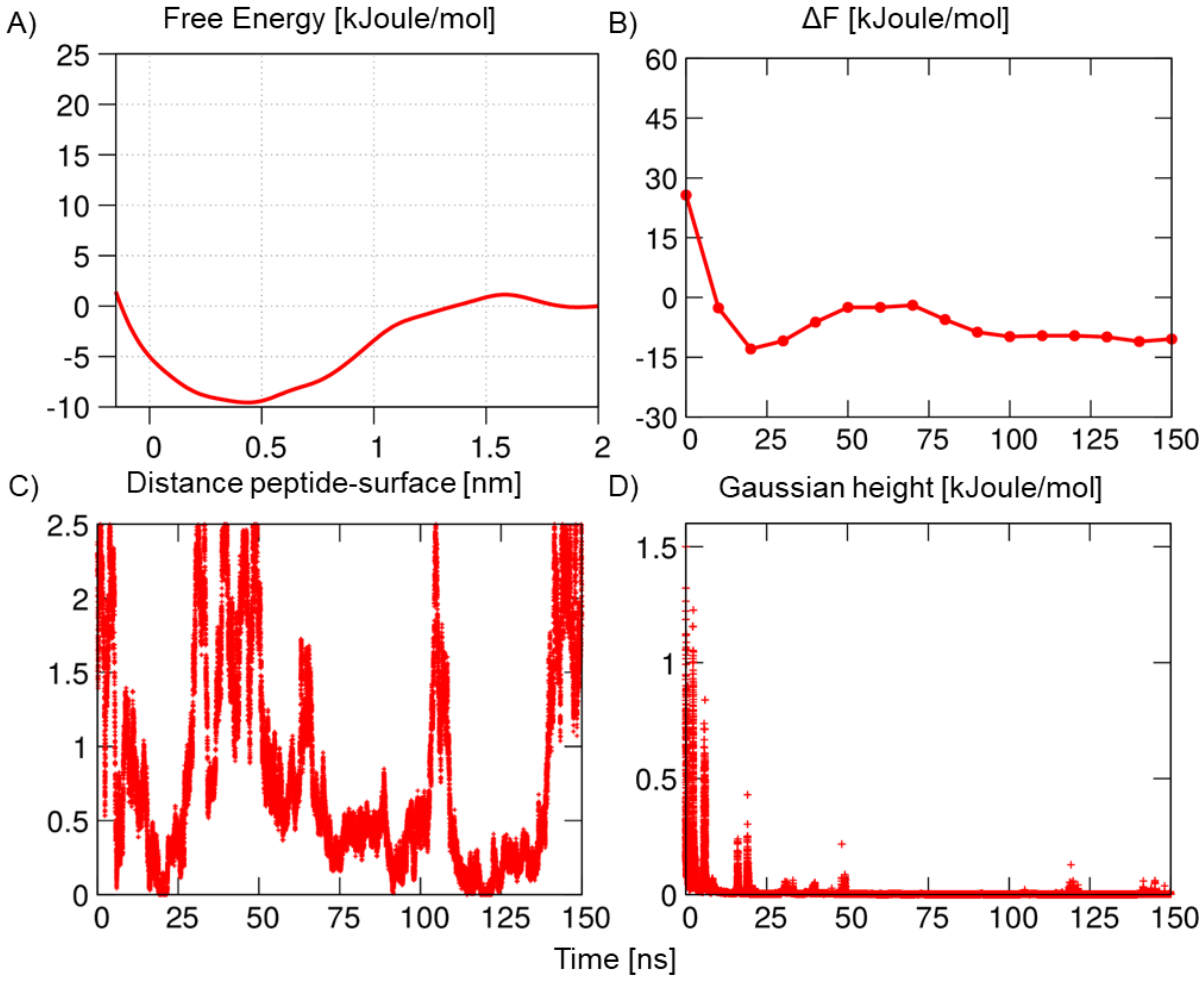

Figure SI 16 Metadynamics results of the CADY peptide interacting with the SiOH surface. A) Free energy profile; B) Convergence analysis; C) Distance CV through time; D) Gaussian Height.

In Figure SI 17 are reported the metadynamics analysis of the MAP peptide interacting with the SiOH surface. The convergence (Figure SI 17 B) is calculated as the difference between the local maximum along the distance CV between 1.5 and 2 nm and the local minimum along the distance CV between 0 and 1 nm. The Gaussian height (Figure SI 17 D) through the simulation time is also shown and its exponential trend is in line with the well-tempered

recipe. Also the distance CV (Figure SI 17 C) through simulation time is reported for clarity, as it is possible to see how the peptide reach the surface several time, exploring multiple metastable state, as expected in such metadynamics simulation.

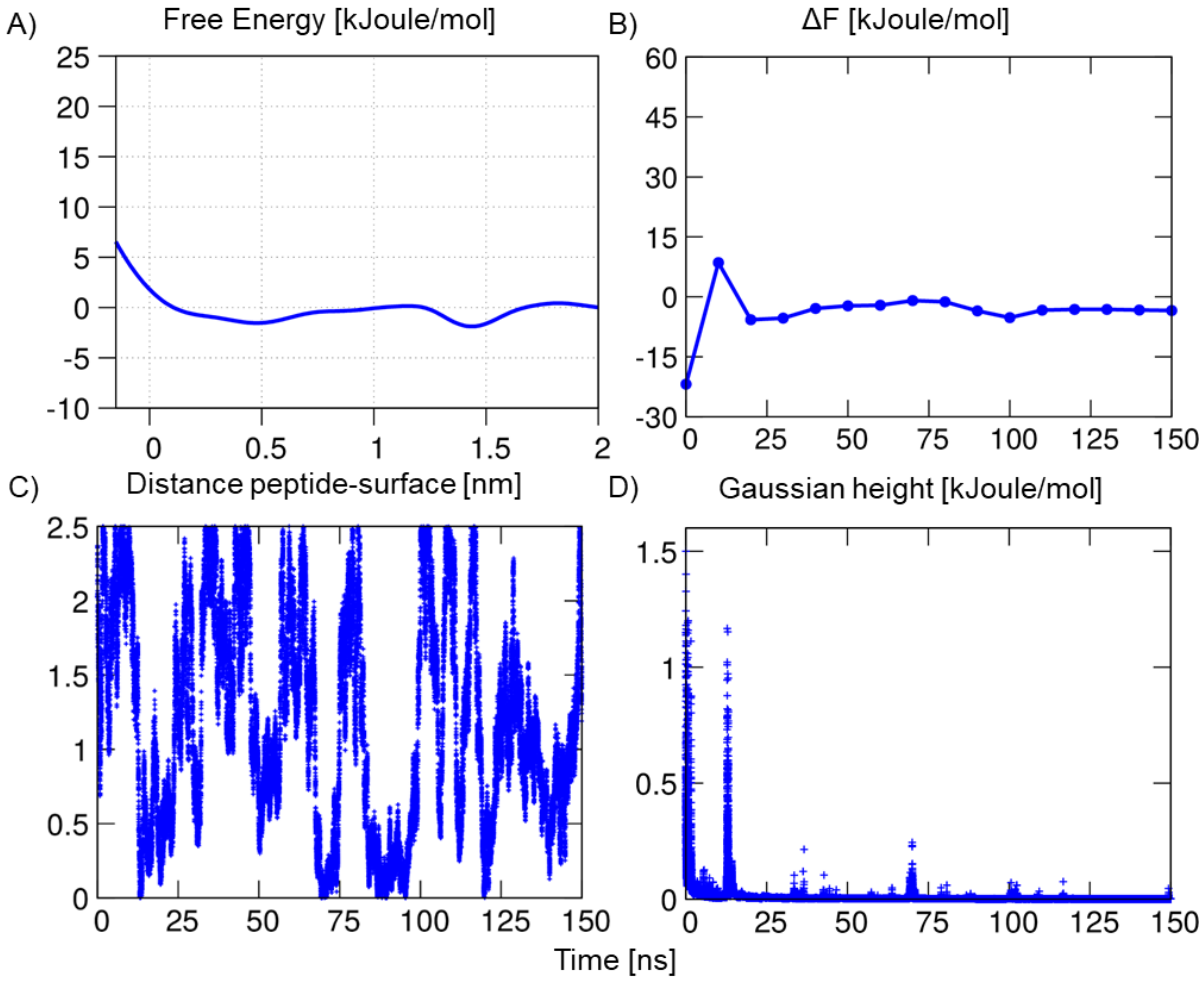

Figure SI 17 Metadynamics results of the MAP peptide interacting with the silica SiOH surface. A) Free energy profile; B) Convergence analysis; C) Distance CV through time; D) Gaussian Height.

In Figure SI 18 are reported the metadynamics analysis of the pAntp peptide interacting with the SiOH surface. The convergence (Figure SI 18 B) is calculated as the difference between the local maximum along the distance CV between 1.5 and 2 nm and the local minimum along the distance CV between 1 and 1.5 nm. The Gaussian height (Figure SI 18 D) through the simulation time is also shown and its exponential trend is in line with the well-tempered recipe. Also the distance CV (Figure SI 18 C) through simulation time is reported for clarity, as it is possible to see how the peptide reach the surface several time, exploring multiple metastable state, as expected in such metadynamics simulation.

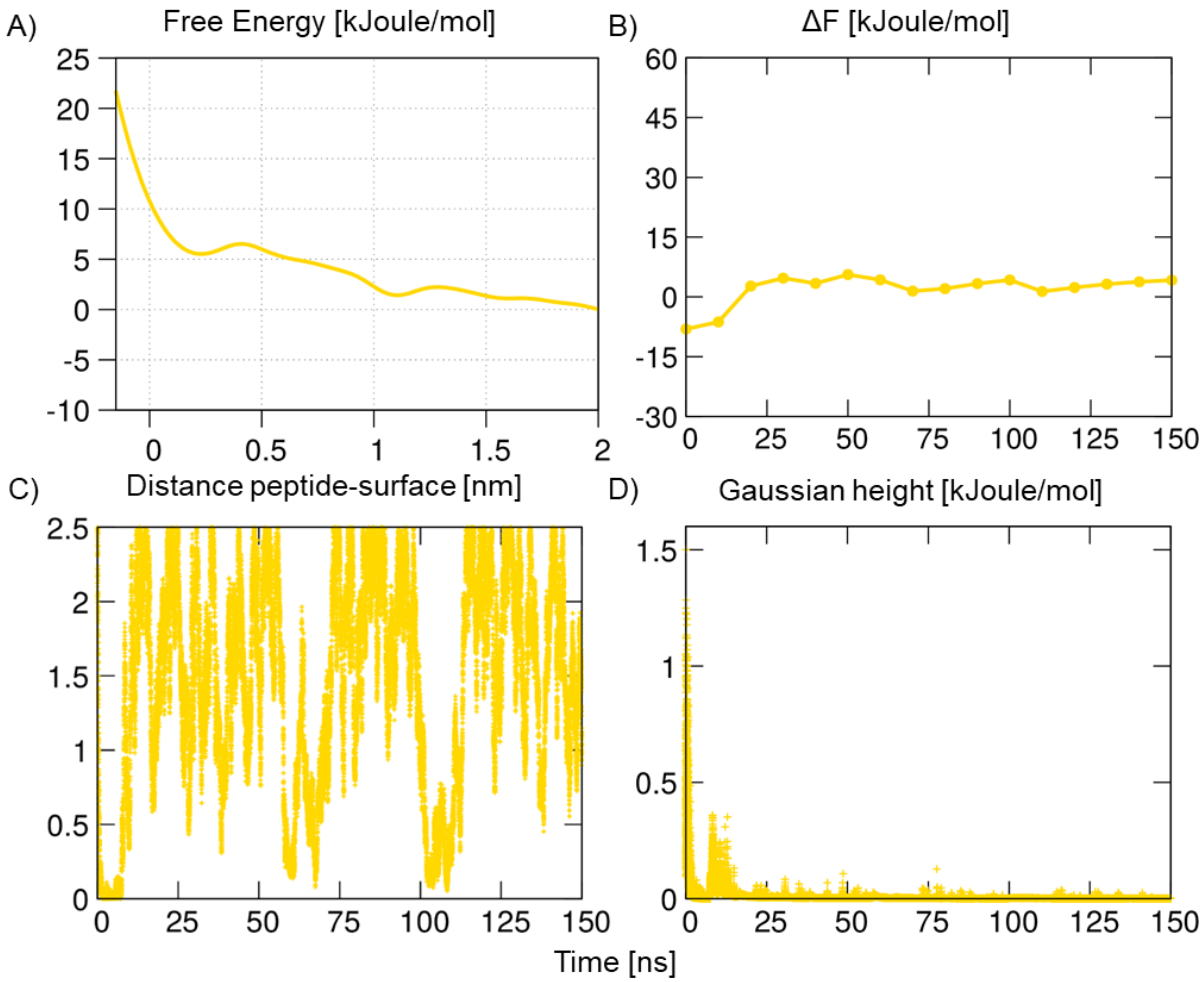

Figure SI 18 Metadynamics results of the pAntp peptide interacting with the SiOH surface. A) Free energy profile; B) Convergence analysis; C) Distance CV through time; D) Gaussian Height.

In Figure SI 19 are reported the metadynamics analysis of the PEP peptide interacting with the SiOH surface. The convergence (Figure SI 19 B) is calculated as the difference between the local maximum along the distance CV between 1.5 and 2 nm and the local minimum along the distance CV between 0 and 0.5 nm. The Gaussian height (Figure SI 19 D) through the simulation time is also shown and its exponential trend is in line with the well-tempered recipe. Also the distance CV (Figure SI 19 C) through simulation time is reported for clarity, as it is possible to see how the peptide reach the surface several time, exploring multiple metastable state, as expected in such metadynamics simulation.

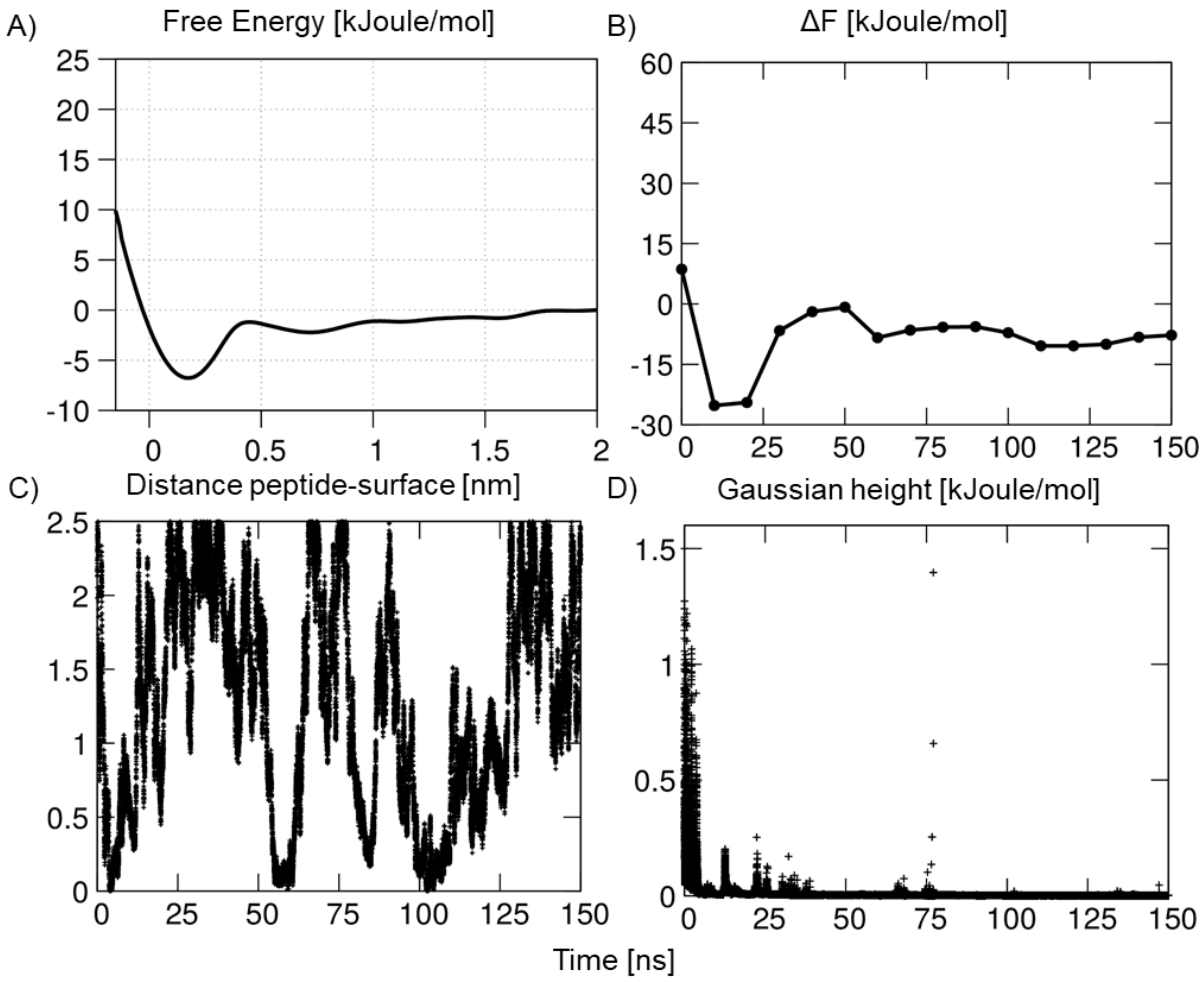

Figure SI 19 Metadynamics results of the PEP peptide interacting with the silica SiOH surface. A) Free energy profile; B) Convergence analysis; C) Distance CV through time; D) Gaussian Height.

In Figure SI 20 are reported the metadynamics analysis of the (ARG)9 peptide interacting with the SiOH surface. The convergence (Figure SI 20 B) is calculated as the difference between the local maximum along the distance CV between 0 and 0.5 nm and the local minimum along the distance CV between 1.5 and 2 nm. The Gaussian height (Figure SI 20 D) through the simulation time is also shown and its exponential trend is in line with the well-tempered recipe. Also the distance CV (Figure SI 20 C) through simulation time is reported for clarity, as it is possible to see how the peptide reach the surface several time, exploring multiple metastable state, as expected in such metadynamics simulation.

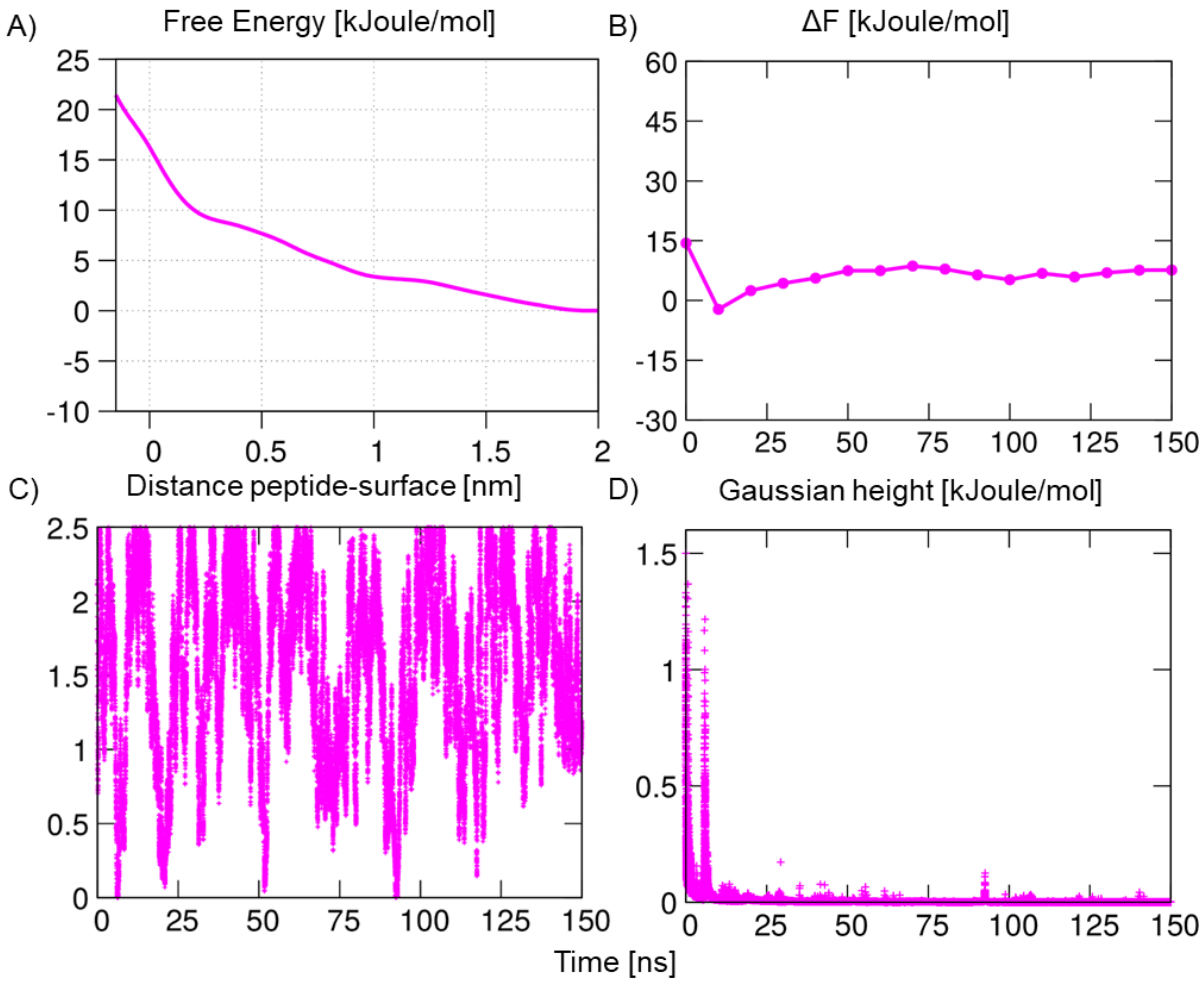

Figure SI 20 Metadynamics results of the (ARG)9 peptide interacting with the SiOH surface. A) Free energy profile; B) Convergence analysis; C) Distance CV through time; D) Gaussian Height.

In Figure SI 21 are reported the metadynamics analysis of the TAT peptide interacting with the SiOH surface. The convergence (Figure SI 21 B) is calculated as the difference between the local maximum along the distance CV between 0 and 0.5 nm and the local minimum along the distance CV between 1.5 and 2 nm. The Gaussian height (Figure SI 21 D) through the simulation time is also shown and its exponential trend is in line with the well-tempered recipe. Also the distance CV (Figure SI 21 C) through simulation time is reported for clarity, as it is possible to see how the peptide reach the surface several time, exploring multiple metastable state, as expected in such metadynamics simulation.

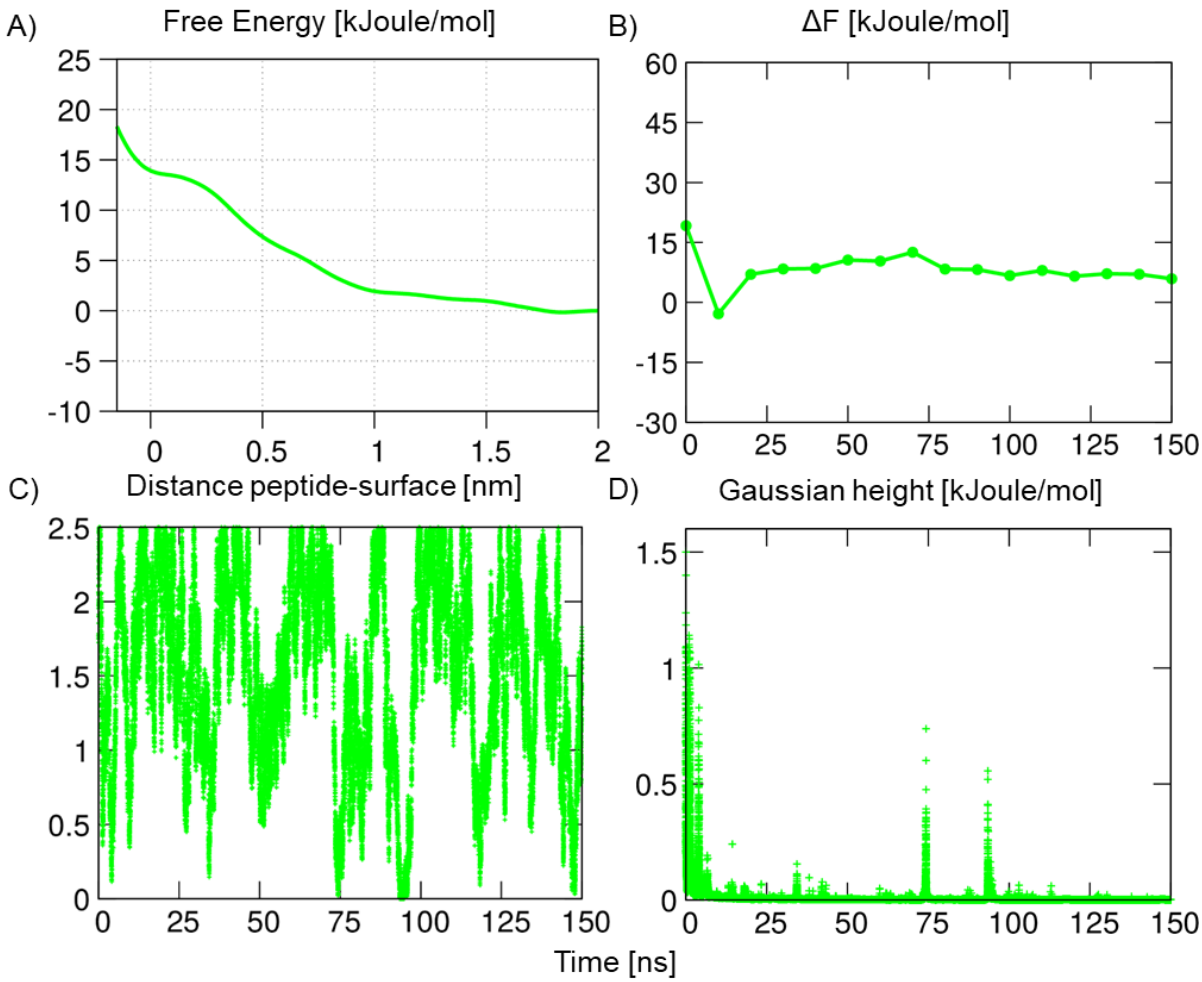

Figure SI 21 Metadynamics results of the TAT peptide interacting with the SiOH surface. A) Free energy profile; B) Convergence analysis; C) Distance CV through time; D) Gaussian Height.

Convergence Analysis – 9SiO(H,Na) Surface

In Figure SI 22 are reported the metadynamics analysis of the CADY peptide interacting with the 9SiO(H,Na) surface. The convergence (Figure SI 22 B) is calculated as the difference between the local maximum along the distance CV between 1.5 and 2 nm and the local minimum along the distance CV between 0 and 0.5 nm. The Gaussian height (Figure SI 22 D) through the simulation time is also shown and its exponential trend is in line with the well-tempered recipe. Also the distance CV (Figure SI 22 C) through simulation time is reported for clarity, as it is possible to see how the peptide reach the surface several time, exploring multiple metastable state, as expected in such metadynamics simulation.

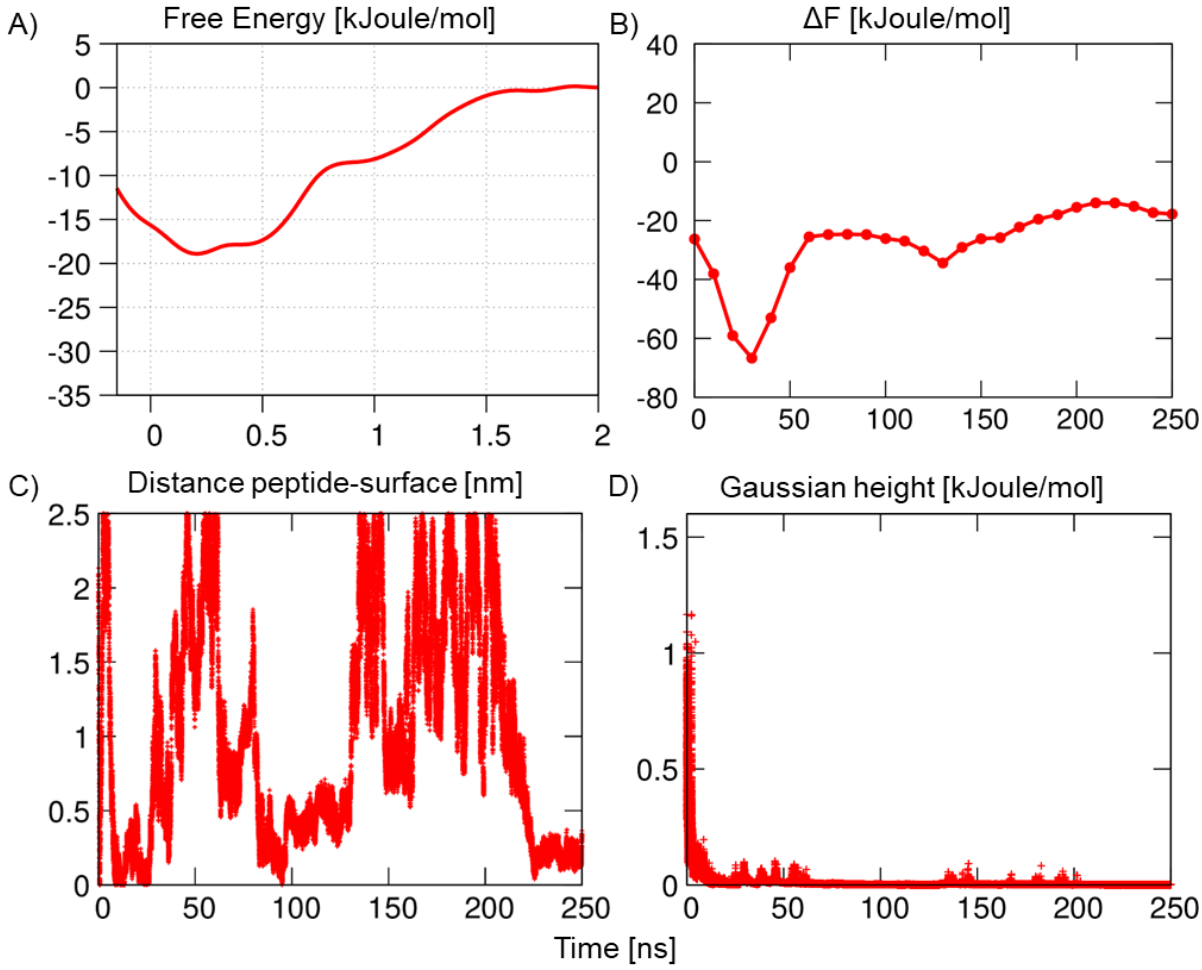

Figure SI 22 Metadynamics results of the CADY peptide interacting with the 9SiO(H,Na) surface. A) Free energy profile; B) Convergence analysis; C) Distance CV through time; D) Gaussian Height.

In Figure SI 23 are reported the metadynamics analysis of the MAP peptide interacting with the 9SiO(H,Na) surface. The convergence (Figure SI 23 B) is calculated as the difference between the local maximum along the distance CV between 1.5 and 2 nm and the local minimum along the distance CV between 0 and 0.5 nm. The Gaussian height (Figure SI 23 D) through the simulation time is also shown and its exponential trend is in line with the well-

tempered recipe. Also the distance CV (Figure SI 23 C) through simulation time is reported for clarity, as it is possible to see how the peptide reach the surface several time, exploring multiple metastable state, as expected in such metadynamics simulation.

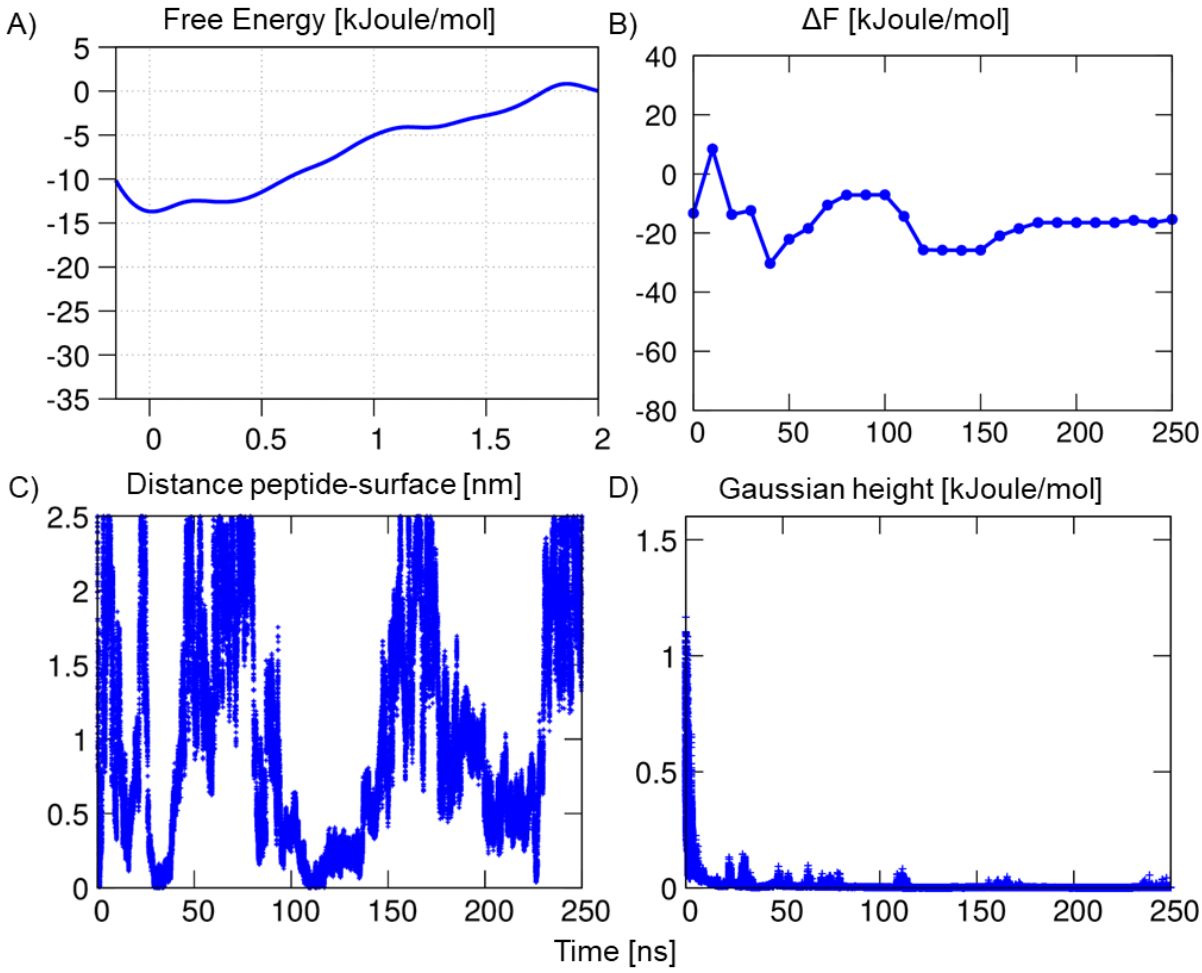

Figure SI 23 Metadynamics results of the MAP peptide interacting with the 9SiO(H,Na) surface. A) Free energy profile; B) Convergence analysis; C) Distance CV through time; D) Gaussian Height.

In Figure SI 24 are reported the metadynamics analysis of the pAntp peptide interacting with the 9SiO(H,Na) surface. The convergence (Figure SI 24 B) is calculated as the difference between the local maximum along the distance CV between 1.5 and 2 nm and the local minimum along the distance CV between 0 and 0.5 nm. The Gaussian height (Figure SI 24 D) through the simulation time is also shown and its exponential trend is in line with the well-tempered recipe. Also the distance CV (Figure SI 24 C) through simulation time is reported for clarity, as it is possible to see how the peptide reach the surface several time, exploring multiple metastable state, as expected in such metadynamics simulation.

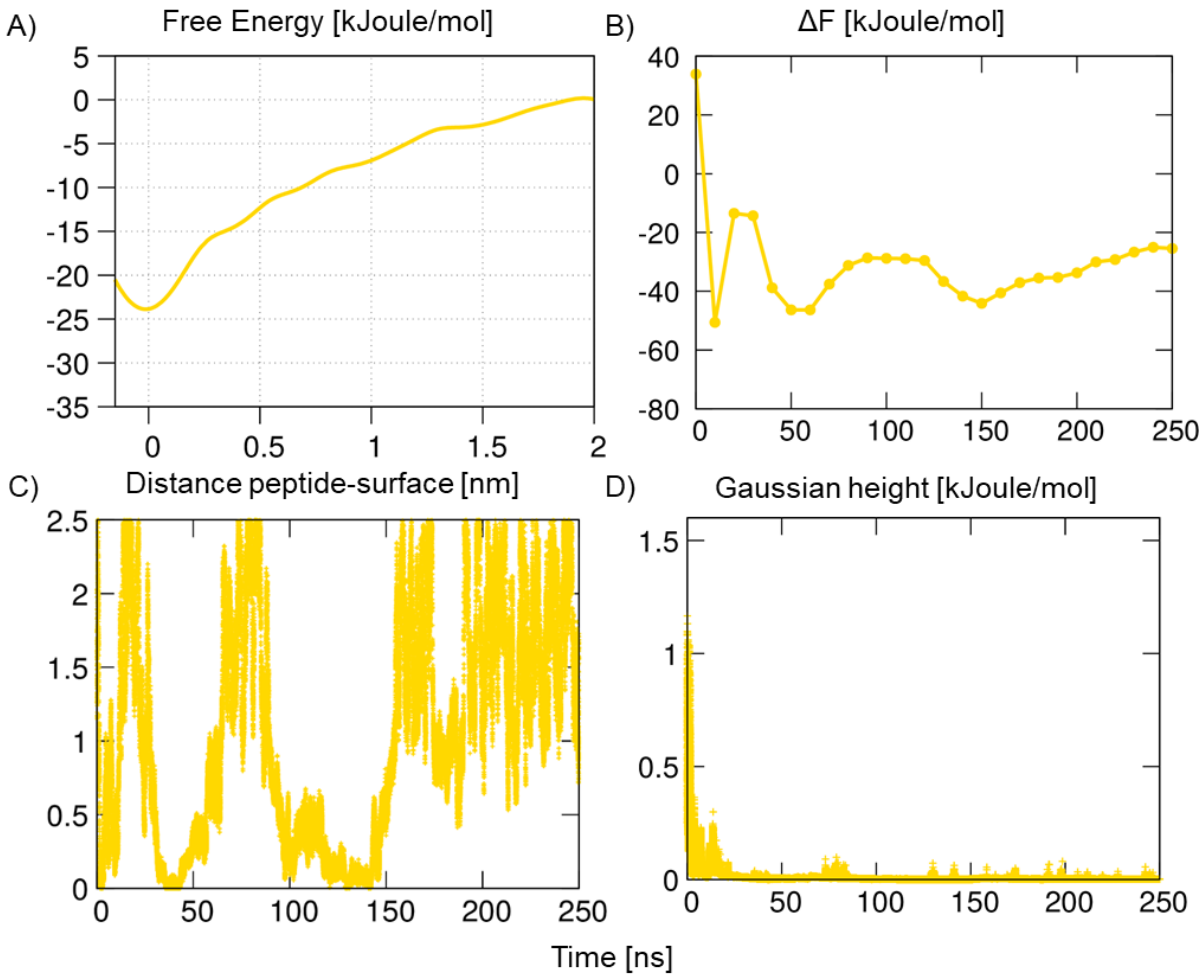

Figure SI 24 Metadynamics results of the pAntp peptide interacting with the 9SiO(H,Na) surface. A) Free energy profile; B) Convergence analysis; C) Distance CV through time; D) Gaussian Height.

In Figure SI 25 are reported the metadynamics analysis of the PEP peptide interacting with the 9SiO(H,Na) surface. The convergence (Figure SI 25 B) is calculated as the difference between the local maximum along the distance CV between 1.5 and 2 nm and the local minimum along the distance CV between 0 and 0.5 nm. The Gaussian height (Figure SI 25 D) through the simulation time is also shown and its exponential trend is in line with the well-tempered recipe. Also the distance CV (Figure SI 25 C) through simulation time is reported for clarity, as it is possible to see how the peptide reach the surface several time, exploring multiple metastable state, as expected in such metadynamics simulation.

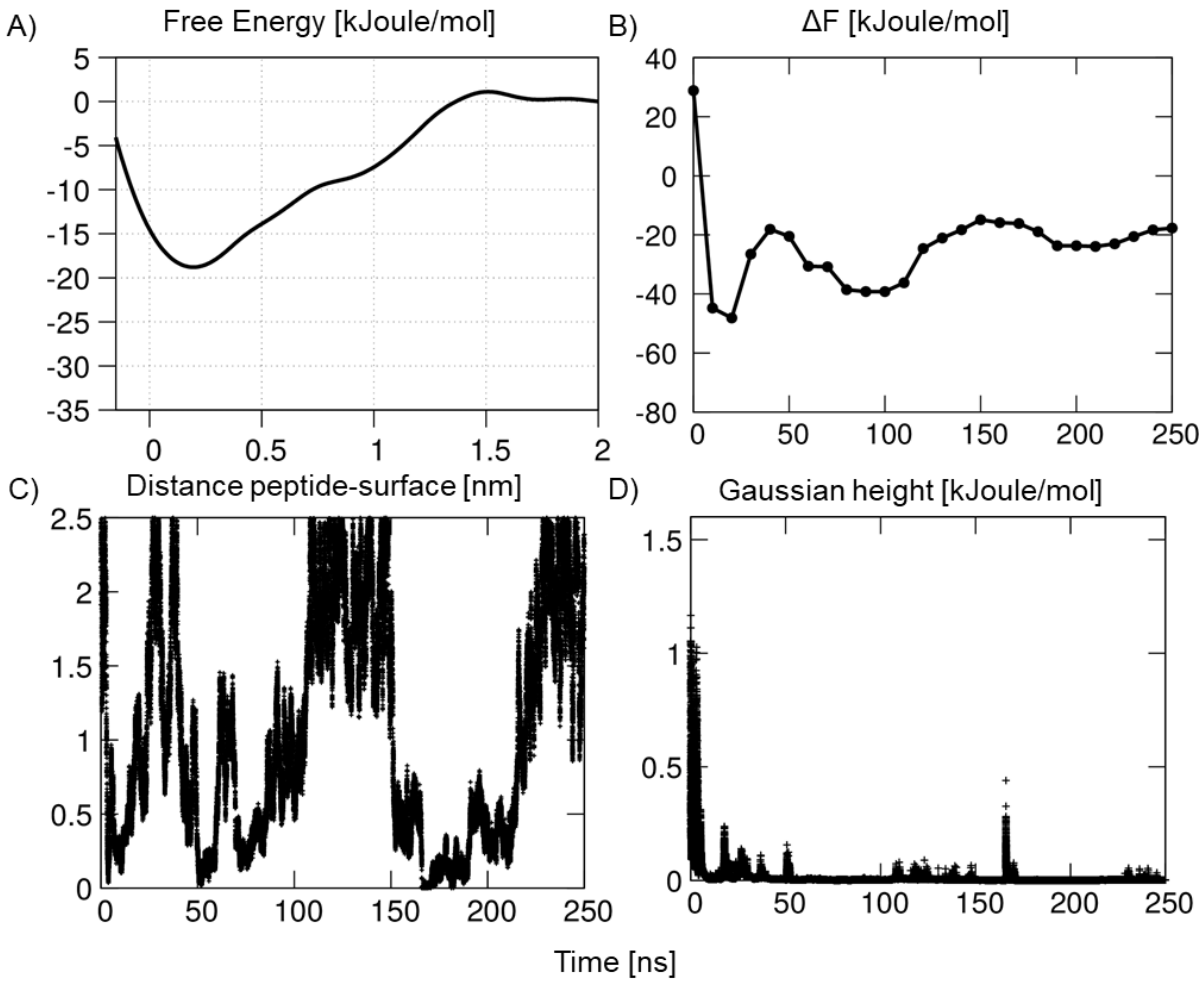

Figure SI 25 Metadynamics results of the PEP peptide interacting with the 9SiO(H,Na) surface. A) Free energy profile; B) Convergence analysis; C) Distance CV through time; D) Gaussian Height.

In Figure SI 26 are reported the metadynamics analysis of the (ARG)9 peptide interacting with the 9SiO(H,Na) surface. The convergence (Figure SI 26 B) is calculated as the difference between the local maximum along the distance CV between 1.5 and 2 nm and the local minimum along the distance CV between 0 and 0.5 nm. The Gaussian height (Figure SI 26 D) through the simulation time is also shown and its exponential trend is in line with the well-tempered recipe. Also the distance CV (Figure SI 26 C) through simulation time is reported for clarity, as it is possible to see how the peptide reach the surface several time, exploring multiple metastable state, as expected in such metadynamics simulation.

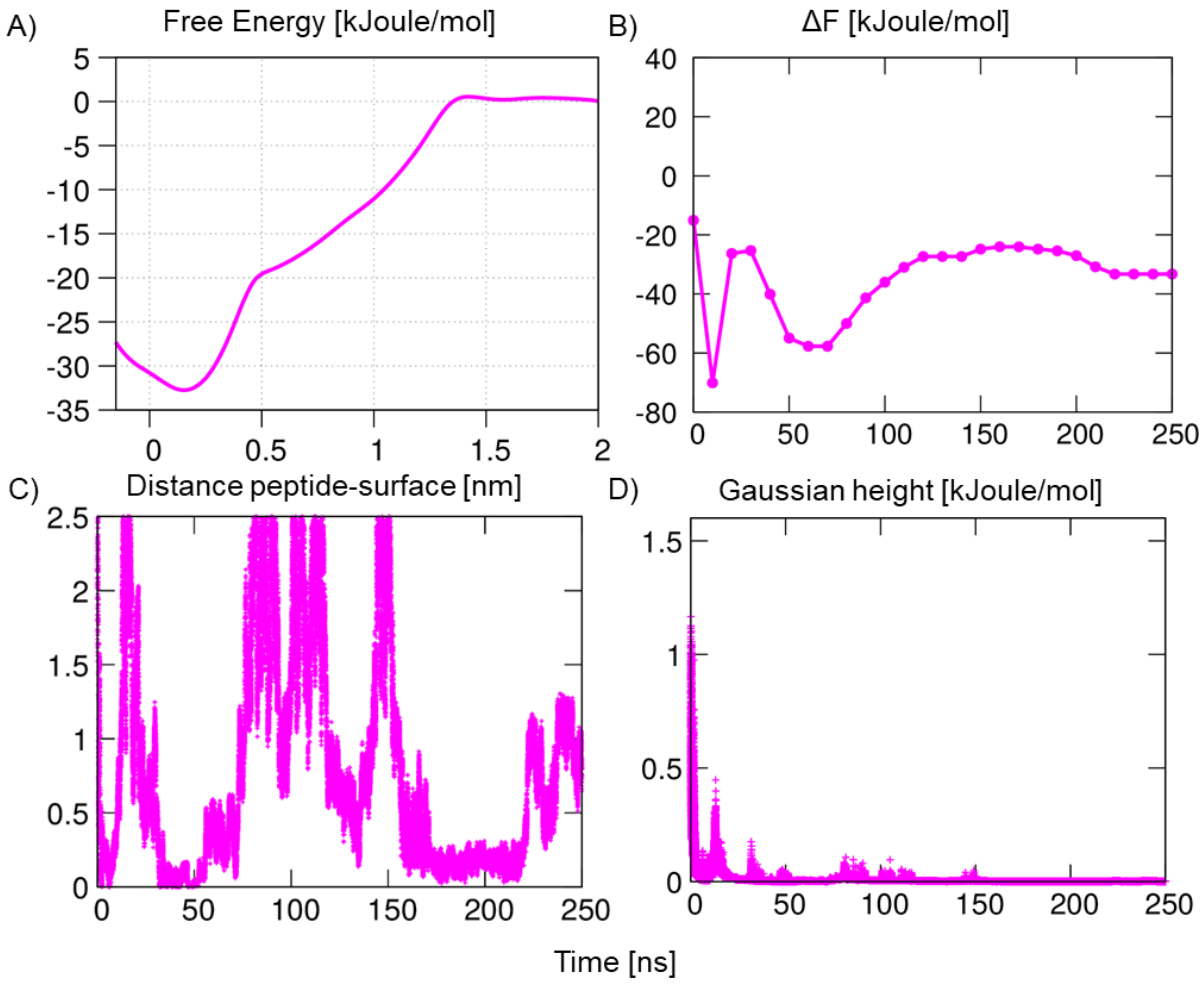

Figure SI 26 Metadynamics results of the (ARG)9 peptide interacting with the 9SiO(H,Na) surface. A) Free energy profile; B) Convergence analysis; C) Distance CV through time; D) Gaussian Height.

In Figure SI 27 are reported the metadynamics analysis of the TAT peptide interacting with the 9SiO(H,Na) surface. The convergence (Figure SI 27 B) is calculated as the difference between the local maximum along the distance CV between 1.5 and 2 nm and the local minimum along the distance CV between 0 and 0.5 nm. The Gaussian height (Figure SI 27 D) through the simulation time is also shown and its exponential trend is in line with the well-tempered recipe. Also the distance CV (Figure SI 27 C) through simulation time is reported for clarity, as it is possible to see how the peptide reach the surface several time, exploring multiple metastable state, as expected in such metadynamics simulation.

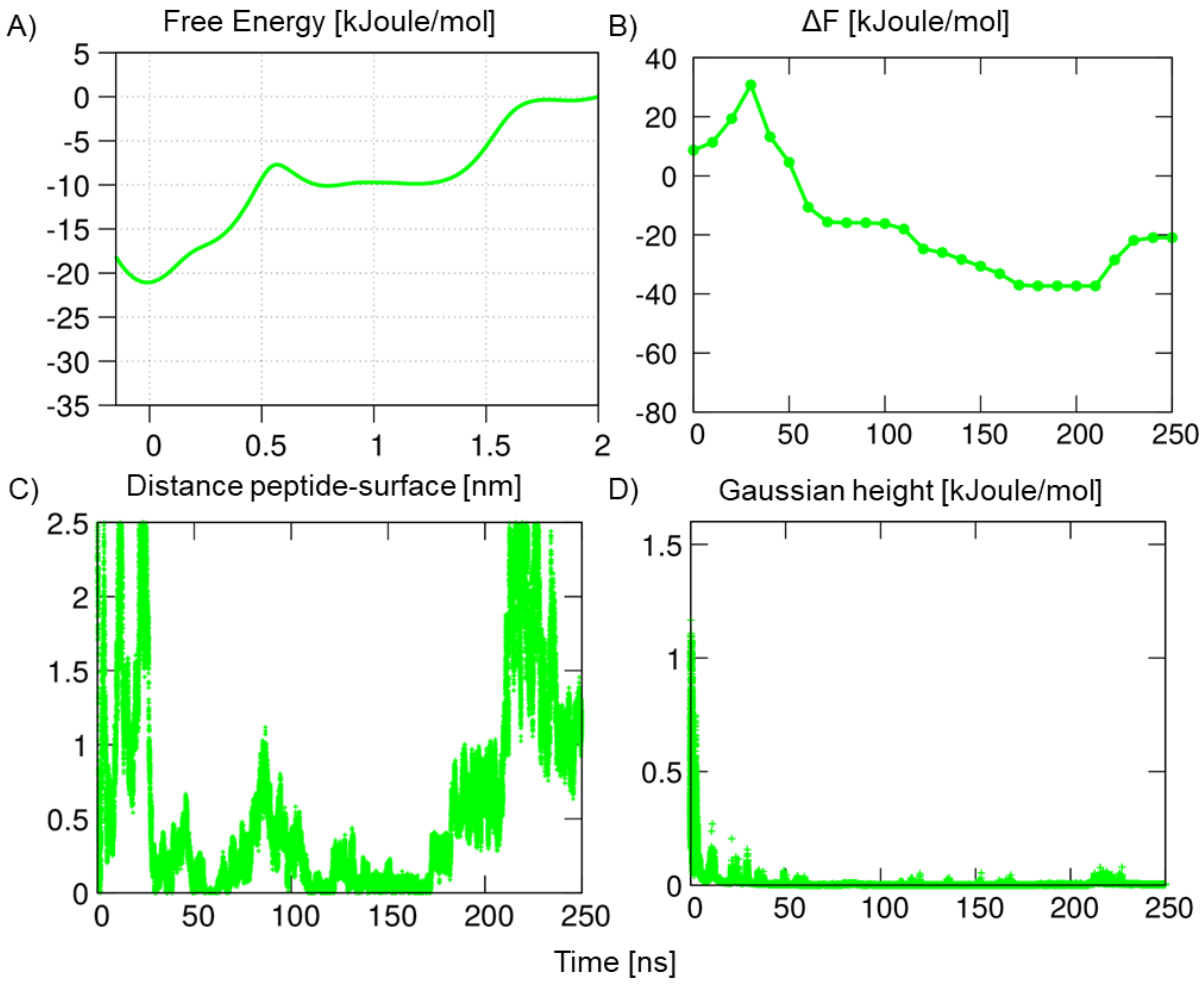

Figure SI 27 Metadynamics results of the TAT peptide interacting with the 9SiO(H,Na) surface. A) Free energy profile; B) Convergence analysis; C) Distance CV through time; D) Gaussian Height.

Convergence Analysis – 18SiO(H,Na) Surface

In Figure SI 28 are reported the metadynamics analysis of the CADY peptide interacting with the 18SiO(H,Na) surface. The convergence (Figure SI 28 B) is calculated as the difference between the local maximum along the distance CV between 1.5 and 2 nm and the local minimum along the distance CV between 0 and 0.5 nm. The Gaussian height (Figure SI 28 D) through the simulation time is also shown and its exponential trend is in line with the well-tempered recipe. Also the distance CV (Figure SI 28 C) through simulation time is reported for clarity, as it is possible to see how the peptide reach the surface several time, exploring multiple metastable state, as expected in such metadynamics simulation.

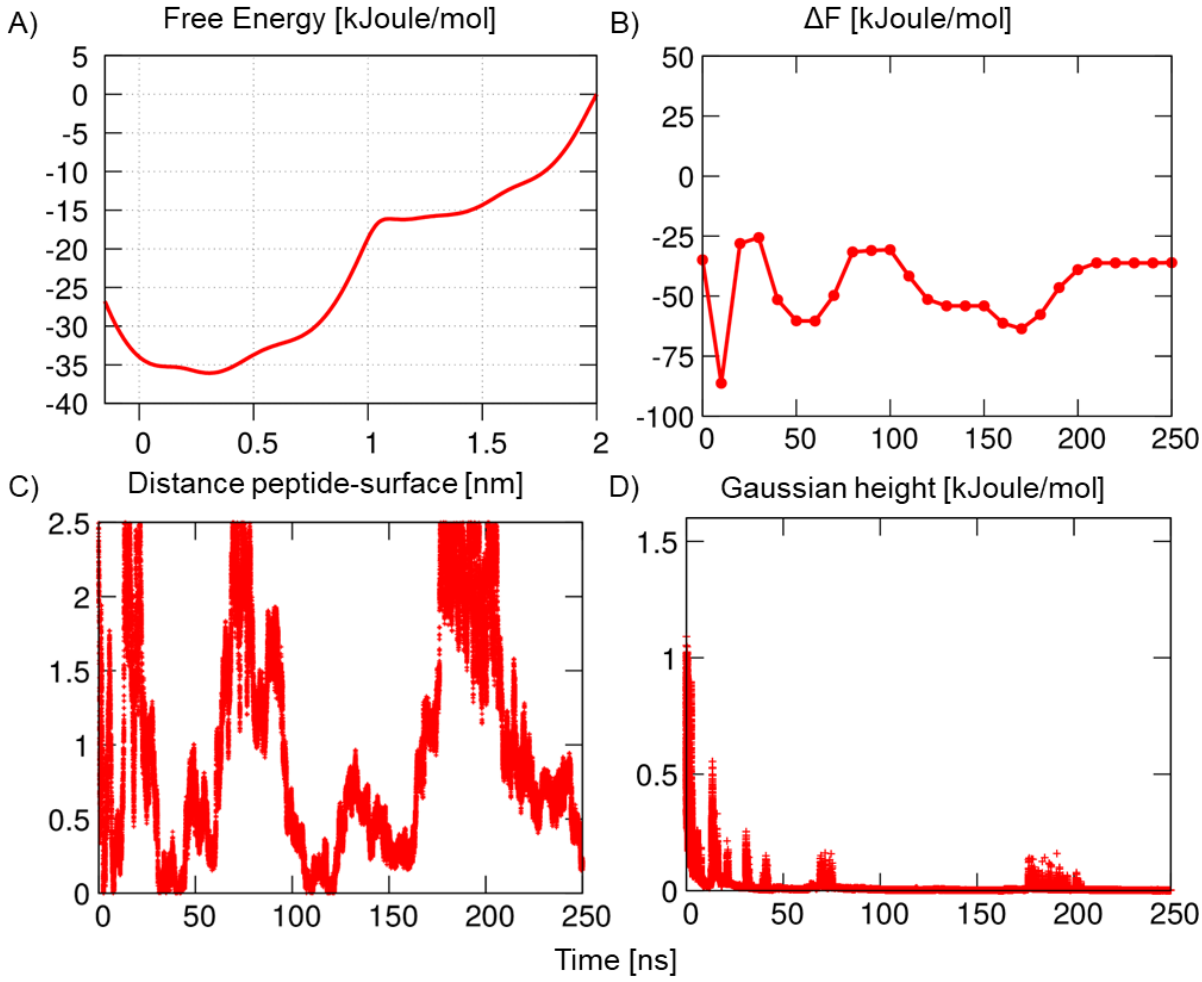

Figure SI 28 Metadynamics results of the CADY peptide interacting with the 18SiO(H,Na) surface. A) Free energy profile; B) Convergence analysis; C) Distance CV through time; D) Gaussian Height.

In Figure SI 29 are reported the metadynamics analysis of the MAP peptide interacting with the 18SiO(H,Na) surface. The convergence (Figure SI 29 B) is calculated as the difference between the local maximum along the distance CV between 1.5 and 2 nm and the local minimum along the distance CV between 0 and 0.5 nm. The Gaussian height (Figure SI 29 D) through the simulation time is also shown and its exponential trend is in line with the well-

tempered recipe. Also the distance CV (Figure SI 29 C) through simulation time is reported for clarity, as it is possible to see how the peptide reach the surface several time, exploring multiple metastable state, as expected in such metadynamics simulation.

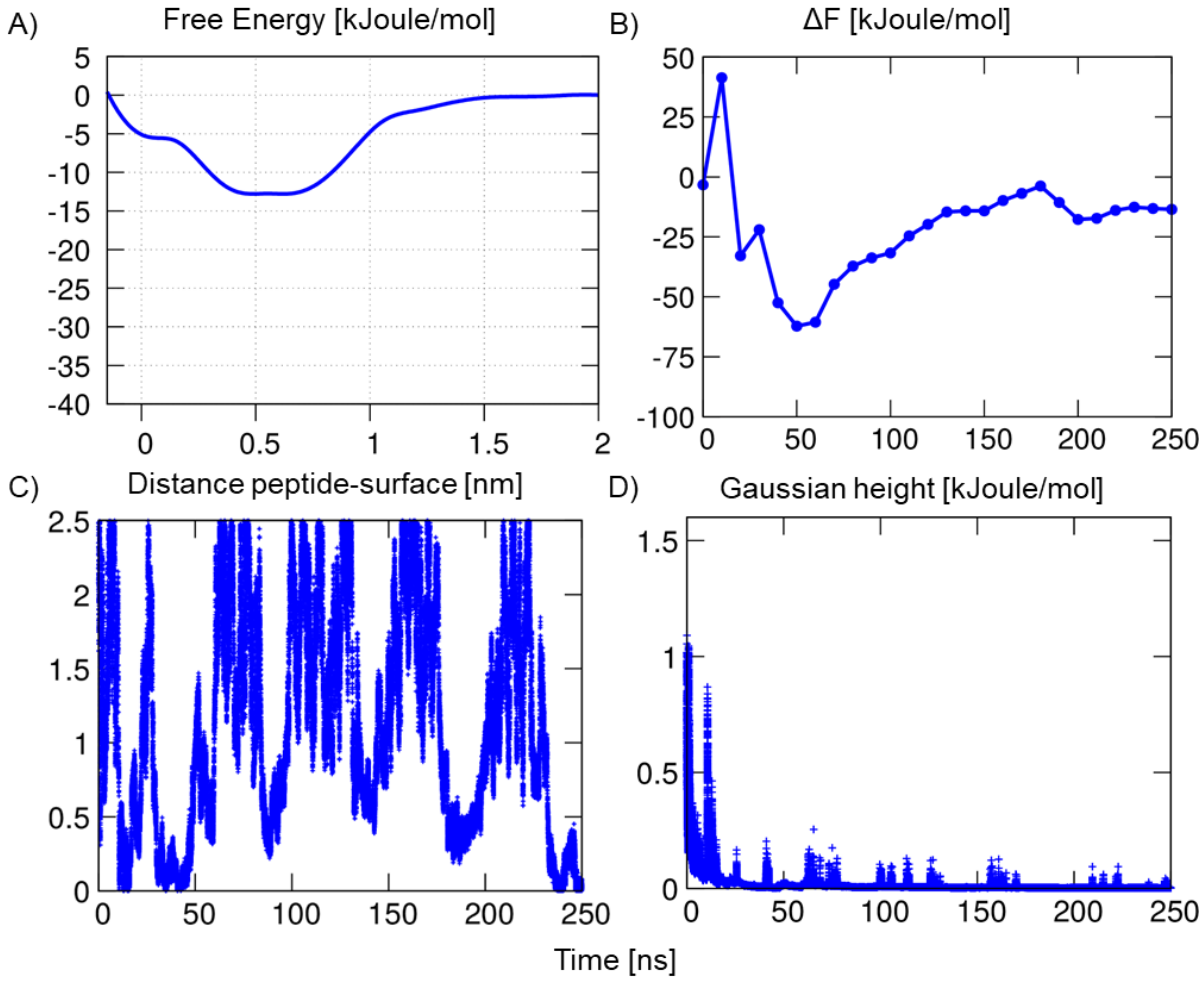

Figure SI 29 Metadynamics results of the MAP peptide interacting with the 18SiO(H,Na) surface. A) Free energy profile; B) Convergence analysis; C) Distance CV through time; D) Gaussian Height.

In Figure SI 30 are reported the metadynamics analysis of the pAntp peptide interacting with the 18SiO(H,Na) surface. The convergence (Figure SI 30 B) is calculated as the difference between the local maximum along the distance CV between 1.5 and 2 nm and the local minimum along the distance CV between 0 and 0.5 nm. The Gaussian height (Figure SI 30 D) through the simulation time is also shown and its exponential trend is in line with the well-tempered recipe. Also the distance CV (Figure SI 30 C) through simulation time is reported for clarity, as it is possible to see how the peptide reach the surface several time, exploring multiple metastable state, as expected in such metadynamics simulation.

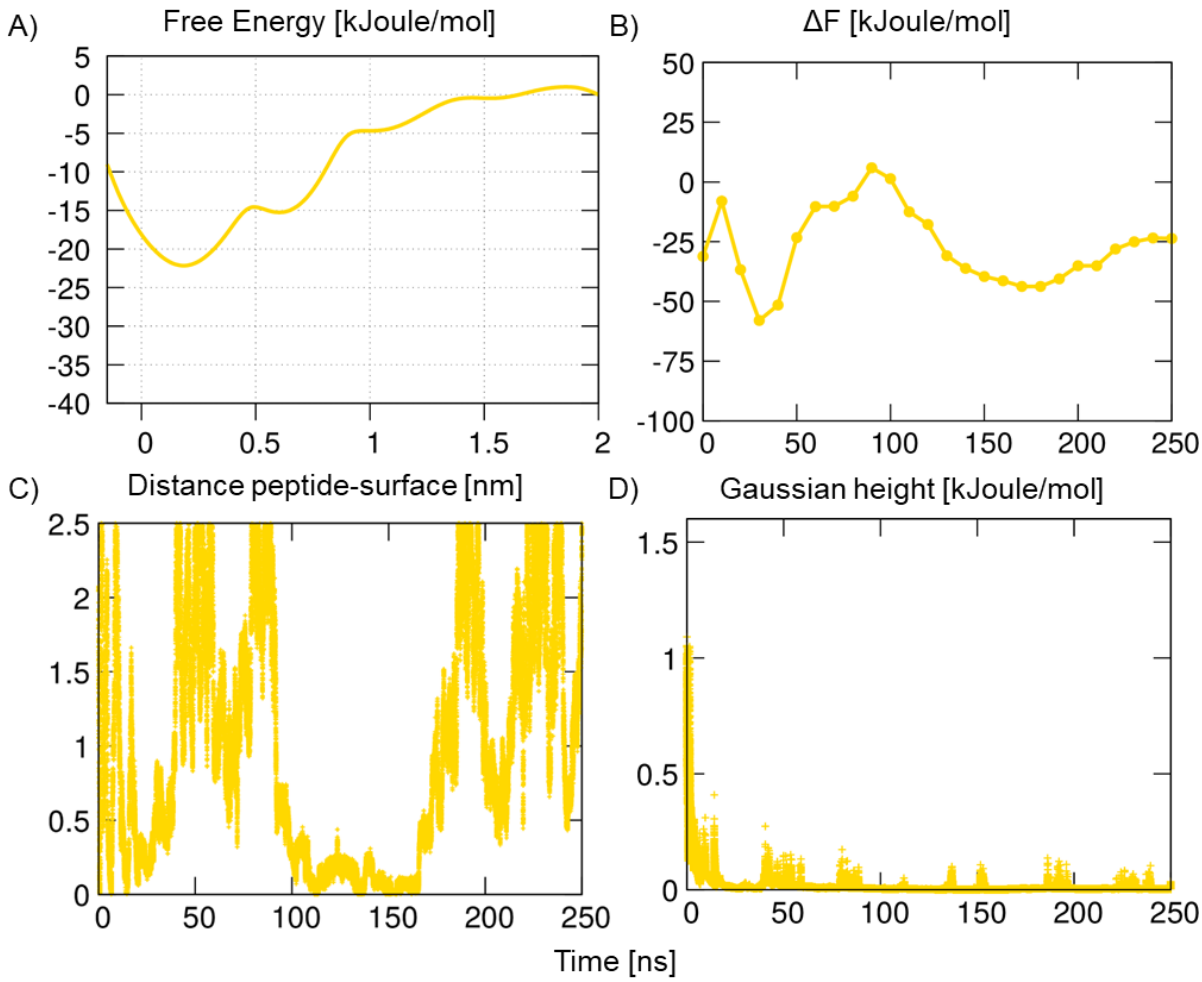

Figure SI 30 Metadynamics results of the pAntp peptide interacting with the 18SiO(H,Na) surface. A) Free energy profile; B) Convergence analysis; C) Distance CV through time; D) Gaussian Height.

In Figure SI 31 are reported the metadynamics analysis of the PEP peptide interacting with the 18SiO(H,Na) surface. The convergence (Figure SI 31 B) is calculated as the difference between the local maximum along the distance CV between 1.5 and 2 nm and the local minimum along the distance CV between 0 and 0.5 nm. The Gaussian height (Figure SI 31 D) through the simulation time is also shown and its exponential trend is in line with the well-tempered recipe. Also the distance CV (Figure SI 31 C) through simulation time is reported for clarity, as it is possible to see how the peptide reach the surface several time, exploring multiple metastable state, as expected in such metadynamics simulation.

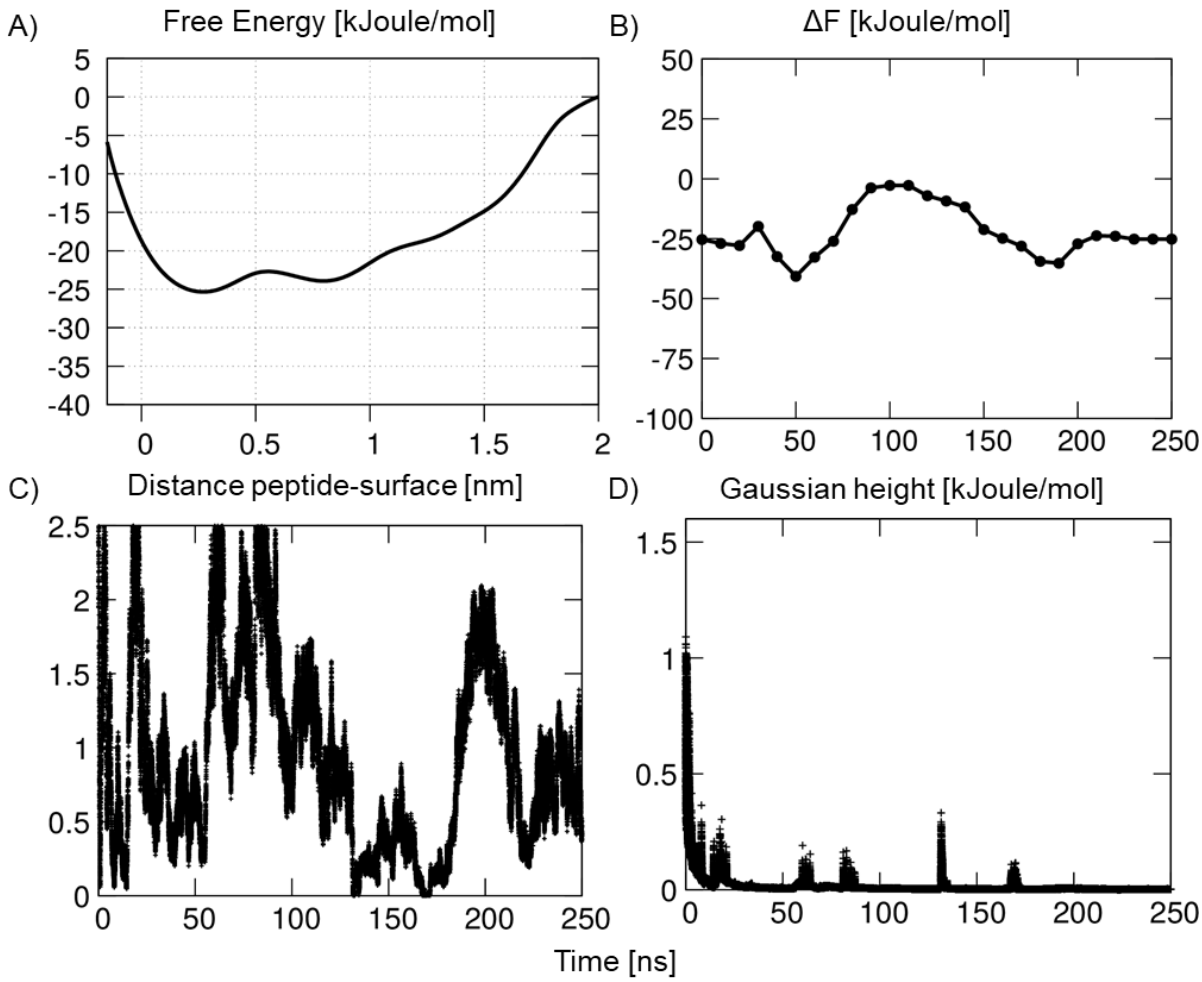

Figure SI 31 Metadynamics results of the PEP peptide interacting with the 18SiO(H,Na) surface. A) Free energy profile; B) Convergence analysis; C) Distance CV through time; D) Gaussian Height.

In Figure SI 32 are reported the metadynamics analysis of the (ARG)9 peptide interacting with the 18SiO(H,Na) surface. The convergence (Figure SI 32 B) is calculated as the difference between the local maximum along the distance CV between 1.5 and 2 nm and the local minimum along the distance CV between 0 and 0.5 nm. The Gaussian height (Figure SI 32 D) through the simulation time is also shown and its exponential trend is in line with the well-tempered recipe. Also the distance CV (Figure SI 32 C) through simulation time is reported for clarity, as it is possible to see how the peptide reach the surface several time, exploring multiple metastable state, as expected in such metadynamics simulation.

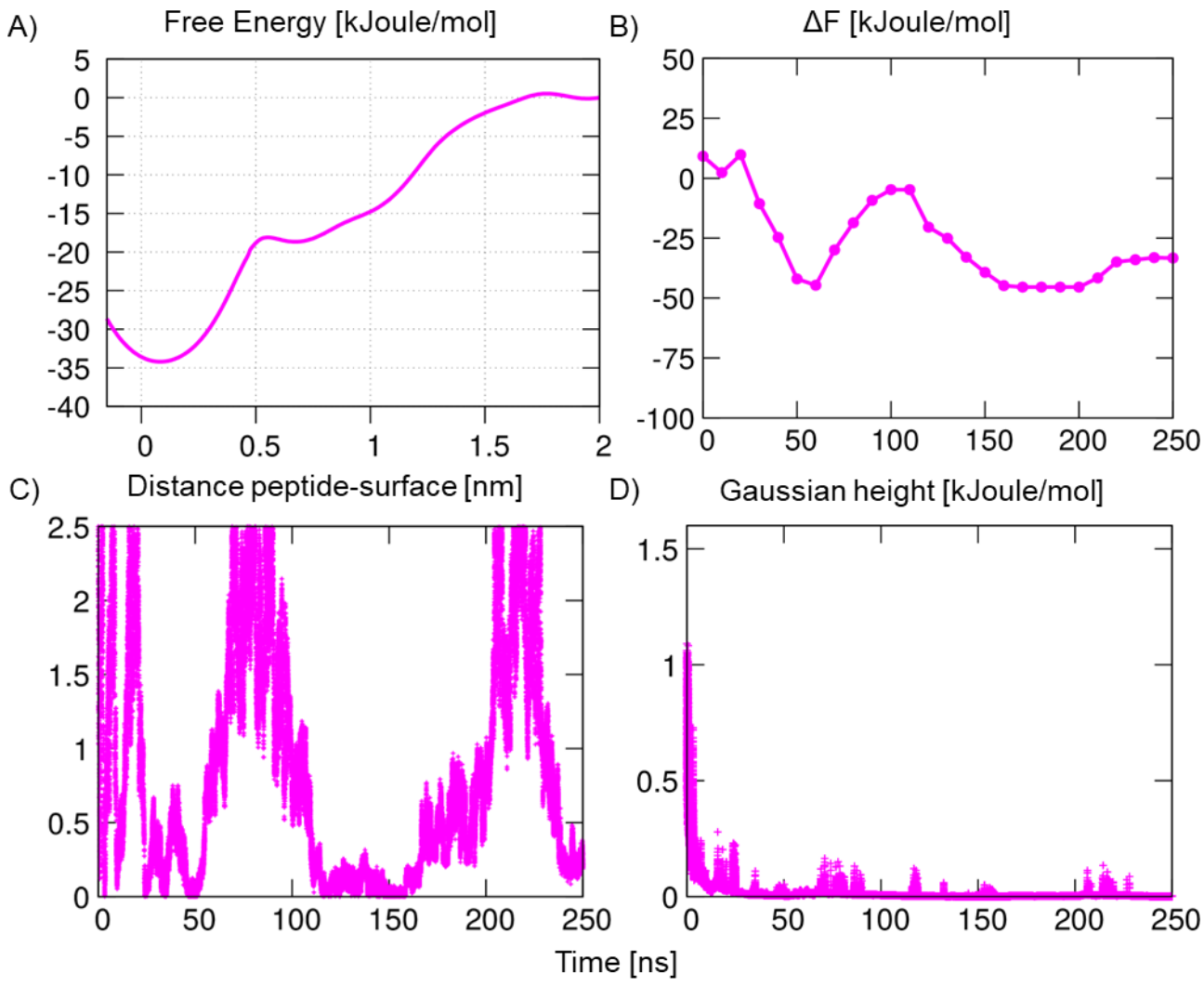

Figure SI 32 Metadynamics results of the (ARG)9 peptide interacting with the 18SiO(H,Na) surface. A) Free energy profile; B) Convergence analysis; C) Distance CV through time; D) Gaussian Height.

In Figure SI 33 are reported the metadynamics analysis of the TAT peptide interacting with the 18SiO(H,Na) surface. The convergence (Figure SI 33 B) is calculated as the difference between the local maximum along the distance CV between 1.5 and 2 nm and the local minimum along the distance CV between 0 and 0.5 nm. The Gaussian height (Figure SI 33 D) through the simulation time is also shown and its exponential trend is in line with the well-tempered recipe. Also the distance CV (Figure SI 33 C) through simulation time is reported for clarity, as it is possible to see how the peptide reach the surface several time, exploring multiple metastable state, as expected in such metadynamics simulation.

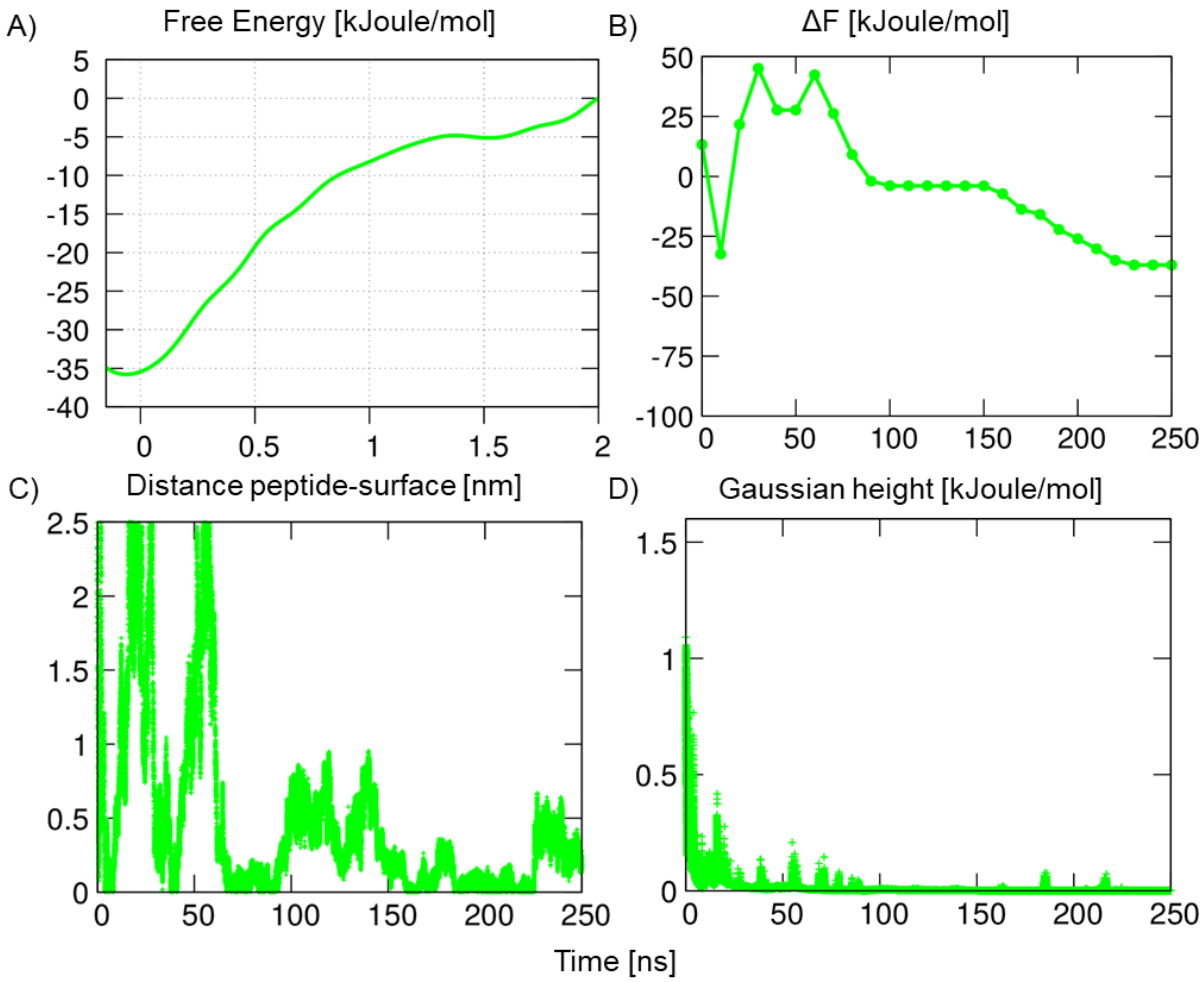

Figure SI 33 Metadynamics results of the TAT peptide interacting with the 18SiO(H,Na) surface. A) Free energy profile; B) Convergence analysis; C) Distance CV through time; D) Gaussian Height.